AN ABSTRACT OF THE DISSERTATION OF

Xiaochen Hu for the degree of Doctor of Philosophy in Mechanical Engineering presented on January 21, 2022.

Title: Optical Sensing for Nondestructive Structural Evaluation and Additive Manufacturing Process Monitoring

Abstract approved: ____

Zhaoyan Fan

Sensing is a significant engineering science which quantify parameters from the physical world and discover the physics running behind the measurement process. Optical sensing makes use of electromagnetic waves from infrared to ultraviolet on the light spectrum as a medium to measure variables, such as position, temperature and strain. Image sensing and fiber sensing are two of the most widely applied optical sensing methods in industries and daily life. They have been studied by the academia for decades, due to their immunity to electromagnetic interference and ease of installation. This dissertation introduced the research on the intelligent and flexible

metrology methodologies for real-time structure and process monitoring based on optical sensing. The works focused on two major topics: 1) structural health monitoring for compact heat exchanger (CHE), and 2) bimetallic additive manufacturing process monitoring.

For the structural health test, a novel online sensing method capable of detecting internal cracks for Compact Heat Exchanger (CHE) was designed and developed through optical fiber sensor based strain measurement. A crack diagnosis model was built to evaluate crack positions based on limited sampling data in mechanical structure. The model established a physical basis to correlate crack position and distributed strain variation that can be detected by the optical fiber sensors. A physical model quantifying the strain transfer from the sensor embedded mechanical structure to the fiber sensor was built to describe the performance of the sensors at different working conditions. A good match has been observed in the comparison of the data from experimental tests and analytical models, with an average relative error 2.4%. Finally, an experimental platform was designed and setup to validate introduced nondestructive test method. The experimental results showed that strain variations can be detected by optical fiber sensors when crack presented in CHE during elastic deformation, plastic deformation and crack growth process.

For bimetallic additive manufacturing process monitoring, an in-situ sensing method for measuring material composition in the printed alloy was modeled and developed based on infrared imaging. The method takes the size of temperature contours surrounding the heated spots during additive manufacturing process as an indicator of the material composition variation. The relationship between material composition and dimensions of the temperature contour was analytically modeled based on Fourier’s law of thermal conduction. The thermal images acquisition by IR camera were processed through a series of designed algorithms to extract geometrical features such as the length and width of the contours, which showed consistent trend through the theoretical analysis. The extracted features and actual weight percentage of copper in the alloy were further used to train an Artificial Neuron Network (ANN) model. The results showed that the accuracy of 94% was achieved when using the trained ANN model to estimate the composition of alloy from the thermal image data.

The analytical/numerical models, simulations, experiments, and data analysis included in this thesis were expected to provide solid support for testing the research hypotheses and developing new hardware/software in advanced manufacturing systems.

Optical Sensing for Nondestructive Structural Evaluation and Additive Manufacturing Process Monitoring

by

Xiaochen Hu

A DISSERTATION

submitted to

Oregon State University

in partial fulfillment of

the requirements for the

degree of

Doctor of Philosophy

Presented January 21, 2022

Commencement June 2022

Doctor of Philosophy dissertation of Xiaochen Hu presented on January 21, 2022

APPROVED:

Major Professor, representing Mechanical Engineering

Head of the School of Mechanical, Industrial, and Manufacturing Engineering

Dean of the Graduate School

I understand that my dissertation will become part of the permanent collection of Oregon State University libraries. My signature below authorizes release of my dissertation to any reader upon request.

Xiaochen Hu, Author

ACKNOWLEDGEMENTS

I would like to express my sincere gratitude to my advisor, Dr. Zhaoyan Fan, for his invaluable advice, continuous support, and patience during my PhD study. His constant encouragement and inspiration kept me going relentlessly in my research. I appreciate his efforts on all discussions we had which gave me directions and path forward around obstacles.

I would like to thank my dissertation committee, Dr. Brian Paul, Dr. Somayeh Pasebani, Dr. Donghua Xu and Dr. Nick Cabot for their invaluable time, suggestions and support along the various stages of my studies.

I wish to thank my colleagues, friends, and the department faculty and staff. Their kind help made my study and life at OSU a wonderful time.

Finally, I am extremely thankful to my parents for their encouragement and support.

CONTRIBUTION OF AUTHORS

Dr. Brian Paul provided technical suggestions and comments for Chapter 2.

Dongqing Yan assisted experimental operation for Chapter 5.

TABLE OF CONTENTS

Page

TABLE OF CONTENTS(Continued)

Page

Page

LIST OF FIGURES

LIST OF FIGURES (Continued)

LIST OF FIGURES (Continued)

LIST OF TABLES

Chapter 1. Introduction

With the development of modern electronics, optics, and control technologies, sensing has been playing a gradually important role in manufacturing systems to quantify the parameters from the machinery, produced parts, and human operators. Amongst various sensing techniques, optical sensing is one of the major categories that make use of light signals in infrared, visible, or ultraviolet as a medium to measure or detect physical variables such as structure, temperature, and strain from the target of interest. Compared to the conventional electrical based sensing, optical sensing is advanced in its non-contact feature and the associated high flexibility, easy installation, and immunity to electromagnetic interference. Figure 1.1 shows the categories of optical sensors within the scope of this thesis. According to the characteristic of detectors, optical sensing can be categorized as optical fiber based sensing and image based sensing. Conventional infrared/light diodes, charge coupled devices (CCDs), and photo detectors are also considered as optical sensors. As most of these sensors are also used in the image sensors as “pixel” elements, they are not separately discussed in this thesis.

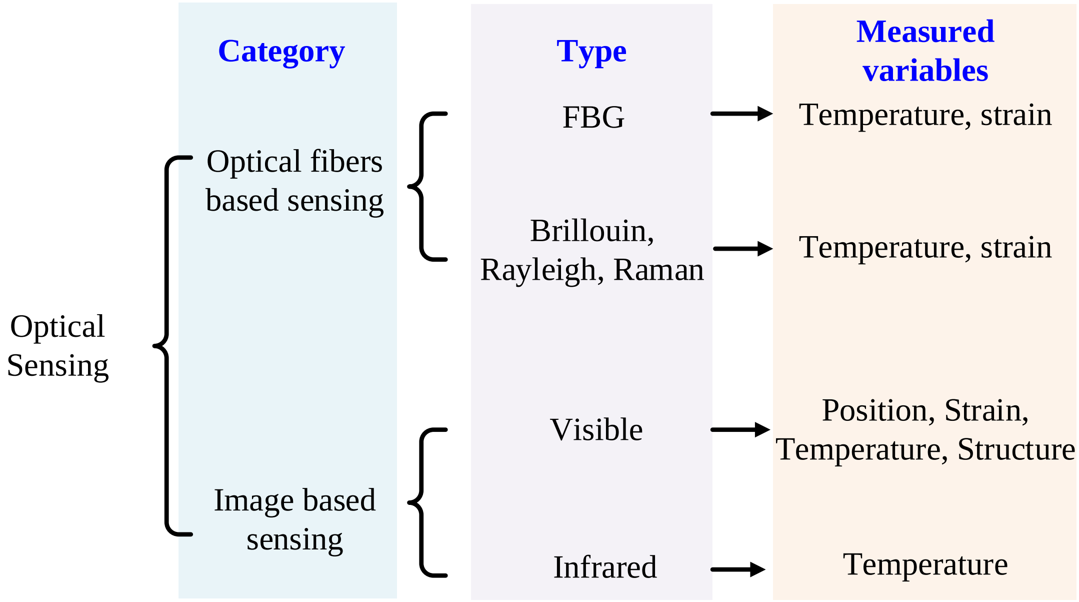

Figure 1.1. Optical sensing technologies

1.1. Optical fiber sensor

Optical fiber was developed as a medium component to transfer light signals with high stability from early 20 century. Since 1960s, optical fiber has been studied to serve as a sensing element to measure temperature and strain [1]. It is one of the most promising sensing methods for structural health monitoring and geohazards prevention due to its ability of acquiring parameters with high speed and sensitivity, small size, immunity to electromagnetic interference and being robust to harsh environment conditions. Optical fiber generally composed of a silicon core and a layer of protective coating made of plastic or metal. When they are being used as physical sensors, a common working principle shared by the optical fiber sensors is to make use of the reflective elements in the fiber core to measure the core deformation induced by temperature or strain variation. Generally, an external interrogator is required for the optical fiber sensors to provide a reference laser source and identify the reflected or back scattered light from the reflective elements. According to the type of reflective elements being used, the optical fiber sensors can measure temperature and strain on 1) single-point or specific locations (with Fiber Brag Grating sensors), or 2) multiple points distributed along the whole fiber, as seen in Figure 1.1.

1) Fiber Brag Grating (FBG)

Fiber Brag Grating (FBG) sensor is the most widely used optical sensor for single-point temperature and strain measurement. FBG sensors have gratings written in the fiber core (as shown in Figure 1.2). The gratings can reflect particular wavelength of incident light from the laser source and transmit all others. The wavelength of reflected light through gratings can be calculated by [2]:

$$\lambda = 2n\Lambda \tag{1.1}$$

where n is the refractive index, Λ is the grating pitch and λ is the wavelength of reflected light. When temperature or strain is applied to the section of fiber core where the gratings are located, the fiber core will be deformed by the thermal expansion or mechanical stress. Accordingly, both the refractive index (n) and grating pitch (Λ) will be changed and lead to a variation in the wavelength (λ) of the reflected light based on Eq. (1.1). When the shift of wavelength $\Delta\lambda$ is read by the interrogator, it is translated into the strain or temperature values according to the mechanical or thermal properties of the fiber core material. As the gratings can be fabricated on multiple locations along the optical fiber, it can be used for quasi-distributed sensing, to measure strain or temperature at specific points where the grates are located. Although some research has reported customized FBG sensor measuring up to 100 points on a single piece of fiber, the general application only includes less than eight channels per piece, due to the limitation on the number of channels and cost to fabricate gratings.

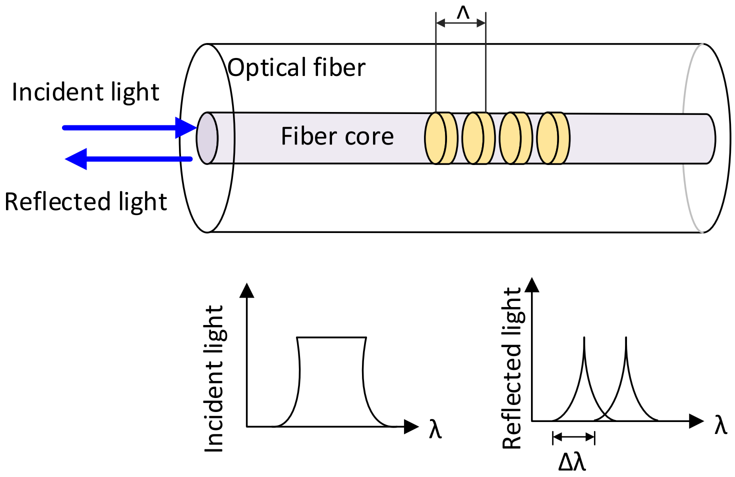

Figure 1.2 FBG sensor

2) Distributed optical fiber sensors

Being different from FBG where the reflective gratings are fabricated in the fiber core, distributed optical fiber sensors make use of the natural microscopic defects in the fiber core to reflect the light from laser source. As the microscopic defect commonly exists in the crystal lattice, they are scattered throughout any of the optical fibers. Consider each microscopic defect could provide a reading of temperature or strain at one location, the distribution of temperature or strain can be read from the whole fiber which high spatial resolution. Due to the inhomogeneous of density, composition and orientation of molecular along fiber core, the light scattered along various directions. Backscattering is the reflection of light wave back to the direction where they came. As these inhomogeneous are evenly distributed through the whole fiber core, theoretically, the temperature or strain can be measured from end to end along the fiber core, if the deformed locations of all the inhomogeneous can be read through the interrogator.

When a beam of light is shot into a piece of optical fiber, the light is scattered by the microscopic defects through all three mechanisms: Rayleigh, Brillouin, and Raman effects. Rayleigh effect refers to the backscattering by the defects smaller than the incident light wavelength. The scattering wave caused by Rayleigh effect has the same frequency/wavelength as the incident light. Brillouin effect considered the acoustic phonons generated during scattering, which added a Doppler shift in the backscattering frequency. As a result, Rayleigh backscattering is sensitive to the dynamic variations in the fiber, such as vibration, while Brillouin backscattering is sensitive to the stationary or "slow changing" variables such as temperature and strain. Raman effected backscattering presented the interaction between incident light and molecular thermal vibration. Thus, Raman backscattering is sensitive to the temperature variations. Figure 1.3 shows the fiber core of distributed optical fiber sensor and its signals when temperature or strain changes. Backscattering presents in each element along fiber length. When temperature or strain is applied on fiber core, the structure of the backscattering element changed which leads to wavelength shift of backscattered light. The interrogator can read the wavelength shift and transfer it as strain/temperature as shown in Eq. (1-2).

$$\frac{\Delta\lambda}{\lambda} = K_T T + K_\varepsilon \varepsilon \tag{1.2}$$

where λ is the wavelength of light, $\Delta\lambda$ is the wavelength shift induced by strain or temperature, K_T and K_ε are the temperature and strain calibration constant.

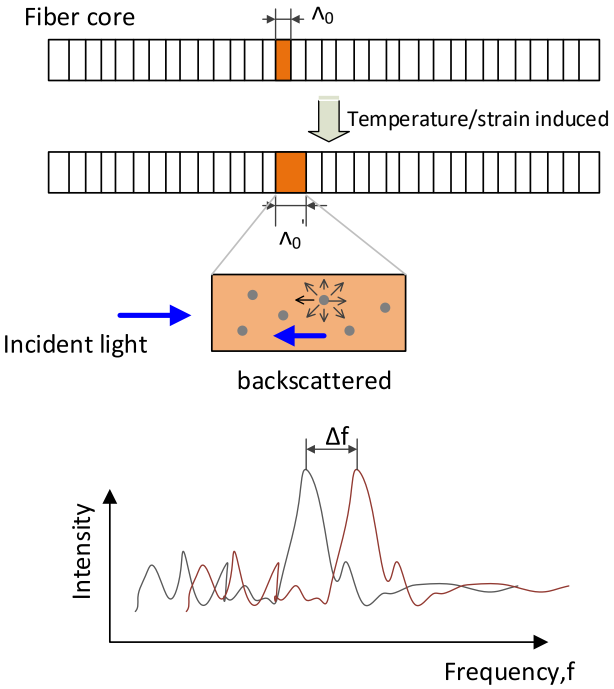

Figure 1.3 Distributed optical fiber sensing

Detection of the optical backscattering signals can be done in time or frequency domains, using optical time domain reflectometry (OTDR) and optical frequency reflectometry (OFDR) methods, respectively. OTDR is capable of long-distance distributed sensing with a sensitivity of 5 με [3]. However, spatial resolution of OTDR is limited to roughly 1 m. The optical backscattering sensor based on OTDR is suitable to applied to test for large scale structures such as buildings or bridges. Conversely, OFDR is capable of refine spatial resolution distributed sensing. The spatial resolution of OFDR sensing can reach to millimeter level. However, the sensing range is limited to roughly 70 m [3]. Table 1.1 shows the sensing performance comparison of different types of optical fiber sensors. According to the specific applications, the suitable type of sensors can be selected based on their sensing performance.

Table 1.1 Sensing performance of optical fiber sensors

Sensors	Transducer type	Sensing range	Spatial resolution	Main measurements
FBG	Single-point	100 channels	2 mm [4]	Temperature, strain, displacement
Brillouin OTDR	Distributed	20-50 km [3]	1 m [3]	Temperature, strain
Rayleigh OFDR	Distributed	50-70 m[5]	<1 mm[6]	Temperature, strain
Roman	Distributed	1-37km [7], [8]	1-17cm [7], [8]	Temperature

1.2. Image-based sensing

Image-based sensing captures images from the objects and accordingly measure the objects' size, temperature, deformation from the features extracted from the images. According to the wavelength being detected, image-based sensing includes visible light imaging and infrared imaging. The imaging systems can also detect X-ray or ultraviolet (UV) waves by combining with fluorescent components, which convert the invisible high energy waves into visible light. Due to the fast response of the sensing elements used in imaging devices and noncontact sensing method, imaging sensor and systems has been widely used in dynamic system monitoring and remote monitoring.

Infrared camera is one type of imaging sensors which capture thermal images of heat sources in IR region (760 nm – 10^6 nm) in the light spectrum, as shown in Figure

1.4. Each of the pixels in a thermal image can be used to measure temperature based on the thermal radiation from the heat source. Based on Plank's law, the radiated power I per unit surface for a particular wavelength (Wm^{-2} µm^{-1}sr^{-1}), from an ideal blackbody can be expressed as:

$$I = \frac{c_1}{\lambda^5[\exp(\frac{c_2}{\lambda T}) - 1]} \tag{1.3}$$

where λ is the wavelength of radiation (µm), *T* is the temperature in absolute scale (K), c_1 (W µm^4/m^2) and c_2 (µmK) are the first and second radiation constants, respectively.

By integrating Eq. (1-3) over all wavelengths, the total power of radiation P in a unit area can be obtained.

$$P = \varepsilon\sigma T^4 \tag{1.4}$$

where ε is the emissivity of the emitting surface, σ (W m^{-2}K^{-4}) is the Stefan-Boltzmann's constant.

When the radiated power is captured by a detector, such as a pyrometer (single point), CCD (linear), or IR image sensor (2D), the temperature of the blackbody heat source can be then retrieved. In practice, the radiation emitted from the heat source are constrained in some specific wavelengths. For example, the characteristic wavelength of radiated IR from aluminum is 3.1 um, and 1.6 µm for melted iron [9]. For each IR imaging sensor, the measurable wavelength is also limited to a certain range determined by the type of sensing element. Selection of IR imaging sensors in applications requires to match the coverage wavelength with the radiation from the specific heat sources being measured.

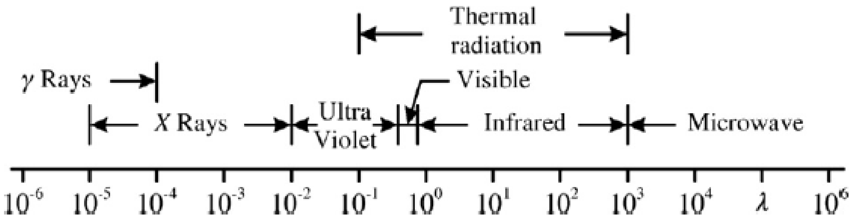

Figure 1.4. Electromagnetic spectrum at micrometer scale [10]

In addition to sensing wavelength range, spatial resolution and frame rate are also the key characteristics of imaging sensors. Spatial resolution is determined by the number of pixels within a constrained image frame. Increased spatial resolution will provide detailed readings on the temperature variation and gradient across a certain space, but at the same, the amount of generated data in each image will be increased. Frame rate is important especially for capturing fast dynamics such as temperature variation during additive manufacturing. Both high spatial resolution and frame rate will result in high computation load in processing the image data and the cost of sensing devices. Practically, a trade-off is needed in selecting these parameters to balance the performance and expenses.

1.3. Organization

This dissertation introduces the research on optical sensing for structural and process monitoring in real-time. The work focuses on two major topics: 1) structural health test for compact heat exchanger, and 2) alloy additive manufacturing process monitoring.

In chapter 2, the crack detection method for PCHE by combining strain field analysis and measuring strains was introduced. A crack diagnosis model was built to predict crack positions based on limited sampling data in structure. A numerical model was built to analyze strain distribution when crack presents in PCHE. The crack position detection algorithm was developed based on Tikhonov regularization. The detection accuracy of the proposed method was verified by simulations considering variety of sensor installation scheme, crack positions and crack dimensions. The relationship between crack position and strain variation field was correlated to provide a theoretical basis for developing new structural health test method.

In chapter 3, strain transfer characteristic of optical fiber strain sensors was studied to compensate measurements and improve measurement accuracy. An analytical model was built based on mechanical equilibrium. Compared to the previous work, both mechanical and thermal effects on strain transfer were considered. The built model can be applied to improve measurement accuracy for system in high temperature and high pressure environment. The analytical model was verified by experiments under different mechanical and thermal loads.

In chapter 4, experimental platform was designed and setup to test sensor responses when elastic, plastic deformation and crack growth presents in the structure. The feasibility of embedding distributed optical fiber strain sensors to detect cracks for PCHE was investigated. The experimental results were compared with finite element analysis (FEA) results. As a component affecting the crack detection accuracy, the fiber coating was discussed to quantify its correlation with the strain measurement results.

In Chapter 5, an in-situ sensing method for material composition identification was proposed based on temperature field analysis and intelligent algorithms. Comparing with previous research that focused on single material printing, the proposed method correlated the relationship between temperature field and material composition. According to thermal conduction, the relationship between material composition and temperature field was theoretically investigated. An infrared (IR) camera was installed to capture temperature field with different material compositions during additive manufacturing process. The features of temperature field were extracted through image processing and collected as inputs to machine learning. An Artificial Neural Network (ANN) model was built to correlate the relationship between material compositions and features of temperature field based on experimental data

STRAIN SENSING FOR COMPACT HEAT EXCHANGER DEFECT DETECTION

Xiaochen Hu, Zhaoyan Fan and Brian Paul

Part of Contents Published in *Pressure Vessels and Piping Conference*

Volume 58967, 2019, Page V005T10A006

Chapter 2. Strain sensing for compact heat exchanger defect detection

Abstract—The development of Compact Heat Exchangers (CHE) improves heat transfer efficiency with surface-to-volume ratios approaching 2500 m^2/m^3. In the applications such nuclear plants, CHE need to work for years in a harsh environment of high temperature up to 800 °C and high pressure up to 20 MPa. Any structural failure, i.e. cracks due to material fatigue or residual stress concentration in the CHEs, may result in safety problems and tremendous economy losses. Compared to the conventional heat exchangers, the non-destructive testing for CHE is challenging because the deformation of micrometer sized channels is hard to detect by the conventional means such as strain gauges or ultrasonic sensors. This paper presents a novel approach to detect the presence of cracks using fiber strain sensors embedded in the compact heat exchangers. The fiber sensors are proposed to install the heat exchanger with the microchannel plate stacks in the heat exchanger, measuring the strain distribution in the structure during the operation. Numerical and analytical models of CHE with and without cracks are built to learn crack size influence on strain variation. Sensors' sensitivity to crack positions was calculated through simulation. A defect retrieval algorithm based on Tikhonov regularization is presented to achieve crack detection according to sensors' outputs. A sample CHE section with 5x5 channels are simulated to quantitatively test the accuracy and validity of the proposed method.

Keywords: crack detection, Finite Element Analysis (FEA), compact heat exchanger, strain sensor

2.1. Introduction

Compact Heat Exchanger (CHE) can be applied in variations applications that require exceptional compactness for effective heat exchanging. The process to assemble CHE in manufacturing is generally stacking multiple plates with one side etched semi-circular grooves with diameter of 1 millimeter, followed by diffusion bonding. As shown in Fig. 1, the plates are arranged in the same direction so that the flat surface on one plate is bonded to the etched surface on the other one to form microchannels. In the nuclear application, compact heat exchangers are considered as a potential candidate for intermediated heat transfer of advanced nuclear reactors with gaseous working fluid, such as high temperature gas cooled reactors. Supercritical carbon dioxide is commonly used in the CHE as the cold channel fluid [11], allowing operating the CHE at a temperature up to 600 °C and pressure up to 20 MPa in the microchannels. Such a high-temperature and high-pressure environment within millimeter scale structures, make the structural cracks, generated either in the manufacturing process or by fatigue during the operation, easy to propagate through the CHE structure. Sometimes the cracks could penetrate through the isolation walls between the cold and hot flows, and finally result in critical safety problems, especially for the CHEs used in the nuclear plants.

The conventional way to estimate the health status of HEs is to set a fixed life time based on the historical data. However, as the initial condition and operation states of CHEs are not fully consistent with each other, the empirical life time estimation could either miss the fast-developed cracks or underestimate the life time for individual parts. For the nondestructive test of tubes, multiple technologies have been developed to monitor the health status of the structure. Lee et al. applied ultrasonic wave to visualize damage of nuclear power plant pipeline [12]. Safizadeh et al. presented a gas pipeline corrosion mapping method by using pulsed eddy current [13]. Besides the pipeline detection on the surface or subsurface, Abdullah et al. studied neutron tomography technique to image internal defect of pipeline [14]. Carvalho et al. studied magnetic flux leakage technique to detect defects of pipe and applied artificial neural networks to distinguish types of defect (external corrosion, internal corrosion and lack of penetration) [15]. Most of methods to detect defects of pipeline are on the surface or subsurface, like ultrasonic wave detection, eddy current testing and magnetic flux testing. Neutron tomography is a method can achieve internal structure detection, but protective measures must be taken against harmful neutron radiation leaks. These methods are available for the single pipelines with normal size which defects exist around tube wall. But it is hard to apply on the compact heat exchanger which defect may exist inside the structure and the size of tubes are at millimeter scale. Meanwhile, if the monitoring process need to be conducted in every channel every time, it would cost much time and not economic. Strain field analysis combined with measurement techniques is an available method to achieve internal defect detection with compact structure. Turnbull et al. [16] studied strain and stress distribution around a single corrosion pit in a cylindrical steel specimen from finite element analysis, the strain distribution and evolution of stress corrosion can be observed. Lee et al. [17] presented thermal stress distribution in the compact heat exchanger and found stress concentration is clear near the channel tip. These strain field analysis methods can provide theoretical reference for indirectly measurement.

This paper presents a novel approach to detect the presence of cracks using fiber strain sensors embedded in the compact heat exchangers. The fiber sensors are installed on an instrumentation plate bonded together with the microchannel plate stacks in the heat exchanger, measuring the strain distribution in the structure during the operation. Where there is crack presence or crack propagation between the channels, the variation of strain distribution on the instrumentation plate is detected by the fiber sensors to retrieve the size and location of the crack. This paper focuses on the simulation test of the approach, to quantitatively evaluate the performance of the approach and provide guideline for the experimental validation. Mathematically, the crack retrieval is realized by solving an ill-posed backward problem through two steps: 1) build a forward equation from crack position to sensor measurements by numerically simulating the sensor response to cracks at each possible locations; 2) inverse the mathematical relationship to establish an algorithm estimating crack location from sensor output. A two-dimensional thermal and structure coupling model is built by ANSYS to simulate the strain distribution of heat exchanger with/ without cracks. As the number of strain values sampled by the fiber strain sensors is far less than the possible crack location within a given space, iterative Tikhonov Regularization method is adopted to solve the ill-posed problem. The approach was tested with simulation results from the numerical model. The estimated crack locations are compared with the “true” crack location set in the simulation to quantify the estimation error. The detailed methodology and simulation results are presented in the next sections.

2.2. Modeling

The CHE is generally designed in a multi-layer structure. Each layer contributes one row of channels. Figure 2.1 shows a sample section of the CHE with semi-circular channels (1mm radius) with seven layers, in the cross-section view. When the CHE is in operation, cold (blue) and hot (red) fluid flows pass through the channels with high pressure to exchange the heat. The proposed method installs the fiber strain sensors (the number of sensors could varies based on required accuracy) between the channels in the sample section.

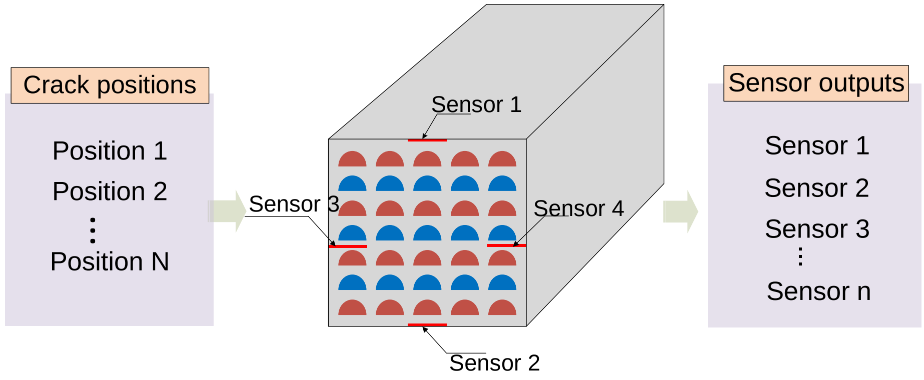

(a) The principle of detection cracks in CHE

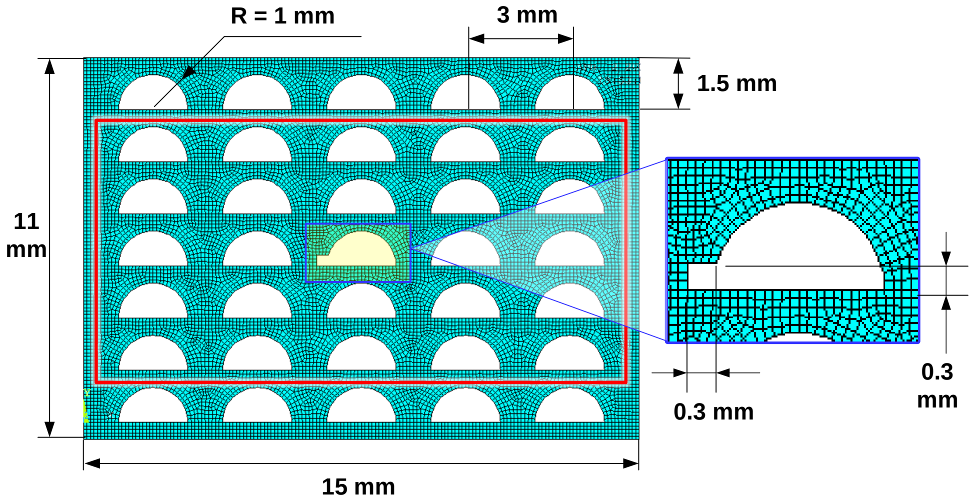

(b) Dimension of CHE with crack

Figure 2.1 Illustration of crack position sensing method

Depending on the presence of crack, there are two major states being investigated.

1) When there is no crack, the pressurized channels deform the CHE structure and builds a certain strain distribution. The sensors measured the strains at each specific location.
2) When a crack is present in one of the channels, the structural deformation leads to variation in strain distribution. Consequently, the individual fiber strain sensor's output is changed after the presence of the crack.

The variation in strain sensor output can be extracted by comparing the outputs of state (1) and (2). Amplitude of the sensor's output variation is determined by the distance to crack as well as the surrounded CHE structure. In this paper, the process of a crack-induced deformation being detected by the sensors is assumed as a forward problem. Based on this assumption, the possible crack position, can be estimated by combining the sensors outputs and their locations in the CHE through solving an ill-posed backward problem. To simplify the simulation model, the interference between the fiber sensors and local strain distribution was ignored, based on the fact that the sensor diameter (0.1 mm) is much smaller than the channel radius (1 mm level)

The Finite Element (FE) model is established on ANSYS platform to simulate the forward sensing process and quantify the effect of crack locations on the individual sensor's output. The sample section of CHE is built in the FE model, as shown in Figure 2.1 (b). The modeled structure composed of 7 layers in total, each containing 5 semicircular channels. The channels are arranged in 7 x 5 matrix in the cross-section view as shown in Figure 2.1 (b). The thickness of each layer is 1.5 mm. The radius of the semicircular channel is 1 mm. The distance between two channels on the horizontal direction is 3 mm. The temperatures for the cold and hot fluid flowing through the channels are set as 420 ˚C and 600 ˚C, respectively. The associated pressures for the cold and hot flows are set as 20 MPa and 8 MPa, respectively. The same type of flow is applied to the same layer as shown in Figure 2.1 (a). The modeling and simulation of the forward problem is based on the assumption that all the strain sensors measure the strain in horizontal direction. So the simulation results and analysis only consider the horizontal strain/stress distribution in the structure. The crack is set as a 0.3 x 0.3

mm rectangle vacant at the corner of a selected channel. Figure 2.1 (b) shows the case where the crack presents in the channel at (4, 3) (the 4th row and 3rd column). The material of the structure was chosen as Incoloy 800H which is considered as a candidate material for the next generation of CHE. The detailed material properties are shown in Table 2.1.

Table 2.1 Material properties of alloy 800h

Young's Modulus	Poisson Ratio	Density	Special Heat	CTE	Thermal Conductivity
157.7 GPa	0.373	7.94×10^3 kg/m^3	460 J/kg·°C	17.1×10^{-6} /°C	21.1 W/m°C

In order to build the relationship between the crack position and the sensors' output, the 5 x 5 channels in the center of the modeled section (as cropped by the red frame in Figure 2.1(b)) are selected as the candidate locations for the crack presents. Mathematically, the crack location can be expressed by an array P (p_1, p_2, ...p_n), where element p_i represents the i^{th} channel (i = 1, 2,…n, n=25). The value of p_i is set to either zero or one depending on the presence of crack in the channel:

$$p_i = \begin{cases} 0, & \text{when there is no crack} \\ 1, & \text{when a crack is present} \end{cases}$$

For the case as shown in Figure 2.1 (b), where the crack presents in channel #13, the value of P array is (0, 0, …, $1_{i=13}$, 0, …0). Similar to the representation of the crack locations, the crack-induced variation in sensors output can be expressed by an array S (s_1, s_2, … s_m), where m is the total number of sensors. If the relationship between the crack presence and the sensors response can be approximated as linear relationship, the sensors output P is expressed as the multiplication of a sensitivity matrix *G* and the location array *P*, which can be expressed as:

$$S = G \cdot P \tag{2.1}$$

where G is an *m x n* matrix, expressed as:

$$G = \begin{pmatrix} g_{11} & g_{12} & \cdots & g_{1n} \\ g_{21} & g_{22} & \cdots & g_{2n} \\ \vdots & \vdots & \vdots & \vdots \\ g_{m1} & g_{m2} & \cdots & g_{mn} \end{pmatrix} \tag{2.2}$$

By substituting the expression of P, S into Eq. (2.1), the element $g_{i,j}$ (i = 1,2, …, n; j = 1, 2, … m) in the sensitivity matrix can be calculated by simulating the j^{th} sensor output when the crack is set to be present in the i^{th} channel ($p_i = 1$), expresses as:

$$g_{ij} = s_j, \quad when \;\; p_{\mathrm{i}} = 1 \text{ and } p_k = 0 \; when \; k \neq i \tag{2.3}$$

Thus by setting the crack to each of the channels and simulating the associated sensors output, the whole sensitivity matrix G can be calculated.

2.3. Simulation

To include temperature induced thermal stress into the model, a thermal analysis is firstly applied to simulate the temperature distribution caused by the hot/cold flows. Then the temperature distribution is imported to structural analysis as an input to simulate the total strain distribution. In this work, the location of crack is assumed to be present at the corner of the semi-circular channels, where the stress/strain concentrates. Strain variation along horizontal direction is obtained by comparing strain distribution of heat exchanger with crack and without crack. Figure 2 shows the case where a crack is set to channel #13. The simulation results from each of the steps are shown in Figure 2.2 (a)-(e).

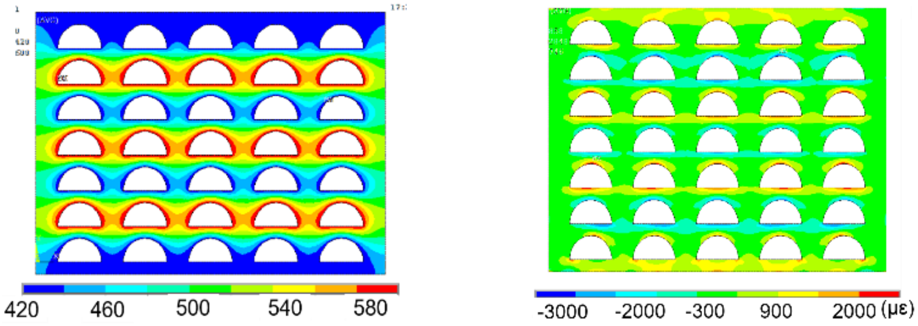

(a) Temperature distribution without crack

(b) Strain distribution without crack

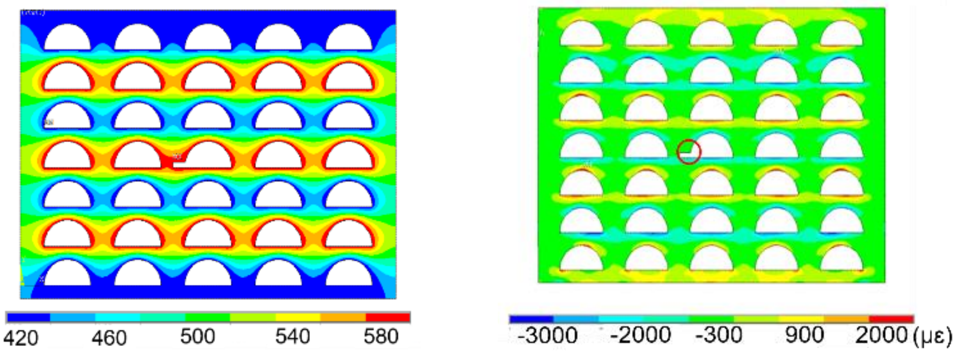

(c) Temperature distribution with crack

(d) Strain distribution with crack

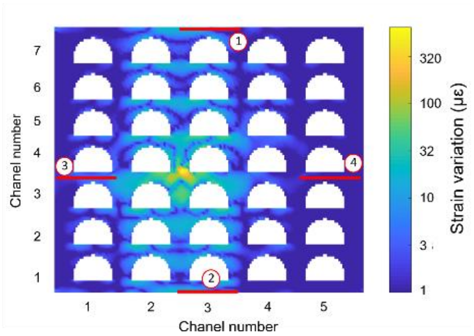

(e) Strain variation distribution

Figure 2.2 Simulation results

Figure 2.2 (e) shows the distribution of strain variation induced by the crack presence. Mathematically, it is calculated by subtracting the strain distribution in Figure 2.2 (b) (without crack) from the distribution in Figure 2.2 (d). The maximum strain variation (100 με), as shown by the bright spot in Figure 2.2 (e), is present at the crack location. If four fiber strain sensors are embedded in the structure close to the middle point of the four edges, as shown in Figure 2.2 (e), the sensors' output can be estimated by the simulated strain values at the same locations. For the arrangement in Figure 2.2 (d), the associated output for sensors #1, #2, #3, and #4 are simulated as 3.5μ, 1.5μ, 15μ, and 3.1μ, respectively. Such a level of strain is measurable with high resolution (<1μ) commercial fiber strain sensors [18]. By repeating this process to simulate all the possible crack locations in the 5x5 candidate channels, the variation in each of the sensors' outputs can be arranged accordingly to the set location of crack, as shown in Figure 2.3. Referring to Eqs.(2.2-2.4), the four series of values shown in Figure 2.3 (a)-(d) are equivalent to the four rows in the sensitivity matrix *G*.

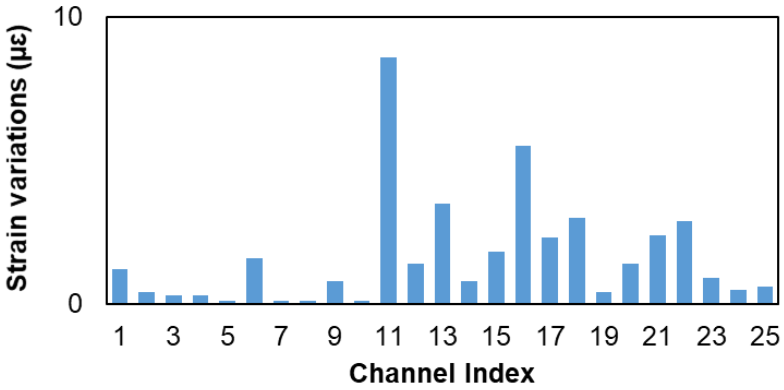

(a) Sensitivity of sensor 1

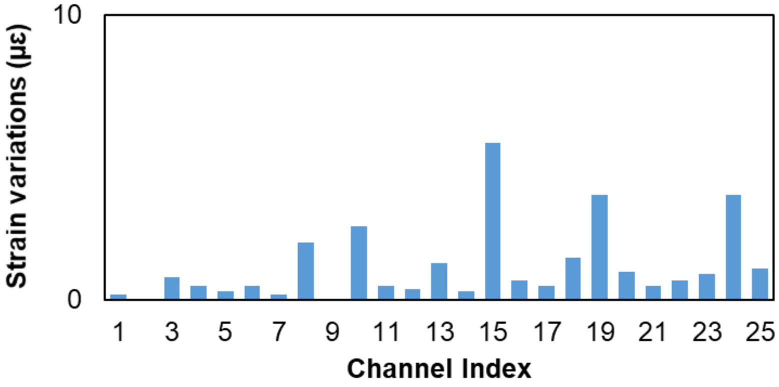

(b) Sensitivity of sensor 2

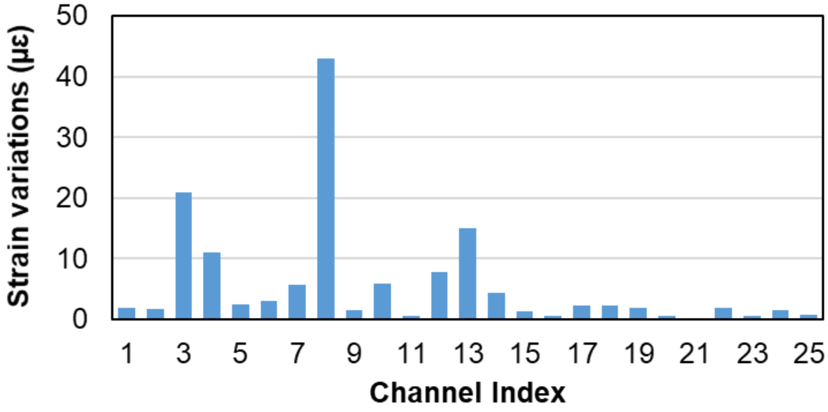

(c) Sensitivity of sensor 3

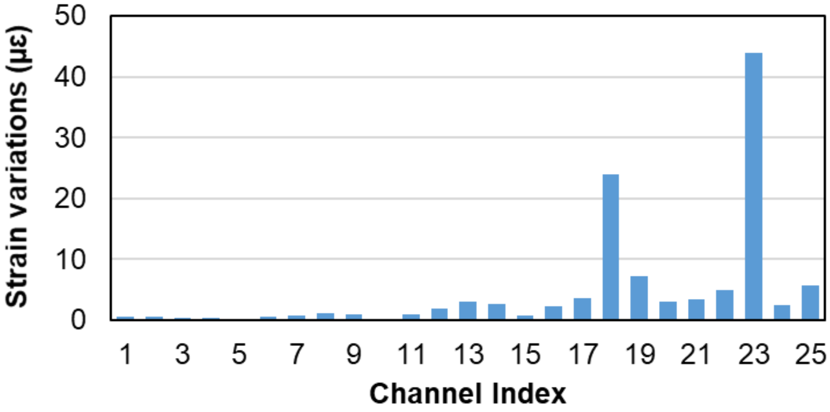

(d) Sensitivity of sensor 4

Figure 2.3 Sensor outputs with different crack positions

2.4. Mathematical Model for Position Detection

2.4.1. Crack Retrieval Algorithm

To estimate the crack location P from the sensors output variation S, the relationship as given in Eq. 2.2 needs to be inversed by considering P as a function of S (inverse problem), based on the simulated sensitivity matrix G. Physically, the number of sensors that can be embedded to the CHE structure is always constrained by the limited space. Also, it is preferred to make used of each sensor to monitor multiple channels to save the expense. Thus, the number of sensors is always less than the number of channels in the realistic application. Such a fact result in that the matrix G is rectangular, e.g. 4 x 25 as shown in Figure 2.1 and Figure 2.3, and the inverse form of G is not available. Mathematically, the inverse problem to solve P from S is ill-posed. Another consideration for solving the backward problem is that some of the elements in matrix G are small numbers approaching zeros, as seen in Figure 2.3, due to the physics that a specific sensor could have weak response to a crack that is apart from the sensor in long distance.

This work adopts iterative Tikhonov Regularization method, which has been widely used to solve the ill-posed inverse problems. The general form of the regularization for solving the crack location can be expressed as:

$$\hat{P} = (G^{\mathrm{T}} G + \lambda\,\mathrm{I})^{-1} G^{T} S \tag{2.4}$$

where λ is the regularization parameter. Generally, the value of λ is a number < 1 to guarantee the determinant of ($G^T G + \lambda I$) is not zero, given the presence of small elements in the G matrix. Some research has studied the mathematical methods to optimize the regularization parameter, including the discrepancy principle method [19], the generalized cross-validation method [20] and L-curve method [21]. If λ is too small, the determinant of (G^TG + λI) will approach zero as the sparse nature of sensitivity matrix G. As a result, the inverse form of (G^TG + λI) will be sensitive to any fluctuation in the data. On the contrary, if λ is too large, the term (G^TG+ λI) will have a large deviation from G^TG, and thus, results in a large approximation error in the calculation. In practice, the regularization parameters are usually chosen empirically [22] according to the requirements in various applications. In this paper, the regularization parameters of 10^{-3}, 10^{-4}, 10^{-5} have been tested. It is found that the value $\lambda=10^{-4}$ achieves highest accuracy among the candidates. Thus, $\lambda=10^{-4}$ is applied for processing the data.

The estimated crack position $\hat{P}$ substitute back into Eq. (2.1) to estimate the sensors output variation:

$$\hat{S} = G \cdot \hat{P} \tag{2.5}$$

The difference between the estimated and the simulated variation is calculated as:

$$\Delta = S - \hat{S} \tag{2.6}$$

The difference is substituted back into Eq. (2.4) to take the place of *S* to update the crack position till Δ goes below a threshold (1/1000 με in realistic calculation). The iterative algorithm is shown in Figure 2.4.

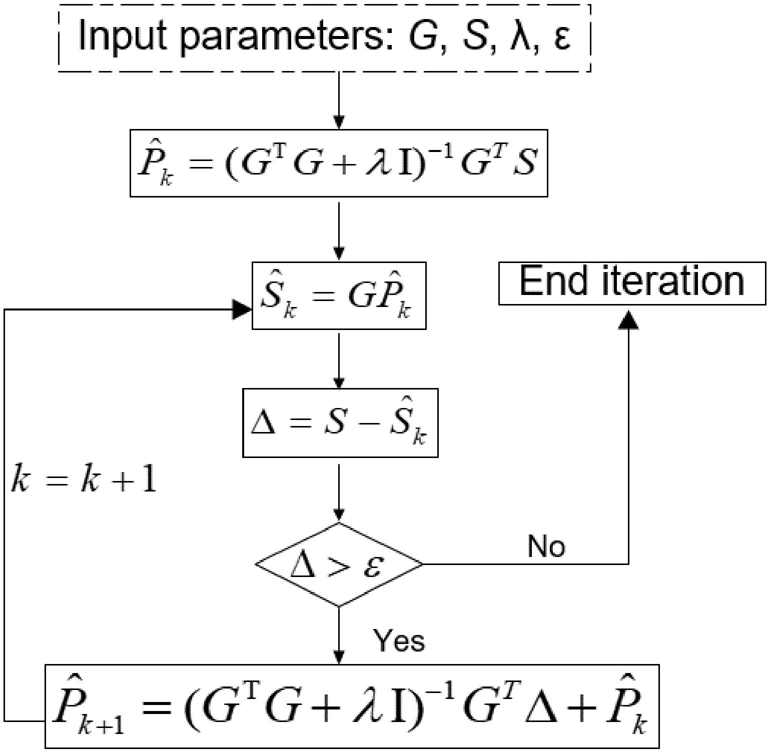

Figure 2.4 Iterative algorithm for crack position retrieval

2.4.2. Retrieval Algorithm Accuracy Analysis

The developed crack retrieval algorithm is tested using the simulated sensors output when the crack is set to different channels in the numerical model. Figure 2.5 (a)-(d) shows the cases when the crack is set to locations (2, 1), (2, 3), (5, 3), and (3, 5), respectively. Each of the grids in the chart shows the location of a channel in the 5 x 5 matrix. The location of the set crack is highlighted by the blue frames. The calculation results (possibility of crack presence) is put in each of the grids and highlighted by the intensity of red color. It is seen that in cases shown in Figure 2.5 (a)(c) and (d), the estimated results exactly match the actual crack locations. While for Figure 2.5 (b), the locations are not perfectly matching but close (1 row and 1 column apart from each other). To quantify the estimation error, the distance from the estimated and actual crack locations are expressed by the number of rows and columns in the matrix, e.g. the error in Figure 2.5 (b) is calculated as $\sqrt{1+1}$ = 1.41.

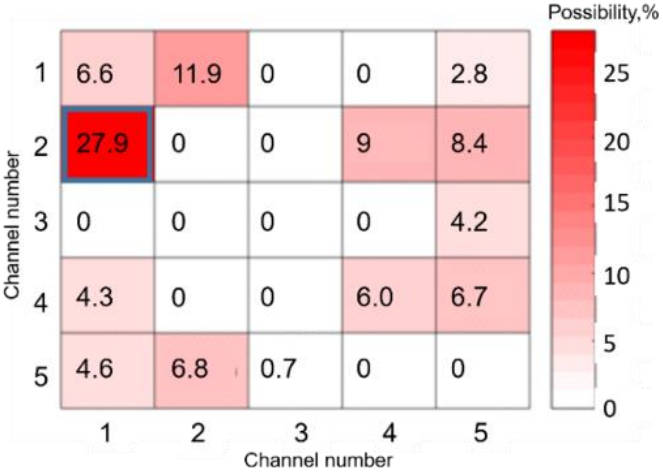

	1	2	3	4	5
1	6.6	11.9	0	0	2.8
2	27.9	0	0	9	8.4
3	0	0	0	0	4.2
4	4.3	0	0	6.0	6.7
5	4.6	6.8	0.7	0	0

(a) Actual crack location (2, 1)

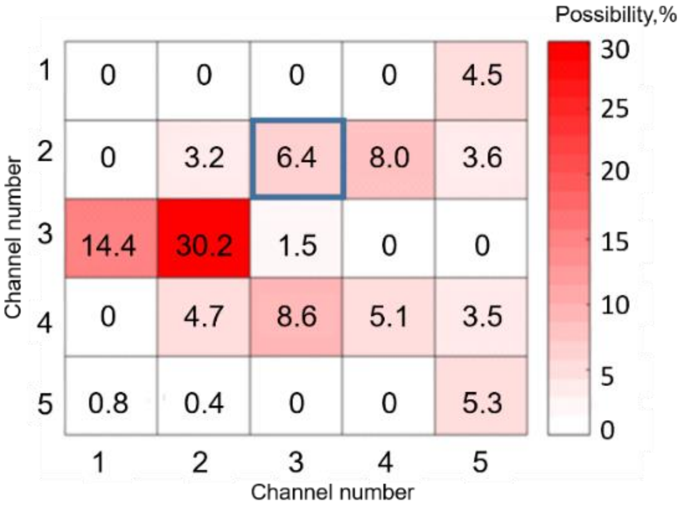

	1	2	3	4	5
1	0	0	0	0	4.5
2	0	3.2	6.4	8.0	3.6
3	14.4	30.2	1.5	0	0
4	0	4.7	8.6	5.1	3.5
5	0.8	0.4	0	0	5.3

(b) Actual crack location (2, 3)

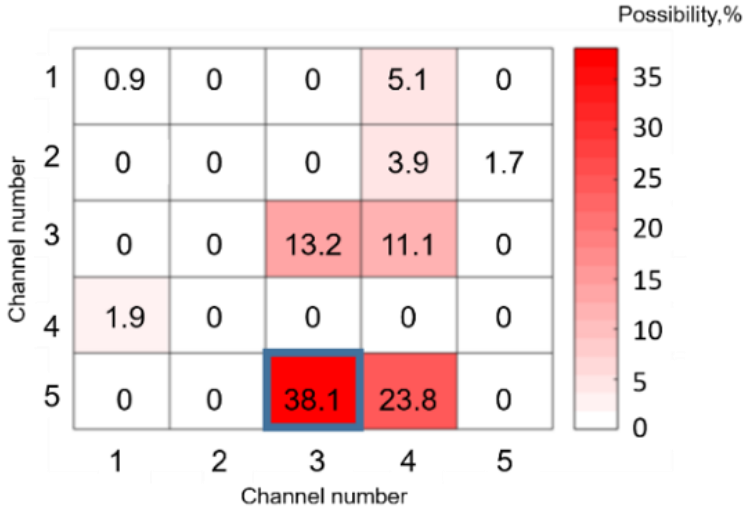

	1	2	3	4	5
1	0.9	0	0	5.1	0
2	0	0	0	3.9	1.7
3	0	0	13.2	11.1	0
4	1.9	0	0	0	0
5	0	0	38.1	23.8	0

(c) Actual crack location (5, 3)

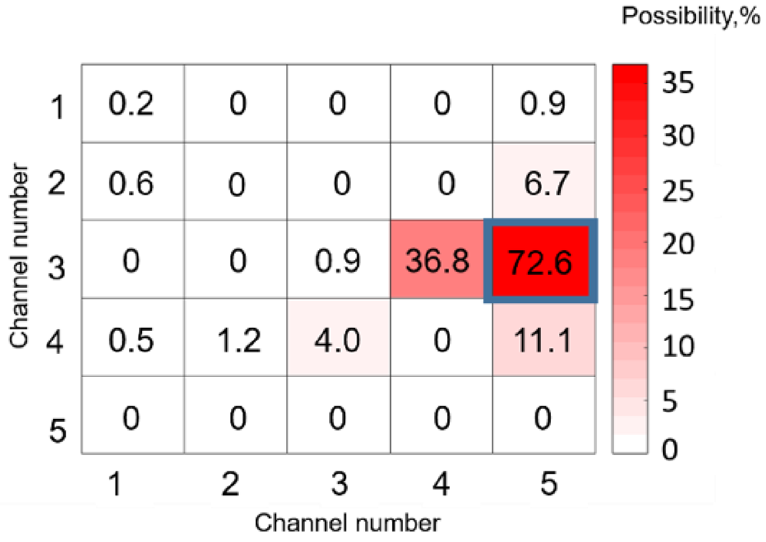

	1	2	3	4	5
1	0.2	0	0	0	0.9
2	0.6	0	0	0	6.7
3	0	0	0.9	36.8	72.6
4	0.5	1.2	4.0	0	11.1
5	0	0	0	0	0

(d) Actual crack location (3, 5)

Figure 2.5 Estimation result by retrieval algorithm

With the four sensors setup, by exhaustively testing the crack locations in each of the 25 candidate channels, the estimation errors are calculated as shown in Figure 2.6. It can be observed that the maximum error (4.47) is associated with the cases where the cracks are present in or close to the corners, due to the long distance from the crack location to two or more sensors reduced their sensitivity to the structural deformation.

Such a problem can be improved by increasing the number of embedded fiber strain sensors in the CHE.

4.47	1	0	1	1.41
0	1	1.41	0	1
1	0	1	1	0
2.23	1	1.41	1.41	1
4.47	4.12	0	1	4.47

(a) Position error in each channel

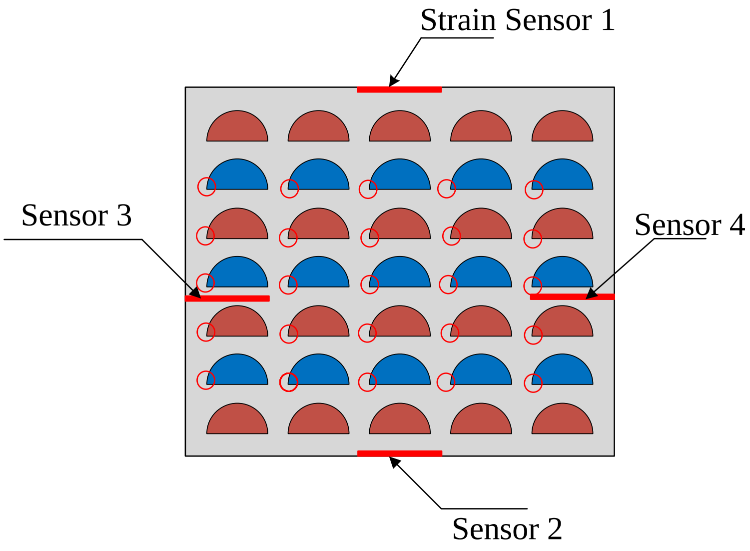

(b) Schematic of sensor installation

Figure 2.6 Position error with 4 sensors

2.5. Discussion on developed method

2.5.1. Number of sensors

Figure 2.7 shows the case studies where five and nine sensors are applied. The increased sensor density relatively reduced the distance from the sensors to the possible crack locations and thus improved the measurement accuracy. By calculating the mean values of all the errors in the grids, the average error for the three cases (4, 5, and 9 sensors) are calculated as 1.4, 1.2, and 0.4. When 9 sensors are installed, the calculation position errors in most channels are 0. Moreover, by comparing prediction errors when different number of sensors installed inside the structure, it is shown the prediction accuracy is low when the distance between a crack position and a sensor location is larger than 2 channels. Therefore, it is speculated that each sensing point can cover 2 x 2 channels approximately to get reasonable prediction results.

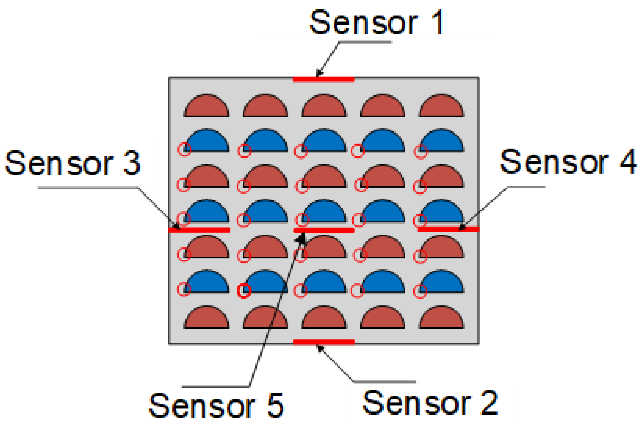

(a) Schematic of five sensors installation

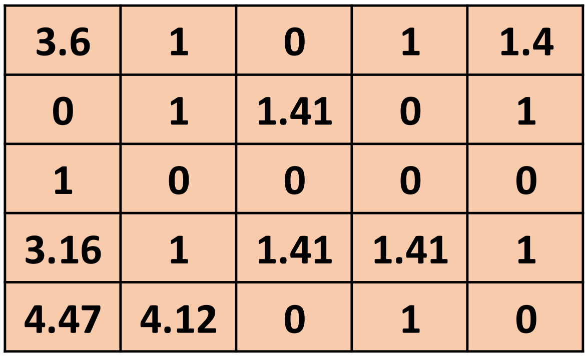

3.6	1	0	1	1.4
0	1	1.41	0	1
1	0	0	0	0
3.16	1	1.41	1.41	1
4.47	4.12	0	1	0

(b) Position error with 5 sensors

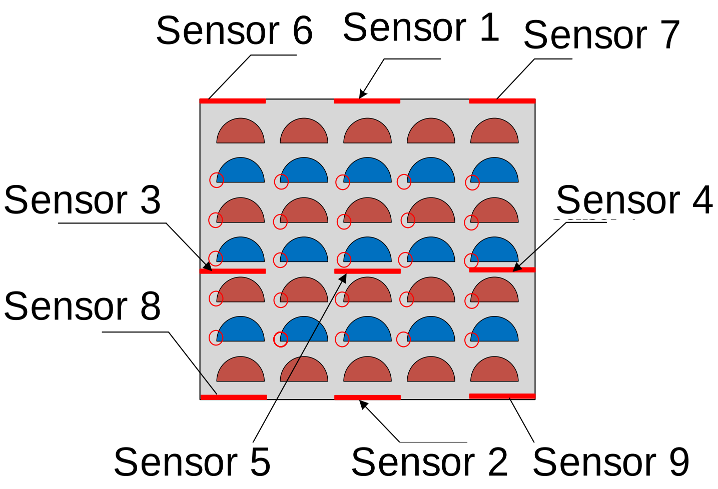

(c) Schematic of nine sensors installation

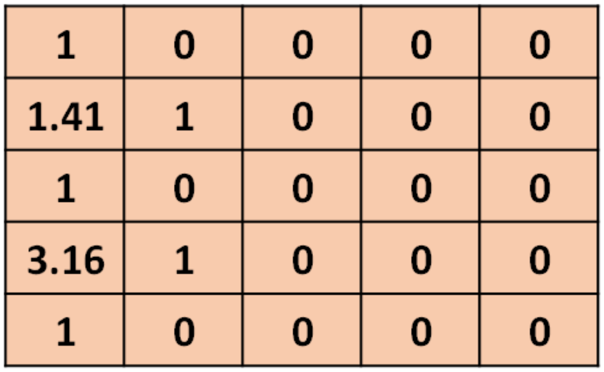

1	0	0	0	0
1.41	1	0	0	0
1	0	0	0	0
3.16	1	0	0	0
1	0	0	0	0

(b) Position error with 9 sensors

Figure 2.7 Prediction position error with different number of sensors

2.5.2. Crack positions

Simulation model in Section 2.3 showed strain distributions when crack presents at the corner of channels. Since temperature and pressure are different between layers, the strain gradient is large between layers. The strain concentration also presents at the top of each channel which is shown in Figure 2.2. Therefore, the top of channels are positions where cracks are easy to be generated. In this section, strain variations induced by crack at the top of channels were learned. The detection accuracy by the proposed nondestructive method when crack presents at the top of channels was calculated.

The simulation flow is the same as that in Section 2.3. Both mechanical load and thermal load were applied on the model. The crack was set at the top of difference channels. Figure 2.8 (a) shows strain distribution when crack presents at the top of one channel. By comparing strain distribution when no crack in the structure at the same loading condition, strain variations induced by crack was calculated as shown in Figure 2.8 (b). It is shown that strain variations radiated from crack position to other positions. The maximum strain variation is at crack position and maximum strain is around 1000 µ. Strain variations are around 1 µ where are 3 channels away from crack position. In the model, the modulus with 5 x 5 channels were extracted as a unit to learn as shown in Figure 2.8 (b). The assumed sensor installation schemes are the same as in Section 2.3 which are shown in Figure 2.6 (a), Figure 2.7 (a) and Figure 2.7 (c).

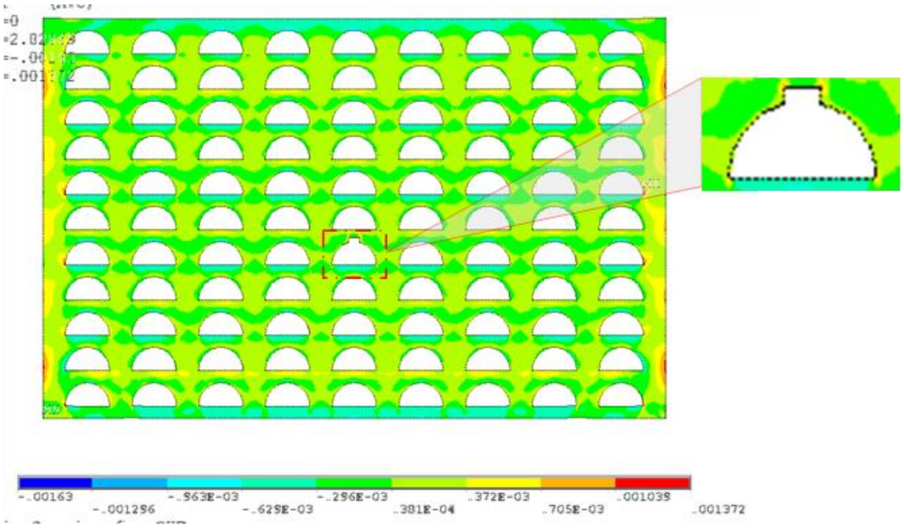

(a) simulation results with vertical crack

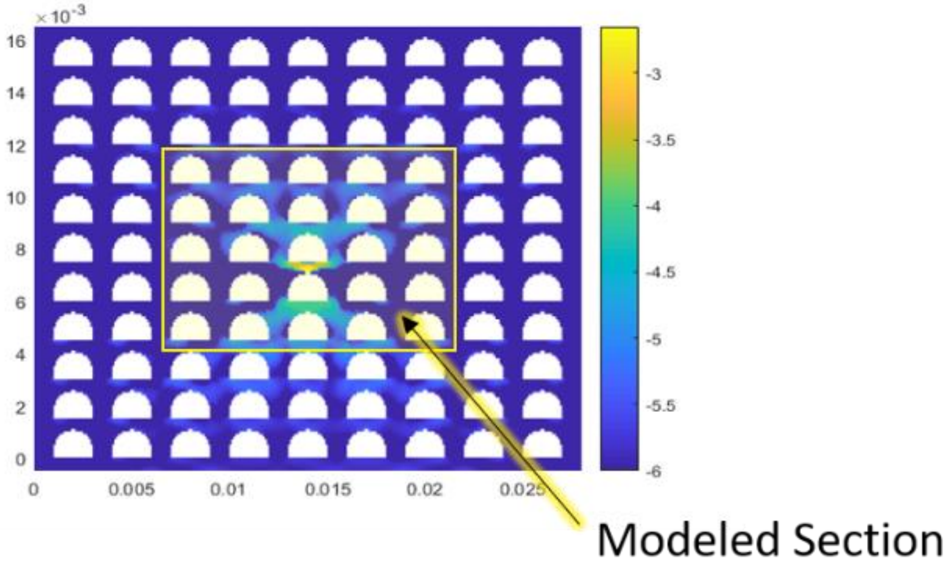

(b) strain variation distribution induced by vertical crack

Figure 2.8 Strain distributions when vertical crack presents in the channel

Figure 2.9 shows detection accuracy with 4, 5 and 9 installed sensors. Detection accuracies when cracks present at the top layer and bottom layer of study unit are higher than at middle layer since sensors are assumed to be installed at the edges of study unit. The strain variations at sensor positions are not high when crack presents at the middle layer. PCHE consists of many study units and the middle layer in this unit can become the top layer or bottom layer for other units. By combining other units, the detection accuracy would be improved. Moreover, Figure 2.9 also demonstrated that the increasing of sensor density can improve accuracy of crack detection. The proposed nondestructive method is also available when crack presents at the top of channels.

1	1	0	1	1
1	0	0	0	1
2.23	1.41	2	1.41	2.23
2.23	0	0	0	2.23
4.12	1	0	1	2

(a) 4 sensors

1	1	0	1	1
1	0	0	0	1
2.23	2.23	1.41	2.23	2.23
1	0	0	0	1
4.12	1	0	1	2.23

(b) 5 sensors

0	0	0	0	0
1	0	0	0	1
1	0	1.41	0	1
0	0	0	0	0
0	0	0	0	0

(c) c) 9 sensors

Figure 2.9 Crack detection accuracy with different number of installation sensors

2.5.3. Crack dimensions

In Section 2.3, the sensitivity matrix was built when crack presents at the corner of each channel. The crack length is set 0.3 mm in simulation to get the sensitivity matrix. In the calculation of detection accuracy, the inputs in the crack retrieval algorithm were from simulations with same crack dimensions. However, the dimensions of crack are hard to know in practical test. In this section, difference dimensions of crack would be regarded as inputs in the crack retrieval algorithm. The detection accuracy with different crack dimensions would be calculated to check universality of the proposed testing method.

Figure 2.10 shows the crack detection accuracy for different crack lengths when 4 sensors were embedded in the structure. The average detection errors when crack length is 0.1 mm, 0.3 mm and 0.5 mm are 1.42, 1.24 and 1.46. When crack length is 0.1 mm, the crack is small and the strain variations induced by crack is not high. The inputs in the crack retrieval algorithm are not as large as simulations with 0.3 mm crack. Therefore, the detection error is higher than that for 0.3 mm crack. When crack length is 0.5 mm, crack is across two channels. The structural characteristic of simulation model is changed. The strain variation distribution induced by crack is different from the model with 0.3 mm length crack. That might be the reason lead to lower detection accuracy than that for 0.3 mm crack. For all these three cases, the detection accuracies are very close to each other. For each channel, the detection accuracies when crack presents with different length are also close to each other.

4.47	**1**	**0**	**1**	**1.41**
0	**1**	**1.41**	**0**	**1**
1	**0**	**1**	**1**	**0**
2.23	**1**	**1.41**	**1.41**	**1**
4.47	**4.12**	**0**	**1**	**4.47**

(a) Crack length: 0.1 mm

3.16	**1**	**0**	**1**	**1.41**
0	**1.41**	**1.41**	**0**	**1**
1	**0**	**1**	**1**	**0**
3.6	**1**	**1.41**	**1.41**	**1**
4	**4.12**	**0**	**1**	**0**

(b) Crack length: 0.3 mm

3.16	**1**	**0**	**1**	**1.41**
0	**1.41**	**3**	**0**	**1**
1	**0**	**1**	**1**	**0**
3.6	**1**	**1**	**1.41**	**1**
4	**4.12**	**0**	**1**	**4.47**

(c) Crack length: 0.5 mm

Figure 2.10. Crack detection accuracy for different crack lengths with 4 sensor installation

Figure 2.11 shows the crack detection accuracy when 9 sensors are embedded in the structure. The average detection errors when crack length is 0.1 mm, 0.3 mm and 0.5 mm are 0.38, 0.44 and 0.72. All detection errors are lower than that in Figure 2.10 since sensor density increases. When crack length is 0.1 mm, the crack detection accuracy is as high as that for 0.3 mm crack. Although strain variations induced by crack are not as high as that for 0.3 mm crack, the increment of sensor density makes strain variations can be detected. When crack length is 0.5 mm, the detection accuracy is lower than that for 0.3 mm which caused by structural characteristic changes. It is known from Figure 2.10 and Figure 2.11 that crack retrieval algorithm which was built with 0.3 mm crack is universal to difference crack dimensions.

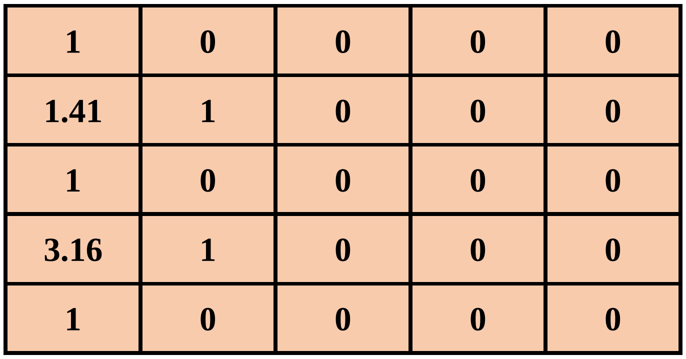

1	**0**	**0**	**0**	**0**
1.41	**1**	**0**	**0**	**0**
1	**0**	**0**	**0**	**0**
3.16	**1**	**0**	**0**	**0**
1	**0**	**0**	**0**	**0**

(a) Crack length: 0.1 mm

1	**0**	**0**	**0**	**0**
1.41	**1.41**	**0**	**0**	**0**
1	**0**	**0**	**0**	**0**
3.16	**1**	**0**	**0**	**1**
1	**0**	**0**	**0**	**0**

(b) Crack length: 0.3 mm

0	**0**	**0**	**0**	**0**
1.41	**3**	**0**	**0**	**3**
1	**0**	**0**	**0**	**0**
3.16	**1**	**1**	**1.41**	**1**
1	**0**	**0**	**1**	**0**

(c) Crack length: 0.5 mm

Figure 2.11 Crack detection accuracy for different crack lengths with 9 sensor installation

2.6. Conclusion

In this paper, a new nondestructive test method was proposed to monitor structure health of compact heat exchanger. This paper focuses on the simulation test of the approach, to quantitatively evaluate the performance of the approach and provide guideline for the experimental validation. Mathematically, the crack retrieval is realized by solving an ill-posed backward problem through two steps: 1) build a forward equation from crack position to sensor measurements by numerically simulating the sensor response to cracks at each possible locations; 2) inverse the mathematical relationship to establish an algorithm estimating crack location from sensor output. A two-dimensional thermal and structure coupling model is built by ANSYS to simulate the strain distribution of heat exchanger with/ without cracks. As the number of strain values sampled by the fiber strain sensors is far less than the possible crack location within a given space, iterative Tikhonov Regularization method is adopted to solve the ill-posed problem. The approach was tested with simulation results from the numerical model. The estimated crack locations are compared with the "true" crack location set in the simulation to quantify the estimation error. Based on a model with 5 x 5 channels, the location of crack can be accurately estimated with an average error less than 0.4 channels. Crack detection accuracies for different crack size, crack position in each channel, and layout of sensors were also discussed. The calculation results show that crack retrieval algorithm also can be applied to detect cracks with different positions and sizes. The increasing of installed sensor density can improve crack detection accuracy. Through simulation test, it is proved that the presence of crack in a multi-channel CHE structure can be detected by limited number of sensors. This work provides an economy and efficient approach to achieve nondestructive detection of compact heat exchanger on the site.

STRAIN TRANSFER CHARACTERISTICS OF SURFACE BONDED FIBER OPTICS SENSOR UNDER THERMAL AND MECHANICAL LOADS

Xiaochen Hu and Zhaoyan Fan

Submitted to *Transaction on Instrumentation and Measurement*

Chapter 3. Strain Transfer Characteristics of Surface Bonded Fiber Optics Sensor Under Thermal and Mechanical Loads

Abstract— Strain transfer ratio is one of the key characteristics to determine the accuracy of sensors for strain measurement and structural health monitoring. This paper presented a theoretical study on the strain transfer ratio of optical fiber sensors, which is generally bonded on the surface of target structure by adhesives. Compared to the prior study from the literatures, this paper first introduced both the temperature variation and the mechanical load in the discussion of strain transfer ratio. The work studied the characteristics of strain transfer ratio for surface bonded fiber optic sensor in two consecutive approaches: 1) A simplified multi-layer analytical model was built to derive the expression of strain transfer ratio as a function of the structural and material properties; 2) Experiments was designed to obtain measured strains of surface-bonded optical fiber sensor under both mechanical and thermal loads. The analytical model was validated by experimental results. A good match has been observed in the comparison of the experimental results and analytical results, with an average relative error 2.4%. It was found in both of the models that the strain transfer ratio is dependent on the thermal and mechanical loads. The derivation of effective sensing length to satisfy the requirement of measurement accuracy, strain variation, and temperature variation was done. Based on the validated analytical model, the discussion was further extended to parametric analysis. The influence factors on strain transfer ratio were analyzed to determine bonding schemes when measurement structure subjects to both mechanical and thermal loads.

Nomenclature

y_c	Radius of coating	L	Half-length of adhesive layer
y_f	Radius of fiber core	D	Width of adhesive layer
y_a	Thickness of adhesive from the central axis of fiber cire to matrix	E_m	Young’s modulus of matrix
y_m	The distance between x axis and matrix	E_a	Young’s modulus of adhesive
σ_f	Normal mechanical stress of fiber	E_c	Young’s modulus of coating
σ_c	Normal mechanical stress of coating	E_f	Young’s modulus of fiber
σ_a	Normal mechanical stress of adhesive	G_m	Shear modulus of matrix
$\sigma_{t,f}$	Thermal stress in the fiber	G_a	Shear modulus of adhesive
$\sigma_{t,c}$	Thermal stress in the coating	G_c	Shear modulus of coating
$\sigma_{t,a}$	Thermal stress in the adhesive	G_f	Shear modulus of fiber
$\sigma_{t,m}$	Thermal stress in the matrix	ΔT	Temperature variation
τ_c	Shear stress in the coating	φ_m	CTE of matrix
τ_a	Shear stress in the adhesive	φ_a	CTE of adhesive
τ_m	Shear stress in the matrix	φ_c	CTE of coating
τ_{cf}	Shear stress between coating and fiber	φ_f	CTE of fiber
h_a	Adhesive above fiber coating		

3.1. Introduction

Optical fiber strain sensor has been a widely adopted device for measuring strain and structural deformation in the past decades, due to the light weight, small size, and immunity to electromagnetic interference compared with other measurement systems [23], [24]. According to the working principles, fiber strain sensors can be classified into two categories:

1) Fiber Bragg Grating (FBG) sensors, generally measuring strain at fixed locations on the fiber core where a series of gratings are fabricated. The grates reflect the incident light at a given wavelength determined by the strain applied to the fiber;

2) Rayleigh, Brillouin, and Raman backscattering sensors, making use of the inhomogeneity of the fiber as reflectors to measure the wavelength variation of the reflected light and consequentially determine the strain with high spatial resolution.

The strain resolution of both two types of fiber sensors is capable of reaching sub-micro strain level [25]. For the backscattering sensors, the spatial resolution can reach up to 1~2 samples per millimeter [26], [27]. The maximum operation temperature is improved from 200℃ to above 800℃. The improvement of sensing capability has enabled the optical fiber sensors being used in detecting structure health in millimeter scale within harsh environments [28], [29]. Literature has reported embedding the fiber sensors in compact heat exchanger [30], pipelines [31], and superconductor magnets [32] in multiple applications.

The performance of fiber optic sensor is determined by the material and its structure. Generally, an optical fiber sensor is composed of a silicon core of 120 ~ 150 μm diameter and a coating layer of about 150 μm thick made of polyimide, acrylate, or metals such as gold. In the application where the optical fiber sensors are used for measuring strain or stress in a host matrix, the fiber is generally attached on the matrix surface by adhesives. When the host matrix is being stretched, compressed, or bent, the adhesive transfers the deformation via the coating layer to the fiber core, where the strain was read through wavelength variation measurement. During the process of strain transfer from the target structure surface to the fiber core, the strain values may be different at each layer due to multiple factors such as adhesive layer thickness, coating layer thickness, material properties, and temperature variation. To study the accuracy of strain measurement, the concept of strain transfer ratio was introduced to express the ratio between the strain measured by the fiber core and the actual value in the target structure. In the priori research, significant efforts have been made to quantify the relationships from the sensor installation parameters to the strain transfer ratio with different sensor bonding schemes and loading types. There are two sensor bonding schemes for measuring strain of matrix, one is bonding sensor on the surface of matrix to measure surface strains, another is embedding sensors in the matrix to get strains inside matrix. For the surface bonding scheme, the theoretical model usually includes fiber core, coating layer, adhesive and matrix. The analyzed models are not symmetry. Some scholars studied the strain transfer mechanism by experimental method and computer simulation. Betz applied finite element analysis to get strain distribution of surface bonded fiber sensor and matrix and then verified the analysis by experiments. He found only thin and stiff coatings can guarantee an optimum strain transfer into fiber [33]. Lin et al. applied finite element analysis and experimental method to study strain transmission efficiency of surface bonded FBG sensors [34]. They found the recoating and steel-tube packaging markedly effect strain transfer efficiency. When the thickness of adhesive is less than the diameter of fiber, the influence of thickness on strain transfer is less. The theoretical method is also developed to study the strain transfer mechanism of surface bonded fiber. Zhang et al. designed a theoretical strain transfer model for distributed optical fiber sensors bonded on the surface of matrix. An increased strain transfer ratio was observed when the shear modulus of fiber coating and bonded length is increased [35]. Her et al. developed a theoretical model to evaluate the strain transferred from host material to optical fiber [36]. It was found that the strain transfer ration increases with the bonded length and the stiffness of the coating layer. Wang et al. presented the traditional strain transfer model is not suitable in cases the host material is anisotropic. They proposed a new strain transfer model for FBG sensors bonded to the surface when the host material is composite laminates [37].

For the sensor embedded scheme, the analysis structure includes fiber core, coating, adhesive and matrix which is same as surface bonded scheme. The analyzed models are simplified as a cylinder under axial loading. Li et al. developed an analytical model for embedded FBG sensors in different host materials and found the shear modulus of the host material influence the strain transmission [38]. Wang and Xiang considered sensor bonding influence on the matrix strain and calculate the strain transfer in the matrix by introducing Goodman’s hypothesis to build a strain transfer model [39]. Li et al. studied the effects of the geometry and the relative stiffness of matrix on strain transfer ratio for embedded FBG sensors.

Besides studying strain transfer mechanism considering bonding scheme, loading type on the measurement system has significant effect. Wang et al. studied strain transfer characteristic of FBG sensors attached on steel structure subjected to fatigue loading. They found the train transfer ratio under fatigue response is much lower than that in static state [40]. Feng et al. studied strain transfer mechanism in Brillouin-based sensors when crack presents in the matrix during measurement by considering elastic and elastoplastic stages in the model [41]. The technique was expected to improve the accuracy of crack detection and localization. Yi et al. studied strain transfer mechanism of surface bonded FBG sensor subject to dynamic load. They found the bonding length, the thickness of adhesive and coating have major impacts on dynamic strain transfer. Also, the relationship between vibration frequency and system natural frequency would influence strain transfer ratio [42]. In addition to the mechanical properties and loads transferred from the host matrix, the readings of optical fiber sensor also subject to the temperature variation, due to the stress induced by thermal expansions of the host material, adhesive, coating, and fiber core. Wang et al. presented a strain transfer analysis for the surface bonded FBG sensor subject to thermal loading from 30℃ to 70℃ without considering the mechanical load [43].

It has been observed in the literatures that most of the work focused on the discussion of strain transfer ratio with single type of load, either mechanical load from the host matrix or the thermal load from temperature variation. When the system is subjected to mechanical load, the load is applied on the matrix and then transfers from matrix to fiber core via adhesive and coating layer. When the system is subjected to thermal load, fiber core, coating, adhesive and matrix expose to load simultaneously. The differences of coefficients of thermal expansion lead to differences of thermal stress in each layer. The different thermal stresses transfer between joint layers. Therefore, the strain transfer mechanism and gradient are not the same for mechanical load and thermal load. The previous approaches would satisfy most of the applications where the strain is measured at consistent temperature or with small temperature variation below 100℃. However, with the wide application of fiber sensors in manufacturing processes, some of the scenarios, such as monitoring diffusion bonding process or the health status of compact heat exchangers [30], requires accurate strain measurement within a large temperature variation up to 500℃. Determining the strain transfer ratio requires considering both the mechanical and thermal load simultaneously in the model which was not covered in the prior theoretical or experimental studies. To fill this gap, this paper presented a theoretical approach quantify the expression of strain transfer ratio for the optical fiber sensors under both mechanical and thermal loads. A simplified multi-layer model including the fiber core, coating, adhesive and host matrix was built to derive the relationships between the strain transfer ratio and the key factors such as temperature variation, matrix strain, adhesive layer thickness, bonding length, etc. Based on the analytical model, the expression of effective sensing length for the optical fiber sensor to obtain accurate strain measurements has been derived as a function of those key factors. The relationships between measured strains and true strains on the surface of matrix were verified by a series of experiments when matrix subjects to both mechanical and thermal loads. Finally, the parametric analysis was done to characterize strain transfer ratio with sensor bonding related parameters. The bonding scheme can be determined based on parametric analysis.

The rest of the paper was organized as follows: Section II introduced the analytical model of the optical fiber sensor. The strain transfer ratio was expressed as a function of the material properties, key installation dimensions, mechanical load, and thermal load. The effective sensing length when temperature variation is unknown is evaluated. Experiments were conducted in Section III to verify the derived analytical model. Strains from experimental results and theoretical calculation were compared and analyzed. The study of parameters related to sensor installation based on the analytical model was presented in Section IV. Finally, a conclusion was presented in Section V.

3.2. Strain analysis of optical fiber

The basic structure of optical fiber strain sensors includes fiber core and coating. For measuring strains on the matrix, strain sensors need to be glued on the matric by adhesive. When mechanical load is applied on the matrix, strains generated on matrix would transfer from matrix surface to fiber core through adhesive and fiber coating. The transferred strains are less than strains on the matrix surface. When thermal load is applied on the system, all materials (matrix, adhesive, fiber coating and fiber core) would deform spontaneously depends on their coefficient of thermal expansion. The thermal strain transfer direction is not sure which can be from matrix to fiber or from fiber to matrix. Although strain transfer gradient is not sure, all strain transfers follow mechanical equilibrium no matter mechanical load or thermal load is applied. Therefore, the analytical model can be built under both mechanical load and thermal load.

3.2.1. Analytical Model

Figure 3.1 (a) shows the physical model where an optical fiber sensor is applied to measure strain on matrix surface. The optical fiber sensor is composed of a fiber core and a layer of protective coating. A section of the fiber sensor (length: 2L) is bonded on the matrix by adhesive of width D. To calculate the strain transfer ratio, the physical model was simplified into a 2-dimentional model along the vertical cross section passing through the axis of the fiber core, as shown in Figure 3.1 (b). In the simplified model, the origin of the coordinate system is set at the center of fiber core. The x and y axes are set along the central axis of the fiber core and the along the vertical symmetry axis of the structure, respectively. There are in total four components presented in the simplified model: 1) adhesive 2) the fiber core, 3) fiber coating, and 4) the host matrix, respectively. The radius of fiber core and protective coating is y_f and y_c, respectively. The thickness of adhesive from the central axis of fiber core to matrix is y_a. The thickness of adhesive above the coating is h_a. The distance between the x axis and matrix is y_m. Variables σ_f, σ_c, σ_a are the normal mechanical stress in the fiber core, coating and adhesive layers. $\sigma_{t,f}$, $\sigma_{t,c}$, $\sigma_{t,a}$, $\sigma_{t,m}$ are the thermal stress in the fiber core, coating, adhesive, and matrix layers, respectively. Variables $\tau_c(x,y)$, $\tau_a(x,y)$, $\tau_m(x,y)$ are the shear stress in the coating, adhesive, matrix, respectively. $\tau_{cf}(x,y)$ is the shear stress between the coating and fiber core. In the derivation of the analytical model, the following assumptions were made based on the physics of the realistic model:

- There is no relative sliding between different material layers.
- The only elastic deformation is considered in all the layers
- All materials in the model are isotropic.

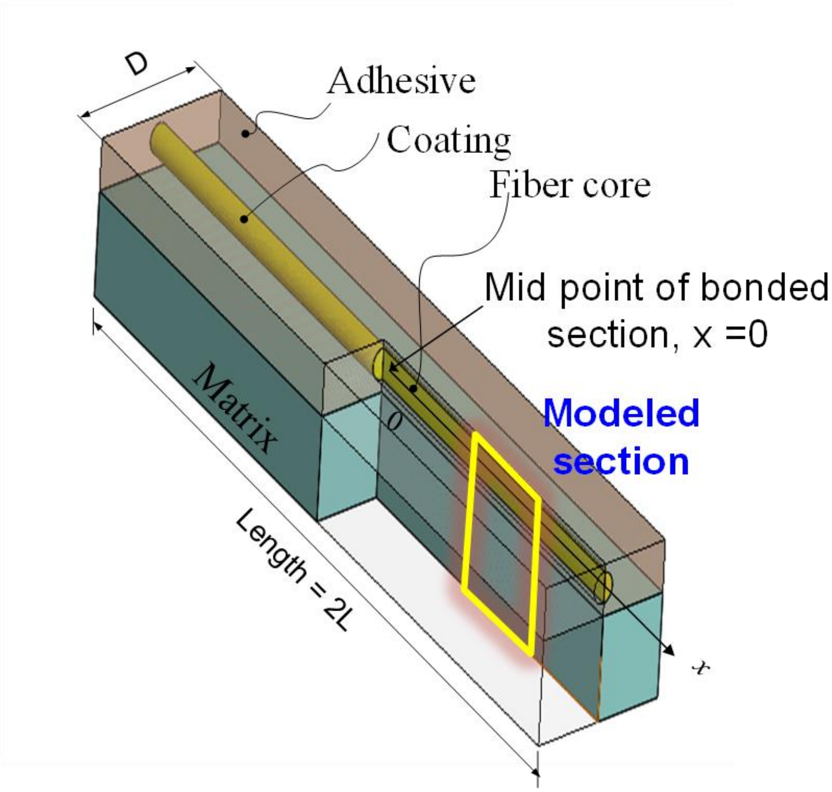

(a) The structure of strain measurement by surface bonded fiber sensor

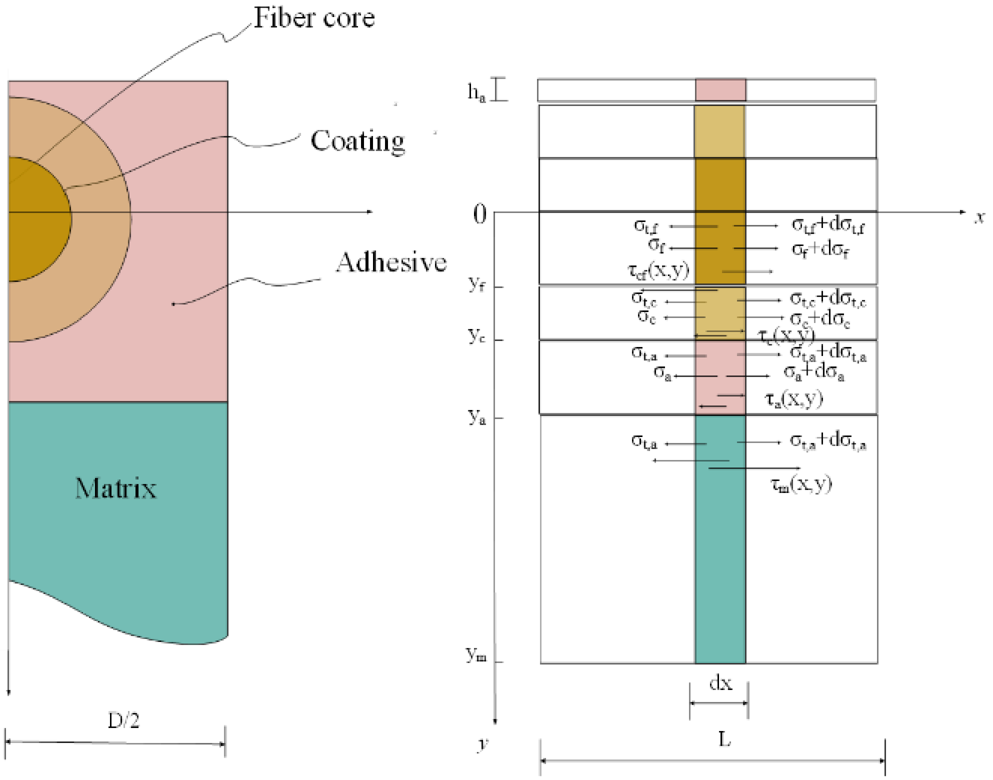

(b) Coordinate system of measurement structure and stress distribution

Figure 3.1 Analytical model of the optical fiber strain sensor bonded to a host matrix through adhesive

Based on mechanical equilibrium, the shear stress in the fiber core can be obtained as:

$$\tau_{cf}(x,y) = -\frac{y_f}{2}\cdot\frac{d\sigma_f + d\sigma_{t,f}}{dx} \tag{3.1}$$

Similarly, the shear stress in the fiber coating is expressed as:

$$\tau_c(x,y) = -\left(\frac{y_f^{\,2}}{2y}\cdot\frac{(d\sigma_f + E_f\phi_f\cdot\Delta T)}{dx} + \frac{(y^2 - y_f^{\,2})}{2y}\cdot\frac{(d\sigma_c + d\sigma_{t,c})}{dx}\right) \tag{3.2}$$

The shear stress in the adhesive layer can be expressed as:

$$\tau_a(x,y) = -[\frac{\pi {y_f}^2}{D} \cdot \frac{(d\sigma_f + E_f \phi_f \cdot \Delta T)}{dx} + \frac{\pi({y_c}^2 - {y_f}^2)}{D} \cdot \frac{(d\sigma_c + E_c \phi_c \cdot \Delta T)}{dx}]$$
$$-[(\mathrm{h_a} + y_\mathrm{c} + y) - \frac{\pi {y_\mathrm{c}}^2}{D}] \cdot \frac{(d\sigma_a + d\sigma_{t,a})}{dx} \tag{3.3}$$

For the matrix, the shear stress can be obtained as:

$$\tau_m(x,y) = \tau_\mathrm{a}(x, y_a) - (y - y_a) \cdot \frac{(d\sigma_m + d\sigma_{t,m})}{dx} \tag{3.4}$$

In the matrix layer, when y is larger or equal to y_m is true, which means the stress distribution is not influenced by the bonded fiber sensor, the following boundary condition is applied:

$$\tau_m(x, y_m) = 0 \tag{3.5}$$

By substituting Eq. (3.5) into Eq. (3.4), the shear stress in the matrix layer can be further expressed as:

$$\tau_m(x,y) = (1 - \frac{y - y_a}{y_m - y_a}) \cdot \tau_a(x, y_a) \tag{3.6}$$

Based on the shear-lag theory, the relative displacement of different layers is determined by the shear strain. Therefore, the relative displacement in continuously layer are calculated as following:

$$\begin{cases} u(x,y_c) - u(x,y_f) = \int_{y_f}^{y_c} \gamma_c(x,y)\,\mathrm{dy} \\ u(x,y_a) - u(x,y_c) = \int_{y_c}^{y_a} \gamma_a(x,y)\,\mathrm{dy} \\ u(x,y_m) - u(x,y_a) = \int_{y_a}^{y_m} \gamma_m(x,y)\,\mathrm{dy} \end{cases} \tag{3.7}$$

According to the second assumption that all materials are linear elastic and Hook’s law, the relationship between shear stress and shear strain can be obtained:

$$\gamma = \frac{\tau}{G} \tag{3.8}$$

where G is shear modulus, γ is shear strain and τ is shear stress.

Similarly, the relationship between thermal stress and thermal strain can be obtained as:

$$\sigma_t = E\varepsilon_t = E \cdot \phi \Delta T \tag{3.9}$$

where ε_t is thermal strain, E is Young's modulus, φ is CTE and ΔT is temperature variation.

By taking the derivative with respect to x, total strain can be obtained. In this mode, the total strain is composed of mechanical strain and thermal strain. By substituting Eqs. (3.8-3.9) into deduced Eq. (3.7) with respect to x, normal mechanical strain and thermal strain can be obtained as:

$$\begin{cases} \dfrac{du(x,y_c)}{dx} - \dfrac{du(x,y_f)}{dx} = \varepsilon(x,y_c) + \phi_c \Delta T - \varepsilon(x,y_f) - \phi_f \Delta T \\ \qquad = \dfrac{1}{G_c} \displaystyle\int_{y_f}^{y_c} \dfrac{\tau_c(x,y)}{dx} dy \\ \dfrac{du(x,y_a)}{dx} - \dfrac{du(x,y_c)}{dx} = \varepsilon(x,y_a) + \phi_a \Delta T - \varepsilon(x,y_c) - \phi_c \Delta T \\ \qquad = \dfrac{1}{G_a} \displaystyle\int_{y_c}^{y_a} \dfrac{\tau_a(x,y)}{dx} dy \\ \dfrac{du(x,y_m)}{dx} - \dfrac{du(x,y_a)}{dx} = \varepsilon(x,y_m) + \phi_m \Delta T - \varepsilon(x,y_a) - \phi_a \Delta T \\ \qquad = \dfrac{1}{G_m} \displaystyle\int_{y_a}^{y_m} \dfrac{\tau_m(x,y)}{dx} dy \end{cases} \tag{3.10}$$

Based on the first assumption, each layer is bonded together perfectly, the fiber is strained together with the interlayer. Therefore, the strain gradients are expected to be of the same order which can be expressed as:

$$\frac{d\varepsilon_f}{dx} \cong \frac{d\varepsilon_c}{dx} \cong \frac{d\varepsilon_a}{dx} \cong \frac{d\varepsilon}{dx} \tag{3.11}$$

By substituting Eq. (3.2-3.4) into Eq. (3.10), Eq. (3.12) can be obtained:

$$\begin{cases} \varepsilon(x,y_c) + \phi_c \Delta T - \varepsilon(x,y_f) + \phi_f \Delta T = -(k_1 \dfrac{d^2\varepsilon}{dx^2} + w_1 \dfrac{d^2T}{dx^2}) \\ \varepsilon(x,y_a) + \phi_a \Delta T - \varepsilon(x,y_c) + \phi_c \Delta T = -(k_2 \dfrac{d^2\varepsilon}{dx^2} + w_2 \dfrac{d^2T}{dx^2}) \\ \varepsilon(x,y_m) + \phi_m \Delta T - \varepsilon(x,y_a) + \phi_a \Delta T = -(k_3 \dfrac{d^2\varepsilon}{dx^2} + w_3 \dfrac{d^2T}{dx^2}) \end{cases} \tag{3.12}$$

where

$$\begin{cases} k_1 = \dfrac{2y_f{}^2 \ln(\dfrac{y_c}{y_f})\, \mathrm{E}_f + [(y_c{}^2 - y_f{}^2) - 2y_f{}^2 \ln(\dfrac{y_c}{y_f})]\, \mathrm{E}_c}{4G_c} \\ k_2 = \dfrac{y_a - y_c}{G_a}[\dfrac{\pi y_f{}^2 E_f + \pi(y_c{}^2 - y_f{}^2)\, \mathrm{E}_c}{D} \\ \qquad + (\mathrm{h}_a + \dfrac{3}{2} y_c + \dfrac{1}{2} y_a - \dfrac{\pi y_c{}^2}{D})\, \mathrm{E}_a] \\ k_3 = \dfrac{1}{2}\dfrac{(y_m - y_a)}{G_m}[\dfrac{\pi y_f{}^2 E_f + \pi(y_c{}^2 - y_f{}^2)\, \mathrm{E}_c}{D} \\ \qquad + (\mathrm{h}_a + y_c + y_a - \dfrac{\pi y_c{}^2}{D})\, \mathrm{E}_a] \end{cases}$$

$$\begin{cases} w_1 = \dfrac{2y_f{}^2 \ln(\dfrac{y_c}{y_f})\, \mathrm{E}_f\, \phi_f + [(y_c{}^2 - y_f{}^2) - 2y_f{}^2 \ln(\dfrac{y_c}{y_f})]\, \mathrm{E}_c\, \phi_c}{4G_c} \\ w_2 = \dfrac{y_a - y_c}{G_a}[\dfrac{\pi y_f{}^2 E_f \phi_f + \pi(y_c{}^2 - y_f{}^2)\, \mathrm{E}_c\, \phi_f}{D} \\ \qquad + (\mathrm{h}_a + \dfrac{3}{2} y_c + \dfrac{1}{2} y_a - \dfrac{\pi y_c{}^2}{D})\, \mathrm{E}_a\, \phi_a] \\ w_3 = \dfrac{1}{2}\dfrac{(y_m - y_a)}{G_m}[\dfrac{\pi y_f{}^2 E_f \phi_f + \pi(y_c{}^2 - y_f{}^2)\, \mathrm{E}_c\, \phi_c}{D} \\ \qquad + (\mathrm{h}_a + y_c + y_a - \dfrac{\pi y_c{}^2}{D})\, \mathrm{E}_a\, \phi_a] \end{cases}$$

By simplifying the simultaneous equations in Eq. (3.12), the strain in the fiber core can be described by a 2nd order differential equation, expressed as:

$$\frac{d^2\varepsilon_f}{dx^2} - k^2\varepsilon_f = -k^2\varepsilon_m - k^2(\phi_m - \phi_f)\cdot\Delta T + (w_1 + w_2 + w_3)\frac{d^2T}{dx^2} \tag{3.13}$$

where

$$k = \frac{1}{\sqrt{k_1 + k_2 + k_3}}$$

In this paper, the measurement system is considered in the constant temperature environment. The dynamic temperature variation is not considered. Therefore, $d^2T/dx^2=0$, Eq. (3.14) can be obtained as:

$$\frac{d^2\varepsilon_f}{dx^2} - k^2\varepsilon_f = -k^2\varepsilon_m - k^2(\phi_m - \phi_f)\cdot\Delta T \tag{3.14}$$

Equation (3.14) is a non-homogeneous linear differential equation, the general solution is:

$$\varepsilon_f(x) = C_1 e^{kx} + C_2 e^{-kx} + \varepsilon_m + (\phi_m - \phi_f)\cdot\Delta T \tag{3.15}$$

The fiber is assumed to be free from axial stress at both ends since the matrix material doesn’t contact the fiber beyond the ends of the interface. The strain transferred from host matrix to the fiber is zero at two ends. Therefore, the boundary conditions are:

$$\varepsilon_f(\mathrm{L}) = \varepsilon_f(-\mathrm{L}) = 0 \tag{3.16}$$

where x=L, x=-L are two ends of fiber. By substituting Eq. (3.16) into Eq. (3.15), C1 and C2 can be calculated, the strain transfer from matrix to fiber is obtained as following:

$$\varepsilon_f(x) = -\frac{\varepsilon_m(x) + (\phi_m - \phi_f)\cdot\Delta\mathrm{T}}{e^{kL} + e^{-kL}}(e^{kx} + e^{-kx}) + \varepsilon_m(x) + (\phi_m - \phi_f)\cdot\Delta T \tag{3.17}$$

Therefore, the strain transfer ratio of total strain in fiber to total strain in matrix can be calculated as:

$$R = \frac{\varepsilon_f + \phi_f \Delta T}{\varepsilon_m + \phi_m \Delta T} = 1 - \frac{\cosh(kx)}{\cosh(kL)} + \frac{\phi_f \Delta T}{\varepsilon_m + \phi_m \Delta T} \cdot \frac{\cosh(kx)}{\cosh(kL)} \tag{3.18}$$

3.2.2. Case Discussion

Equation 3.18 shows that the strain transfer ratio is composed of three major components, as given on the right side of the equation. The first two components [1-cosh(kx)/cosh(kL)] is the term that is fully determined by the mechanical load on the matrix, which is consistent with prior work [36],[38] where there is no temperature variation considered. The third component shows that when the temperature variation is considered in the strain measurement, the strain transfer ratio is co-determined by the temperature, thermal expansion, and the strain (ε_m) induced by the mechanical force load applied to the matrix. As this component has both ε_m and ΔT in the denominator, it indicates that the thermal and mechanical loads are not independent factors affecting the strain transfer ratio but coupled together:

Case 1: When the mechanical load induced strain is far higher than thermal load induced strain, namely $\varepsilon_m >> \phi \Delta T$, the third term on the right side of Eq (3.18) is approaching zero. Accordingly, the strain transfer ratio can be simplified into a function of location *x,* expressed as.

$$R = \frac{\varepsilon_f + \phi_f \Delta T}{\varepsilon_m + \phi_m \Delta T} = 1 - \frac{\cosh(kx)}{\cosh(kL)} \tag{3.19}$$

In this case, the strain transfer ratio is only determined by the axial location *x* on the bonded section. This expression is consistent with the discuss in research [36],[38] where only the mechanical load is considered in the calculation of strain transfer ratio.

Case 2: When the mechanical load induced strain is far lower than that of the thermal load, namely $\varepsilon_m << \phi \Delta T$, the term ε_m can be ignored in third term on the right side of Eq. (3.18). Accordingly, the expression of strain transfer ratio can be simplified as the form:

$$R = \frac{\varepsilon_f + \phi_f \Delta T}{\varepsilon_m + \phi_m \Delta T} = 1 - \frac{\cosh(kx)}{\cosh(kL)} + \frac{\phi_f}{\phi_m} \cdot \frac{\cosh(kx)}{\cosh(kL)} \tag{3.20}$$

In this case, the strain transfer ratio is determined by the axial location x on the bonded section and CTE of fiber core and matrix.

Case 3: When the mechanical load induced strain is approaching the same order of magnitude with the thermal load induced strain. Neither of the two terms, ε_m *or* $\phi \Delta T$, can be ignored. The expression of strain transfer ratio remains consistent with Eq. (3.18). Accordingly, in this cases, the strain transfer ratio is affected by thermal load and mechanical load. In another word, if the fiber sensor is used for determining strain value ε_m in a temperature varying environment, and the value of ε_m *and* $\phi \Delta T$ are on the same levels, theoretically, the actual value of strain transfer ratio cannot be determined if the temperature variation is unknown. However, since both mechanical strain ε_m and temperature variations ΔT have limitations during practical measurement, the range of $\varepsilon_m / \phi \Delta T$ can be determined based on measurement limitations. For example, for most of commercial optical fiber measurement system, the maximum readable strain depending on measurement range is usually 10000 με, and minimum readable strain depending on resolution is 1 με [18]. For the optical fiber sensors with polyimide coating, the maximum operation temperature is around 200℃ [18]. The operation temperature can reach to 600℃ for optical fiber sensors with gold coating. Therefore, the ratio of $\varepsilon_m / \phi \cdot \Delta T$ can be calculated based on the limitations of operation temperature and readable strain values. By determining the range of strain transfer ratio, the measurement error can be evaluated and the sensing length under tolerance can be determined which is described in Part 3.2.3.

3.2.3. Effective sensing length

Although, theoretically it is impossible to determine the actual value of strain transfer ratio without knowing the temperature variation, if the maximum range for the strain and temperature can be estimated, an approximation of strain transfer ratio can be calculated by considering a tolerance range δ.

$$\left|[1-\frac{\cosh(kx)}{\cosh(kL)}]-R\right| \le \delta \tag{3.21}$$

When the temperature variation is unknown during test, the true strain value at different measurement location on the matrix surface can be calculated based on the strain transfer ratio without considering temperature variation (when ΔT=0 in Eq. (3.18) within a tolerance. In order to get accurate measurements, a certain tolerance δ from 1 is given to evaluate reliable measurement location which is defined as effective sensing length. By substituting the Eq. (3.20) into Eq. (3.21), the effective sensing length that can be applied to measure strain on the structure is obtained:

$$\frac{-\delta \cdot \cosh(kL) \cdot (\varepsilon_m + \phi_m \Delta T)}{\phi_f \Delta T} \le \cosh(kx) \le \frac{\delta \cdot \cosh(kL) \cdot (\varepsilon_m + \phi_m \Delta T)}{\phi_f \Delta T} \tag{3.22}$$

Let

$$Q = \frac{\delta \cdot \cosh(kL) \cdot (\varepsilon_m + \phi_m \Delta T)}{\phi_f \Delta T} \tag{3.23}$$

Then, the measurement location x is constrained by:

$$\cosh(kx) \leq Q \tag{3.24}$$

In Eq. (3.24), Q is a function related to the ratio of mechanical strain to temperature variation. As it is discussed in the Part 3.2.2, there is a range of Q when the ratio of mechanical strain to temperature variation has limitations. When the temperature variation reaches the maximum operation temperature of sensing system and minimum strain reaches the measurement resolution, Q has a minimum value:

$$Q_{\min} = \frac{\delta \cdot \cosh(kL) \cdot (\frac{\varepsilon_{m\_\min}}{\Delta T_{\max}} + \phi_m)}{\phi_f} \tag{3.25}$$

When the mechanical strain is much higher than temperature variation, the ratio of mechanical strain to temperature variation is infinity which leads to the value of Q is infinite. Since cosh(kx) is a monotonically increasing function when x>0 as shown in Figure 3.2, there is a range of effective measurement position based on the range of Q. It shows that as long as the measurement location x in the bonded section is less than $x_{\min}$, the strain transfer ratio will be controlled within the tolerance range from the ideal value 1. Such a relationship can be used for determining the sensor installation schemes for high precision strain measurement.

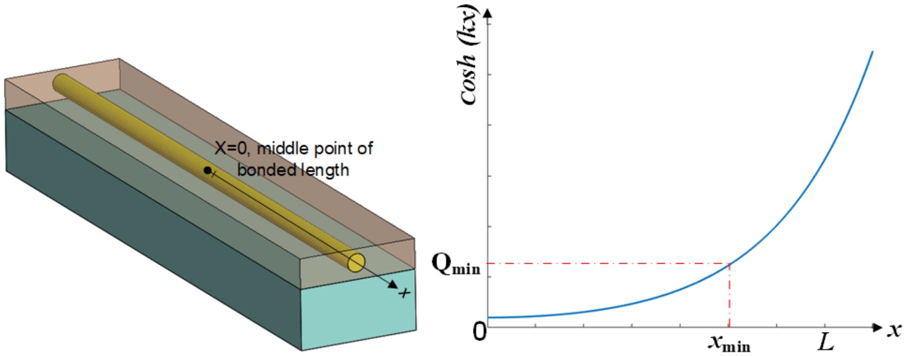

Figure 3.2 Effective measurement length based on strain transfer ratio without considering temperature influence

3.3. Experimental verification

To validate the strain transfer characteristics resulted from the theoretical model, a series of experiments were conducted on an equal stress beam, which provides uniform stress/strain distribution along the optical fiber sensor.

3.3.1. Experimental setup

Equal-stress beam usually adopts a triangular structure. When a vertical load is applied to the tip of the beam, the tension strains are consistent in each cross section along the axis of the beam. Figure 3.3 (a) shows the design of the equal-stress beam used in this study. The wide (right) end of the beam were fixed on a metal rod. A section of the fiber optic sensor, 180 mm long, was bonded in the middle section of the equal-stress beam, along the axis. At the center of the narrow (left) end, a certain weight is loaded along the vertical direction. Based on the working principle of the equal-stress beam, the stress on the surface of beam can be calculated as [35]:

$$\sigma = {6FL}/{mt^2} \tag{3.26}$$

where F is the load applied on beam; L is the length from load position to the end of the beam; *m* is the maximum width of equal stress beam; and t is the beam thickness. The dimension of the beam, as seen in Figure 3.3 (a), is designed to generate 304µ of strain when a maximum of 1.5 kg weight is applied on the narrow end.

Thermal loads on the equal stress beam were provided through rising in ambient temperature by a walk-in oven. The thermal strains of equal stress beam can be calculated by CTE of materials:

$$\varepsilon_{thermal} = \phi \cdot \Delta T \tag{3.27}$$

Therefore, the total strains on the surface of equal stress beam can be obtained:

$$\varepsilon_{total} = \varepsilon_{mechanical} + \varepsilon_{thermal} \tag{3.28}$$

A distributed optical fiber sensor with polyimide coating was bonded along the equal stress beam to obtain strain measurements. Figure 3.3 (b) shows the bonding scheme of optical fiber sensor. Tapes were applied to fix the optical fiber sensor on the surface of beam and determine the bonding length, width and thickness. The geometrical parameters of measurement structure are shown in Table 3.1.

Table 3.1 Geometrical parameters of the measurement structure

Parameter/unit	Symbol	Value
Half-length of adhesive layer/mm	L	90
Width of adhesive layer/mm	D	2
Radius of fiber/µm	y_f	62.5
Radius of coating/µm	y_c	77.5
Thickness of adhesive layer below *x* axis/ mm	y_a	0.5
Adhesive above fiber coating/ mm	h_a	2

Thickness of matrix/ mm	y_m	3

The experiments adopted LUNA ODISIB system to measure the strain via fiber optic sensor. The system is able to determine strain along the fiber every 0.65 mm with a resolution of 1µ [18].

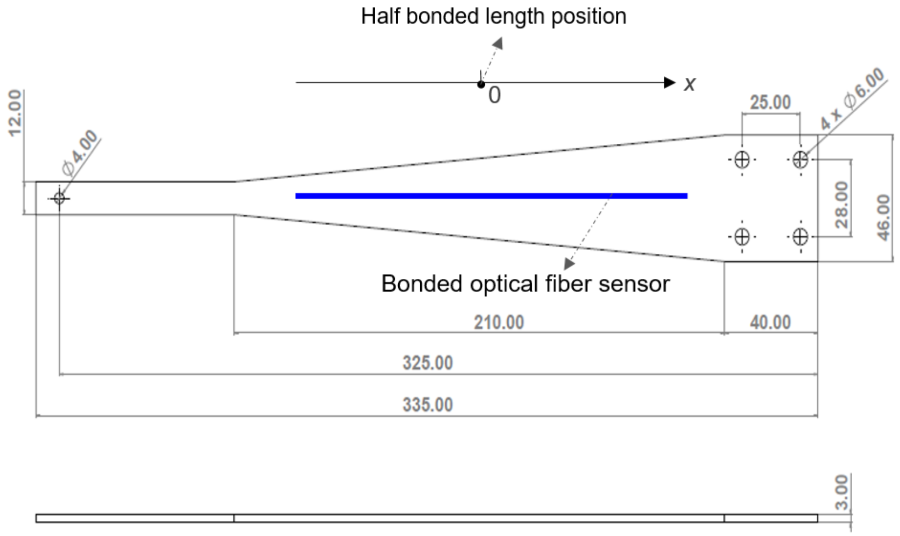

(a) Dimensions of equal strength beam

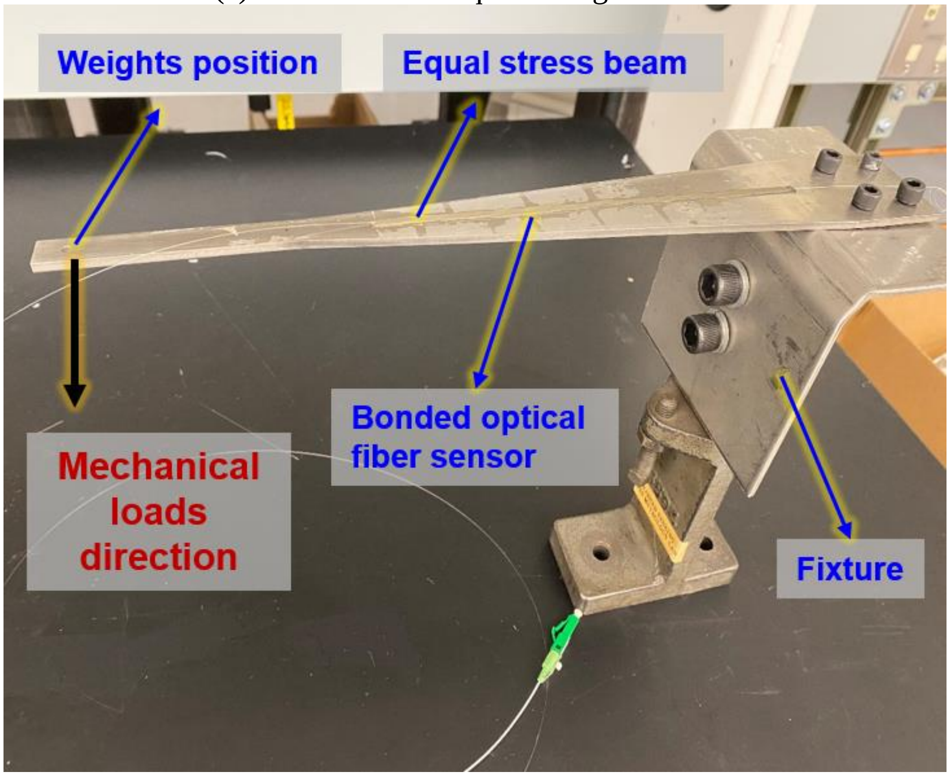

(b) The installation scheme of fiber sensor
Figure 3.3 Equal strength beam for measurement accuracy test

The experimental setup is shown in Figure 3.4, where a walk-in oven was applied to provide thermal loads on the measurement setup. According to the temperature range of the oven, the test temperatures were set from 25℃ to 220℃, at an increment of 65℃. By subtracting the base temperature 25℃, the temperature variation is calculated from 0℃ to 195℃. The mechanical load was added by hanging weights at the end of equal stress beam. Table 3.2 shows the mechanical and thermal load applied to the whole setup. A full factorial design of experiment was adopted to obtain the strain measurements under all the thermal/mechanical loads combinations.

Table 3.2 Experimental parameters

Variables	Values

Mechanical load (N)	0, 14.7, 24.5, 34.3
Temperature variations (℃)	0, 65, 130, 195

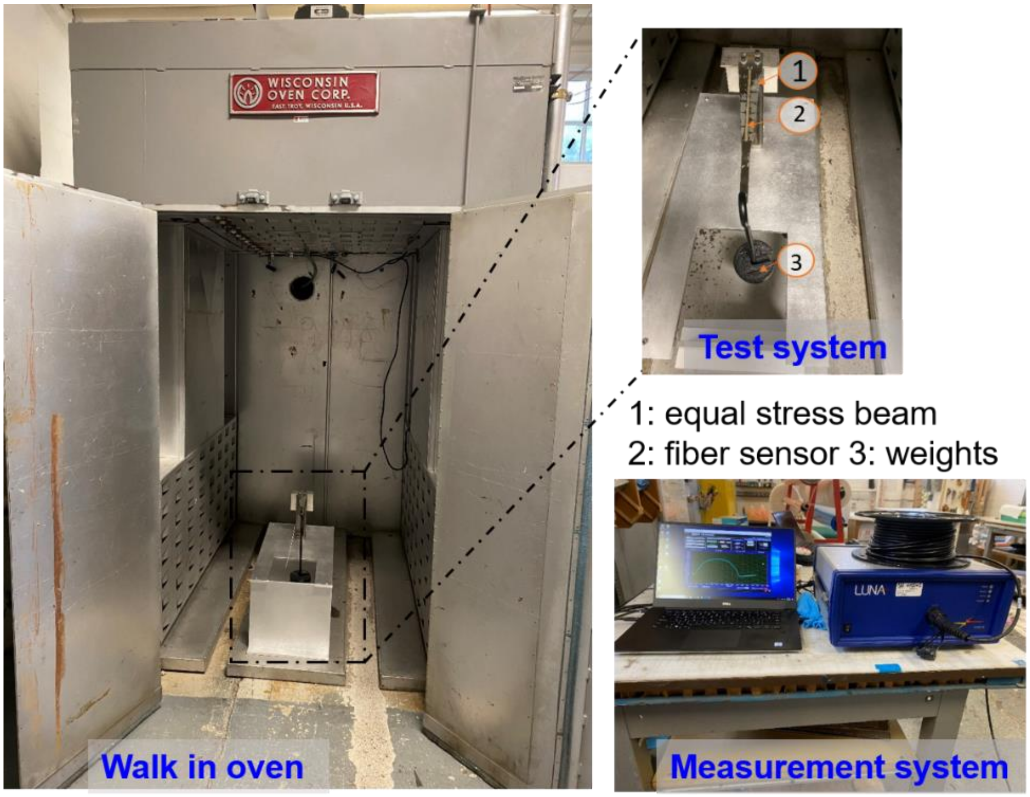

Figure 3.4 Experimental setup

3.3.2. Experimental results

Figure 3.5 (a)-(d) shows the strain at different locations along the fiber sensor from the middle point to the end of the bonded section. The mechanical properties of the measurement structure are shown in Table 3.3. One thing need to be noticed in Table 3.3 is the CTE of fiber core. For optical fiber sensors, the generated thermal strains depend on both thermal-expansion and thermos-optical effect when temperature changes [44]. The thermal strains can be calculated:

$$\varepsilon = K \cdot (\phi + \xi)\Delta \mathrm{T} \tag{3.29}$$

where *Φ* and ζ represent the thermal-expansion and thermo-optical coefficients, respectively. According to literatures [45], [46], the *Φ* and ζ are selected as 0.55 x 10^{-6}/°C and 7 x 10^{-6}/°C.

Table 3.3 Properties of different components

Components	Fiber core	Coating	Adhesive	Matrix
Material	Silica	Polyimide	Epoxy	Stainless steel
Young’s modulus (GPa)	70	3	3	200
Shear modulus (GPa)	30	0.86	1	82
CTE (μm/m/℃)	0.55	40	40	23

The test system first tested the case with no mechanical loads at room temperature 25℃ (ΔT = 0), where the strain values were calibrated to zero, as shown in Figure 3.5 (a). Test results in each figure (see Figure 3.5a-d) were obtained by fixing the mechanical load at a constant level (0, 14.7N, 24.5N, 34.3N) and varies the thermal load. The theoretical results calculated using Eqs.(3.18) were compared with the experimental data. Figure 3.5 shows that the theoretical calculations of measured strains match well with experimental results. The measured strains are uniform near the center of bonded length and start to decrease when measured points are near the end of bonded length. As shown in Figure 3.5 (a), the maximum variations of measured strain along bonded length are 750 μ when ΔT = 65℃. The measured strain variations increase with the increment of thermal loads. When ΔT = 195℃, the measured strain variations along bonded length reach to 2,750 μ. When both mechanical and thermal loads applied to the measurement structure, the results are shown in Figure 3.5 (c)-(d). The theoretical calculations of measured strains are close to experimental results. When ΔT = 0℃ which means the measurement structure only subjects to mechanical loads, the measured strains are zero at the end of bonded length. When thermal loads are applied to measurement structure, the measured strains at the end of bonded length are not zero which depend on temperature variations.

Figure 3.6 presents the relative error of average measured strains along bonded length obtained from theoretical calculations and experimental results. It is shown the maximum relative error is 8.6%, and the average relative error from 15 groups of tests is 2.4%. The results demonstrated that strain transfer model can be applied to predict measured strains and calculate true strains on the surface of matrix.

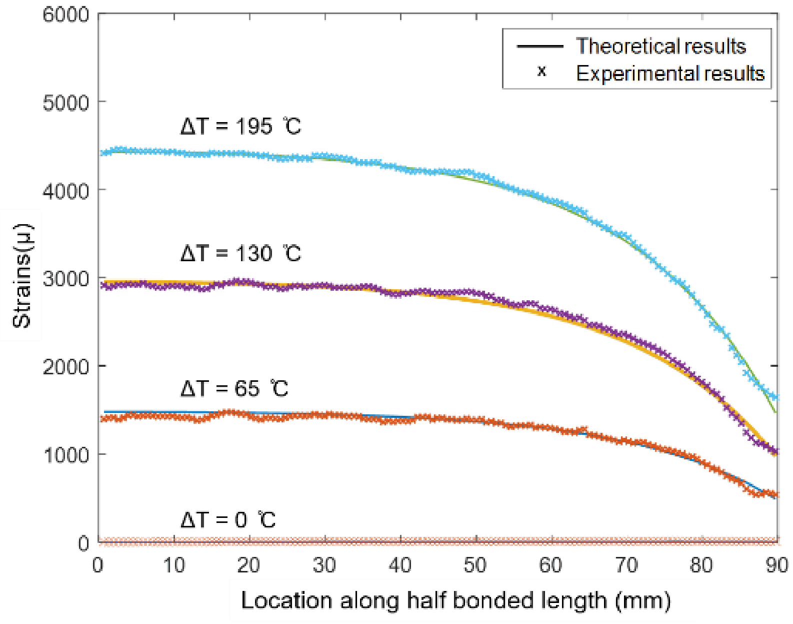

(a) Without weights, F = 0 N

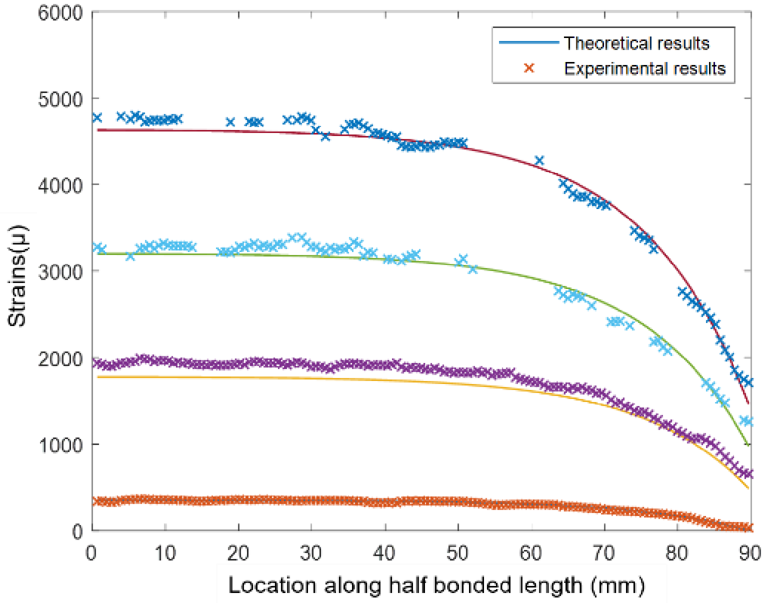

(b)1.5 kg weight, F = 14.7 N

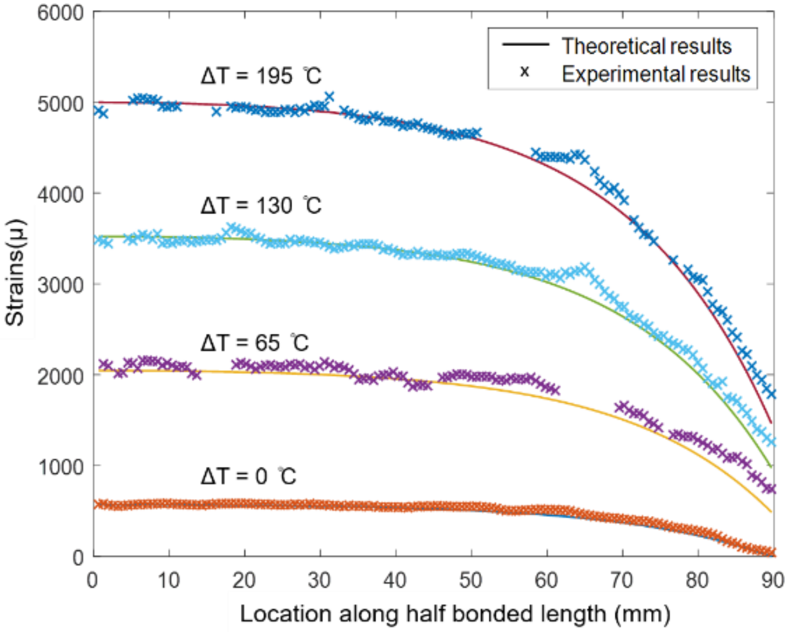

(c) 2.5 kg weight, F=24.5 N

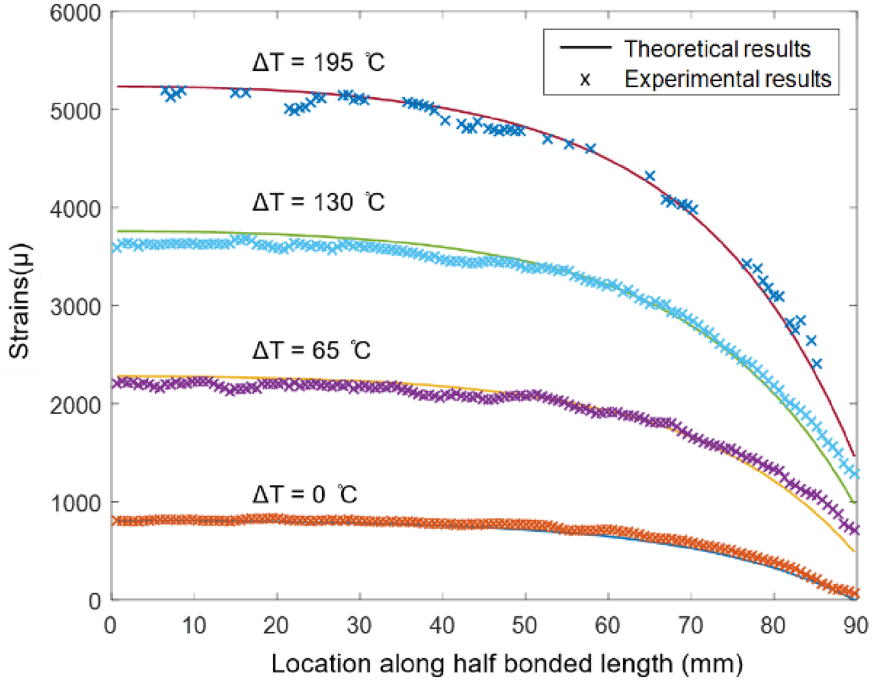

(d) 3.5 kg weight, F=34.3 N

Figure 3.5 Strain transfer ratio with different thermal loads

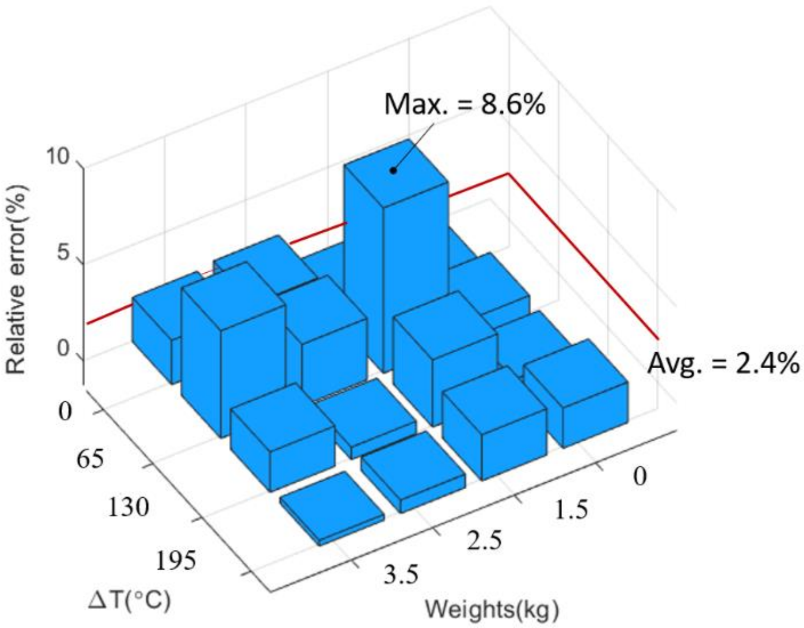

Figure 3.6 Average relative error between theoretical model and experimental results

3.4. Parameter Study

The analytical model shows that the strain transfer is influenced by bonding length, coefficient *k*, and CTE of materials. The coefficient *k* is further determined by mechanical and geometrical properties of measurement structure. In order to quantify how the strain transfer is co-determined by these parameters, a comparative study is conducted based on the analytical model.

3.4.1. Temperature *variation*

The strain transfer ratios for 180 mm bonded length measurement structure at different temperatures are shown in Figure 3.7 (a-b). The mechanical strains generated on the matrix are regarded as constants, which are 1000 μ in Figure 3.7 (a) and 10000 μ in Figure 3.7 (b). These two figures show that train transfer ratio depends on both temperature variations and mechanical loads. In Figure 3.7 (a), the strain transfer ratio decreases along fiber for all four cases with different temperature variations. The strain transfer ratio is zero at the end of bonded length when temperature variation is not considered. When thermal load is applied to measurement system, the strain transfer ratios are higher than no thermal loads applied structure at the same bonded position. The maximum variation of strain transfer ratio presents at the end of bonded length between $\Delta T= 0^\circ C$ and $\Delta T= 600^\circ C$, which is 0.32. For average strain transfer ratio along bonded length, the maximum variation among these four cases is 0.03.

When the mechanical load increased to generate 10000 μ strains on the matrix as shown in Figure 3.7 (b), strain generated in fiber mainly depends on mechanical load. The maximum variation of strain transfer ratio also presents at the end of bonded length between ΔT= 0˚C and ΔT= 600˚C, which is 0.19. The maximum variation of average strain transfer ratio among different ΔTs is 0.018. Both figures and calculated variations demonstrated that the strain transfer ratios are closer to each other under different ΔTs with larger mechanical load comparing with Figure 3.7 (a). The temperature influence on strain transfer ratio is not as obvious as that in Figure 3.7 (a).

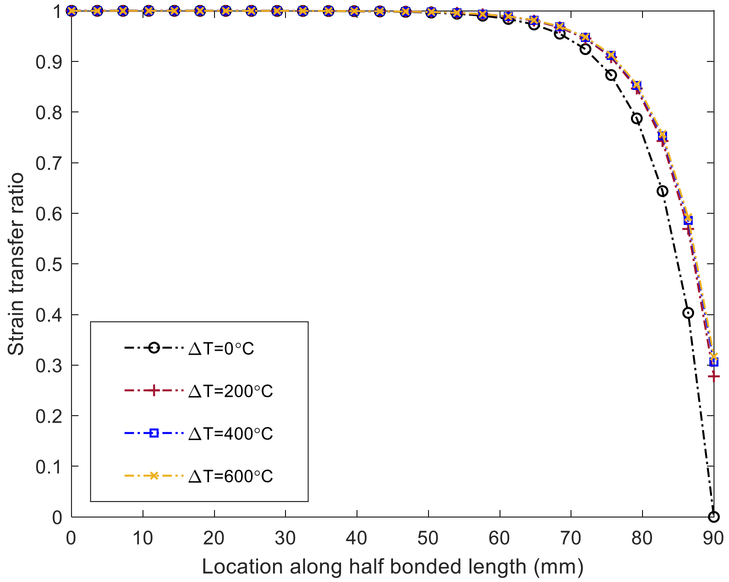

(a) ε_m= 1000 μ

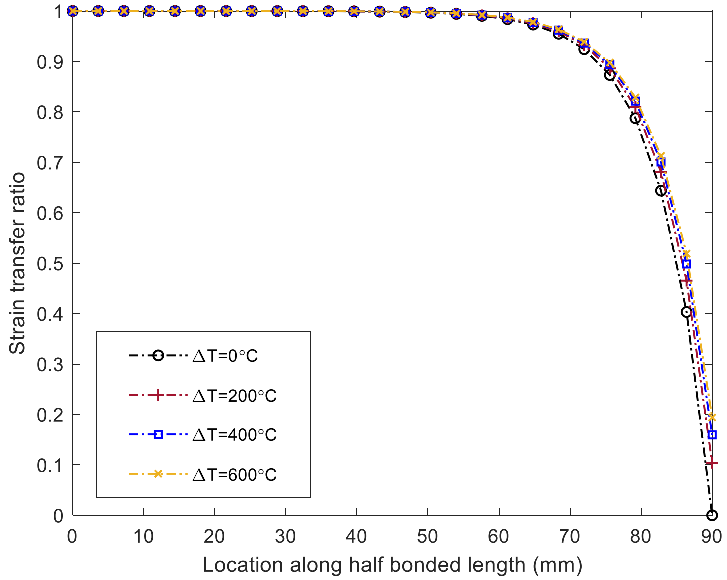

(b) εm= 10000 μ

Figure 3.7 Strain transfer ratio influenced by temperature variations with different mechanical strains

3.4.2. Geometry properties

Bonding length and adhesive thickness are two factors which are controllable during the sensor installation process. Figure 3.8 (a-b) show strain transfer characteristic with different bonded length optical fiber sensor when ΔT is 0℃ and

300℃. It is shown that even the transfer ratios are varying with temperature, the relationships between bonded length and transfer efficiency remains the same for all the tested cases: the increased bonding length will result in a strain transfer ratio approaching 1 at locations close to the center section. Figure 3.8 (c) shows the adhesive thickness influence on strain transfer with 180 mm bonded optical fiber sensor, where the strain transfer ratio is higher with reduced adhesive layer thickness at the same sensing point. The analysis of bonded length and adhesive thickness effect on strain transfer can provide a guide on determining sensors bonding scheme to obtain stable and effective measurements.

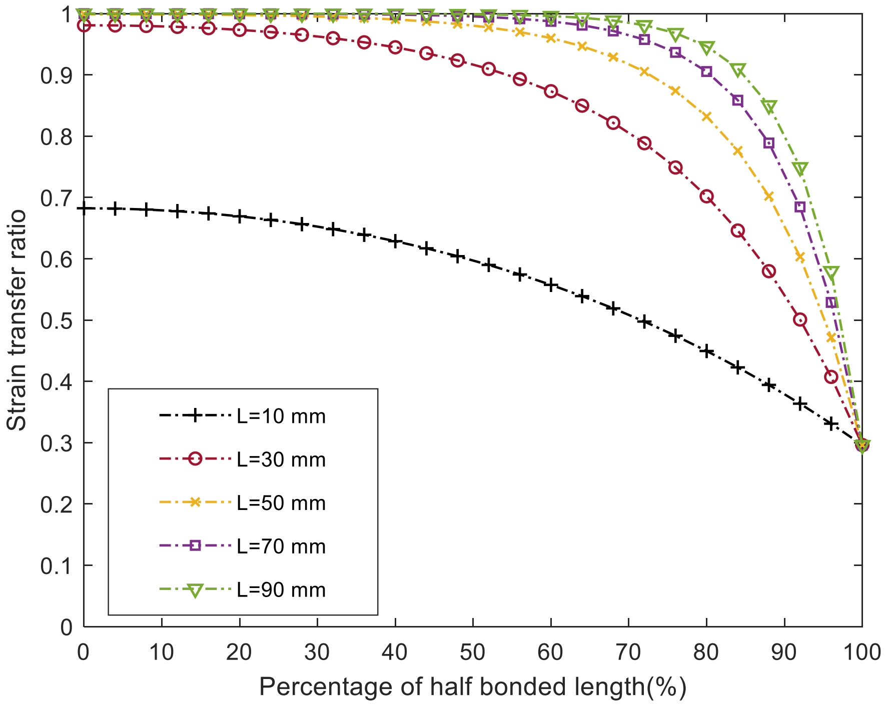

(a) Strain transfer ratios with different bonded length when ΔT =0℃, ε_m = 1000 μ

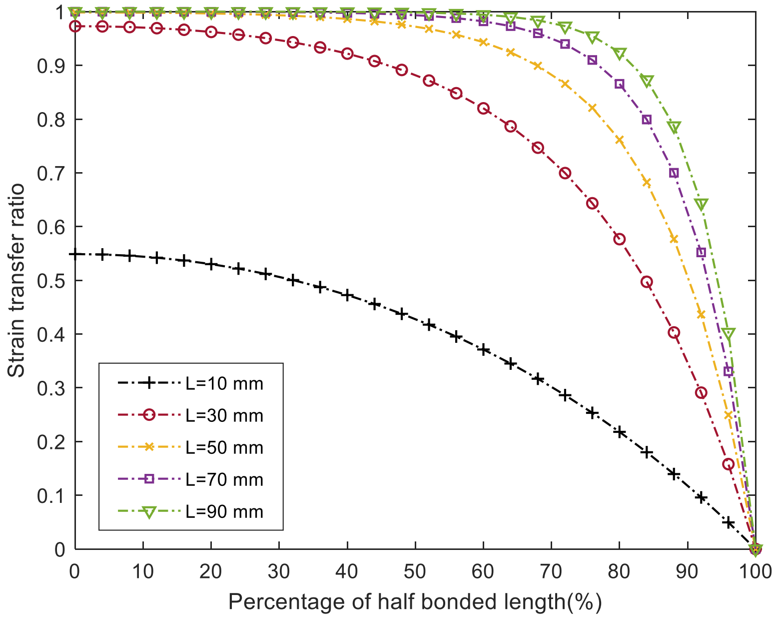

(b) Strain transfer ratio with different bonded length when ΔT = 300℃, ε_m = 1000 μ

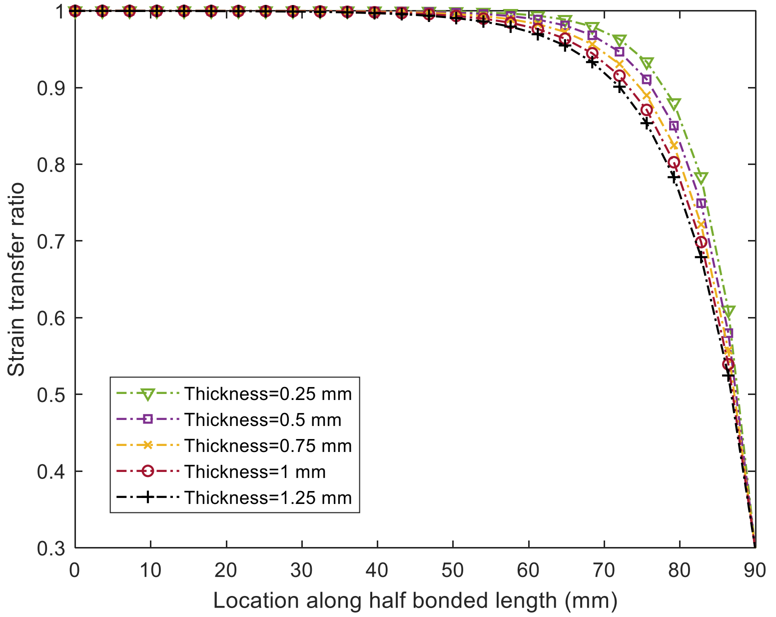

(c) Strain transfer ratios with different adhesive thickness when ΔT = 300℃, ε_m = 1000 μ

Figure 3.8 Geometrical properties influence on strain transfer ratio

3.4.3. Mechanical properties of adhesive

In practice, the Young's modulus of adhesives varies from 2 MPa to 2 GPa depending on adhesive materials and curing conditions [35], [37]. Figure 3.9 shows the Young's modulus of adhesive influence on strain transfer ratio. It is shown that strain transfer ratio is higher with higher Young's modulus for the same bonded point. The strain transfer ratio of Ea = 2000 MPa is regarded as reference to quantify adhesive influence on strain transfer. In Figure 3.9, there is a gap of strain transfer ratio curve when the Young's modulus is between 2 MPa and 2000 MPa. The relative error of average strain transfer ratio is 3% when Ea = 2000 MPa is reference. When the Young's modulus is higher than 20 MPa, the relative errors of average strain transfer ratios are less than 0.4%. It indicates that, in this case if high accuracy is required for strain measurements across the bonded section of fiber optic sensors, it is preferred to adopt adhesive with high Young's modulus larger than 20 MPa.

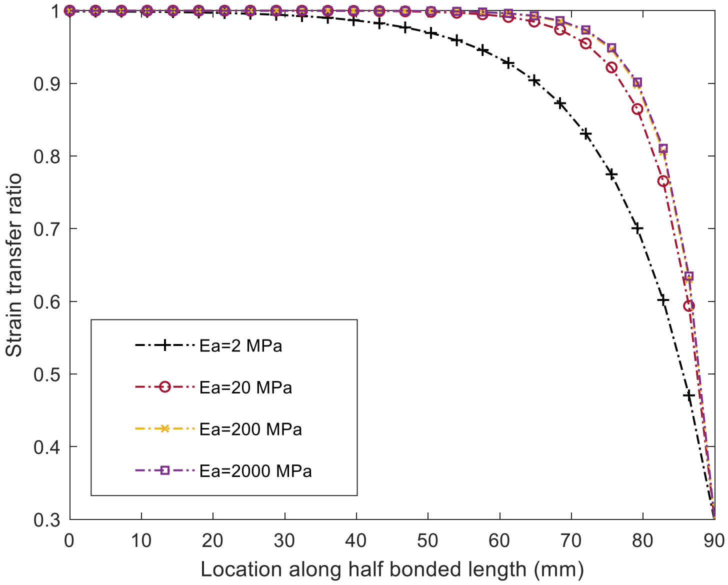

Figure 3.9 Young's modulus of adhesive influence on strain transfer ration when $\Delta T = 300℃$, $\varepsilon_m = 1000\ \mu$

3.5. Conclusion

In this paper, an analytical model of strain transfer characteristic for surface bonded optical fiber strain sensor is built. Both mechanical and thermal loads are considered in the analytical model to evaluate the strain transfer ratio variation along the bonded section of fiber optic sensors under different conditions. The analytical model is verified by experiments under different mechanical and thermal loads. The results show that the average relative difference between the analytical and experimental data is 2.4%. This model can be applied to calculate strain values on the matrix based on sensor measurements to improve measurement accuracy. Based on the analytical model, the parameters that affect strain transfer characteristic are further analyzed. It is shown that the strain transfer ratio is not constant for the packaged measurement structure but changes with the strain being measured when the temperature varies during the strain measurement. The calculation of effective sensing length can be applied to obtain strain measurements within tolerance when ambient temperature is not known during strain measurement. The parametric analysis presented in this paper is expected to provide a guideline on the installation of fiber sensors for high precision strain measurement.

MICROCRACK DETECTION IN PRINTED COMPACT HEAT EXCHANGER BY DISTRIBUTED OPTICAL FIBER STRAIN SENSOR

Xiaochen Hu and Zhaoyan Fan

Submitted to *Transaction on Instrumentation and Measurement*

Chapter 4. Microcrack detection in printed compact heat exchanger by distributed optical fiber strain sensor

Abstract - Compact heat exchangers (CHE) are regarded as candidate for next generation of heat exchanger applied in nuclear power plant. The structure health monitoring of CHE is important for this application. The geometric characteristics of CHEs make them have high heat transfer efficiency which include: 1). Dimensions of flow channels are at millimeter scale; 2) Hundreds of channels compact together with the interval at millimeter scale. However, these characteristics improved difficulties to detect cracks inside structure. This paper presents a method to detect cracks in one type of CHE, printed compact heat exchanger (PCHE). The feasibility of embedding distributed optical fiber strain sensors to detect cracks for PCHE was investigated. Three types of experiments: static load test, plastic deformation test and fracture test, were designed to validate the crack detection method. The experimental results match well with finite element analysis (FEA) results, showing that the stain variations induced by crack or during generating early crack can be detected. As a component affecting the crack detection accuracy, the fiber coating was discussed to quantify its correlation with the strain measurement results.

Key words: distributed optical fiber strain sensor, compact heat exchanger, crack detection, structure health monitoring, Rayleigh backscattering OFDR sensor

4.1. Introduction

Compact heat exchanger (CHE) is regarded as next generation of energy receiver in solar, nuclear power plant [47] since it has high heat transfer cycle efficiency with reliable mechanical characteristic under high pressure and high temperature. PCHE (printed compact heat exchanger) is a relatively new type of CHE. Hundreds of semi-circle channels manufactured by photo-chemically etched compose PCHE [48]. The radius of channels is 1 mm and the interval between channels is around 0.5 mm. The harsh operation condition of high temperature and high pressure and long years' service would increase possibility to generate failure or cracks in PCHE. When crack propagates through channels, different fluid in channels would mix and then generate chemical reactions which is harmful to heat transfer efficiency and system safety. Therefore, detecting cracks in PCHE at early stage when crack is at micro scale and then repairing the structure are necessary for applying PCHE in power plant.

Over the years, a lot of nondestructive testing (NDT) techniques have been developed including sensing acoustic [12] [49], magnetic [15], radiography [50] [14] and others signals. These NDT techniques have wide applications in structural health monitoring such as monitoring pipeline [12], masonry[51] and so on. However, they have some practical limitations in PCHE detection. For example, acoustic sensing is good to detect failures on the surface or subsurface of structure, but it is hard to detect internal failures. Moreover, the structural complexity of PCHE makes the acoustic signal hard to be analyzed. Radiography can detect internal failure of PCHE, but real-time monitoring is still a challenge. Distributed optical fiber (DOF) sensing is emerging as a powerful method for monitoring structural health. DOF strain sensors can achieve multiple pointes measurements employing scattering phenomena along the fiber. Moreover, comparing with other conventional strain sensors, optical fiber sensors are advanced in light weight, small size and immunity to electromagnetic interference. Categorizing by wavelength of scattering signals, two types of DOF strain sensors are commonly used in structure health monitoring by optical time-domain reflectometry (OTDA) or optical frequency-domain reflectometry (OFDA). Most of the previous research have investigated feasibility of structural failure detection by Brillouin optical time-domain analysis (BOTDA) strain sensors. Feng et al. investigated the BOTDA for damage assessment in structural members for civil structural monitoring. The bending test was conducted on I beam to analyze strain distribution when crack was on the beam [52]. Xu et al. studied the feasibility of the microcrack detection in pre-stressed concrete cylinder pipes through full scale experiments based on BOTDA. The selection of appropriate sensing cables and installation technique for accurate measurement were discussed [53]. Liu et al. proposed applying BOTDA to detect defects for civil structure by monitoring distributed dynamic strain. They applied wavelet transform to transform strain data from time domain to frequency domain and then achieved 40 με damage detection [54]. Babanajad et al. built a theoretical model for quantifying crack opening displacements based on measured dynamic strains by BOTDA. The experimental results indicated that it is possible to detect and quantify crack opening displacement of 200 μm and larger. Song et al. presented a strain processing approach, visual saliency-based image binarization, to achieve surface micro-crack detection by BOTDA. They found the minimum detectable crack opening displacement is 32 μm with 20 cm spatial resolution (SR) [55]. Literatures survey of defect detection by BOTDA reveals that BOTDA can be applied in structural health monitoring for different structures, such as steel beam, bridge, and large tubes. The BOTDA can achieve 30 km long-span structural detection [56]. However, the SR is around centimeter level which makes BOTDA hard to detect micro scale cracks in the structure.

Rayleigh backscattering distributed optical fiber strain sensors based on OFDA have been developed for structural health detection these years since the strain resolution is high to 1 με and the SR can be less than 1 mm [18]. The high strain and spatial resolution make microcrack detection possible. Berrocal et al. investigated the use of Rayleigh backscattering optical fiber sensor based on OFDR to detect crack in reinforced concrete beams. The beam bending tests with monotonic and cyclic loading were conducted to study strain distribution when crack presented on the beam. The presented early crack with 40 µm width can be detected with 0.65 mm SR [57]. Shan et al. applied Rayleigh optical fiber sensor to detect crack in composite winglet of a real aircraft. The test results showed that Rayleigh optical fiber sensor can identify existence and locations of damages successfully. The results obtained from fiber sensors matched well with that from strain gauges [58]. The Rayleigh backscattering fiber sensors are relatively new technique in structural health monitoring. Most of research investigated the feasibility of Rayleigh-based sensors in crack detection through bonding sensors on beams to detect surface cracks. For PCHE, cracks may present inside structure. The investigates of surface crack detections are hard to verify feasibility for internal cracks detection. Moreover, the complexity of PCHE structure would improve difficulty to detect cracks by Rayleigh based strain sensors.

The objective of the research described herein was to develop a distributed damage detection method for crack identify and locate for PCHE. Rayleigh based OFDR strain sensors was proposed to be applied to measure distributed strains along the structure. Experiments was designed and conducted to measure strain variations when crack presents in the PCHE structure during elastic deformation, plastic deformation and crack growth period. For improving accuracy of crack detection in PCHE, the influence of fiber coating on crack detection was learned by lab tests.

4.2. Theoretical basis for crack detection

The basic idea to detect cracks in the structure is that the strain distribution would be changed when crack presents inside structure. Figure 4.1 is an example to demonstrate this idea. When load F is applied on the beam without crack as shown in Figure 4.1 (a), the strain generated at position P1 can be calculated as below:

$$\varepsilon = \frac{\sigma}{E} = \frac{F}{w \cdot t \cdot E} \tag{4.1}$$

where σ is the generated stress under load *F*; *E* is the Young's modulus of beam; *w* is the width of beam, and *t* is the thickness of the beam. When crack presents in the beam under the same load, as shown in Figure 4.1 (b), the strain generated at position P1' where is the same location as P1 in Figure 4.1 (a) can be calculated as below:

$$\varepsilon' = \frac{\sigma'}{E} = \frac{F}{(w-d) \cdot t \cdot E} \tag{4.2}$$

where *d* is the length of crack. Therefore, the strain variation induced by crack can be obtained:

$$\Delta\varepsilon = \varepsilon - \varepsilon' = \frac{F}{t \cdot E} \cdot \left(\frac{1}{w} - \frac{1}{w-d} \right) \qquad (4.3)$$

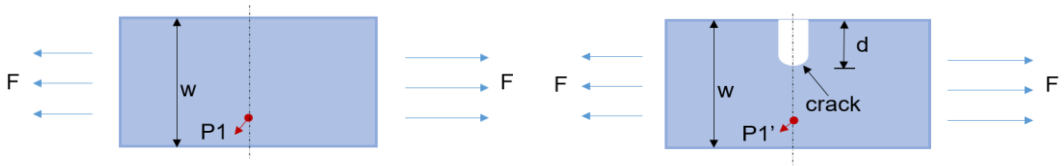

(a) Beam without crack

(b) Beam with crack

Figure 4.1 Demonstration of crack effect on strain generation

The above calculation demonstrated that strains would be changed when crack presents in the structure. In turn, changed strains can be applied to detect cracks in the structure. Considering the structural complexity of PCHE, finite element analysis (FEA) was applied to study strain distribution and strain variations induced by crack in PCHE. The sample section of PCHE was built in the FE model, as shown in Figure 4.2. PCHE is composed of multi-layer structures. Each layer contributes one row of channels. The modeled structure composed of 3 layers in total, each containing 5 semicircular channels. The channels were arranged in 3 x 5 matrix in the cross-section view of PCHE. The dimensions of the modeled structure are shown in the figure. The pressures for the cold and hot flows are set as 40 MPa and 16 MPa, respectively. The material of the structure was SS316 which is considered as a candidate material for the next generation of PCHE. The fiber sensors were proposed to measure strains in horizontal direction. Therefore, the simulation results and analysis only consider the horizontal strain distribution in the structure. The crack is set as a triangle with 0.3 mm width and 0.3 mm height. Figure 4.2 shows the case when crack presents in the middle of bottom layer. For calculating strain variations induced by crack in the structure, the structure without crack was also modeled. Strain variation along horizontal direction was obtained by comparing strain distribution of structure with crack and without crack. Figure 4.3 (a) shows the case when a crack is set in the middle of bottom layer. Figure 4.3 (b) shows strain distribution when no crack presents in the structure. The strain variations induced by crack can be calculated based on Figure 4.3 (a) and (b) which are shown in Figure 4.3 (c). The maximum strain variation (2000 με), as shown by the bright spot in Figure 4.3 (c), is present at the crack location. Distributed optical fiber sensors are proposed to be installed along horizontal direction in PCHE which demonstrated in Figure 4.3 (c). The sensors’ output can be estimated by the simulated strain values at the same locations. For the arrangement in Figure 4.3 (c), the associated outputs along sensors #1 and #2 for the structure with crack and without crack are shown in Figure 4.4 (a)-(b). Strain distributions obtained from both models with/without crack show that strain gradient in each channel is large. The strain gradient difference in each channel reached to 100 με which caused by characteristic of PCHE geometry. Figure 4.4 (a) shows that for Sensor #1, the strains from both models are close to each other. Since simulated crack presents at the bottom layer of channel which is far from Sensor #1, the crack effects on strain distribution is not clear. For the Sensor #2 shown in Figure 4.4 (b), strains from model with crack are higher than strains from model without crack, especially near crack position. Strain variations along sensors when crack presents in the structure were calculated and presented in Figure 4.4 (c). For Sensor #1, the magnitude of strain variation is less than 4 μ which caused by the far distance from crack to sensor location. The magnitude of strain variation along Sensor #2 is 10 μ at the center of sensor installation line where is close to crack location. Such a level of strain variation is measureable with high resolution commercial optical fiber strain sensors [18]. The sensor responses when crack presented in other channels were also learned. The channels in the model were numbered to clear express the crack location which is shown in Figure 4.3. Since the model is bilateral symmetric, the strain variations when crack presented in channel #1 to channel #9 were numerically learned as shown in Figure 4.5 (a)-(i). These figures demonstrated that strain variation distributions varied with crack positions. The maximum strain variation in each group presented near the crack position. When crack presented in the bottom layer of channels, significant changes of strains can be found at Sensor #2. In contrast, when crack presented at the top layer, strain variations along Sensor #1 are clear to be seen. Numerical results show that sensors are sensitive to the crack presences and positions. These results were regarded as a reference to analyze measured strains in the below sections.

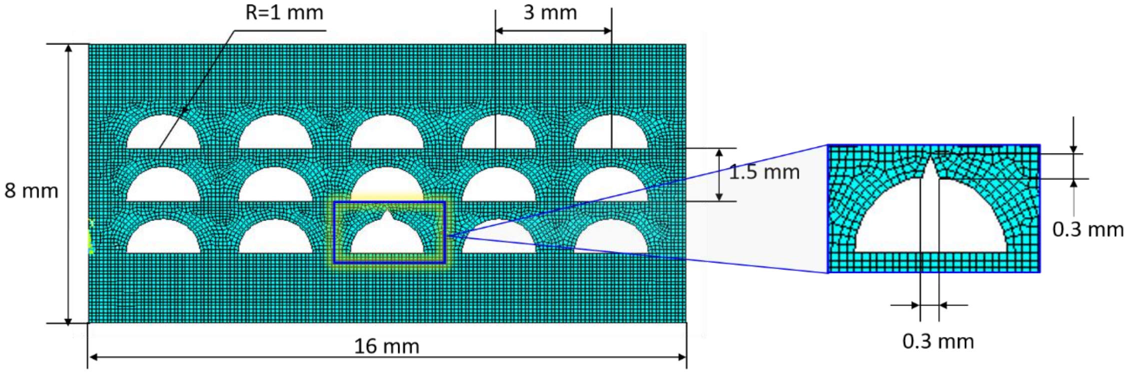

Figure 4.2 Dimensions of modeled section with crack

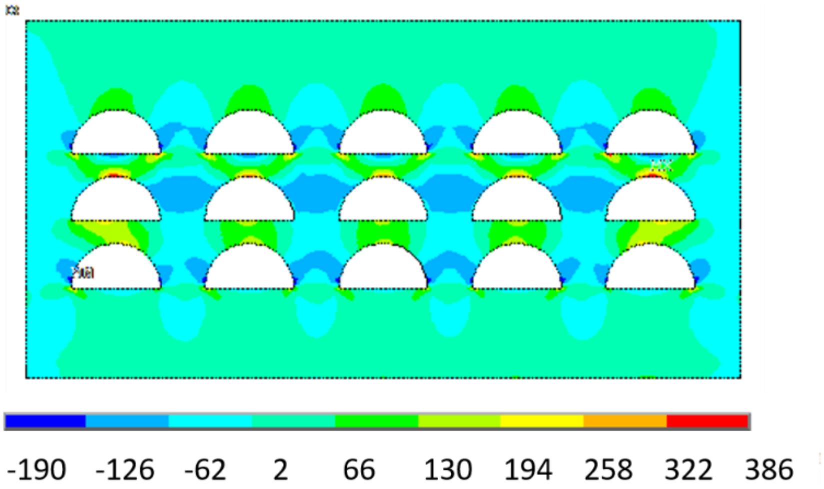

(a) with crack

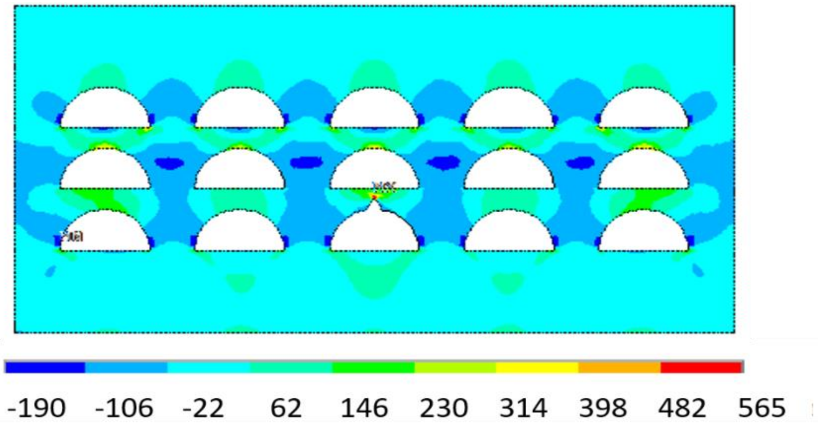

(b) without crack

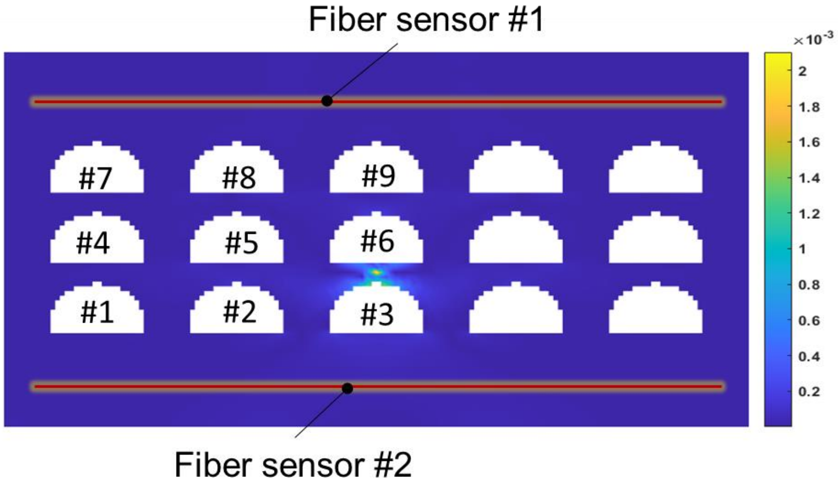

(c) Strain variation distribution induced by crack
Figure 4.3 Strain distribution for structure

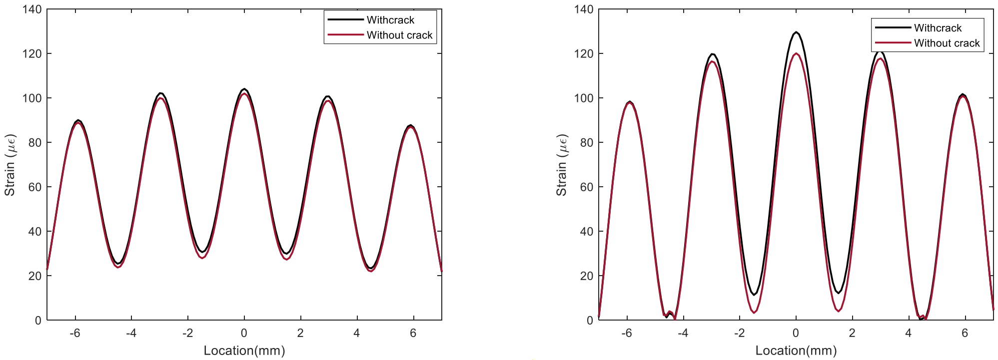

(a) Sensor #1 (b) Sensor #2

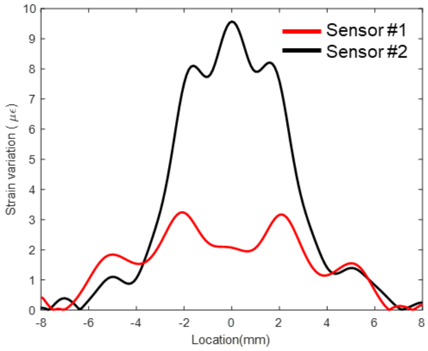

(c) Strain variations induced by crack
Figure 4.4 Strain distribution along fiber installation line

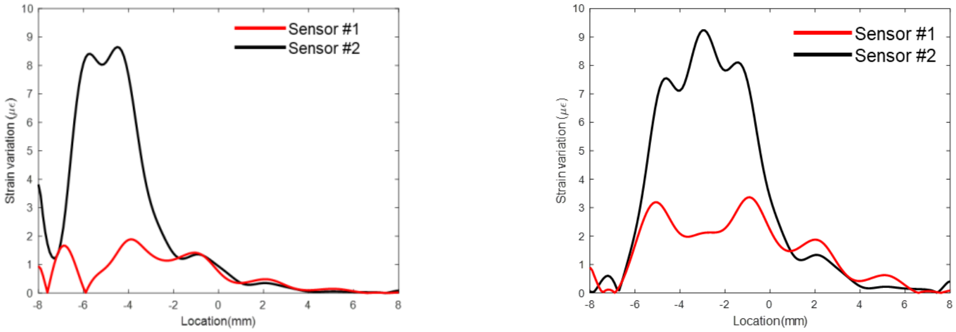

(a) Channel #1 (b) Channel #2

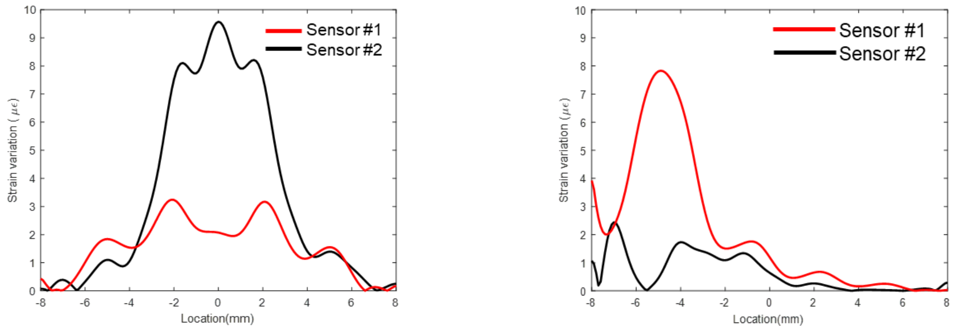

(c) Channel #3 (d) Channel #4

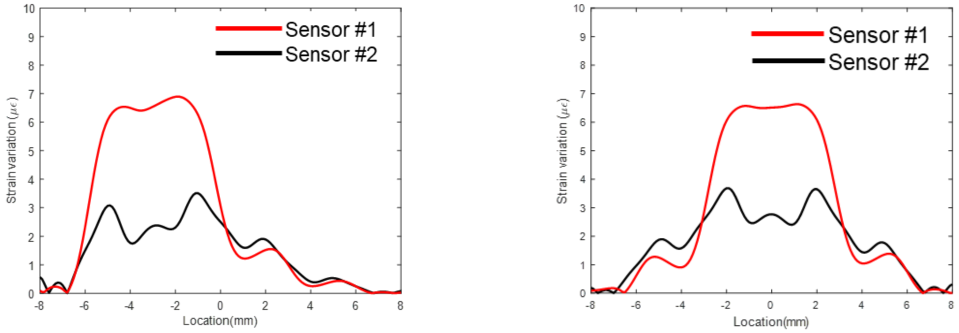

(e) Channel #5 (f) Channel #6

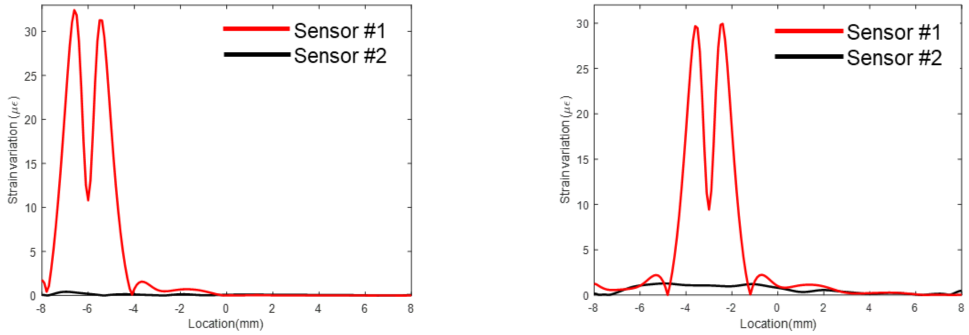

(g) Channel #7 (h) Channel #8

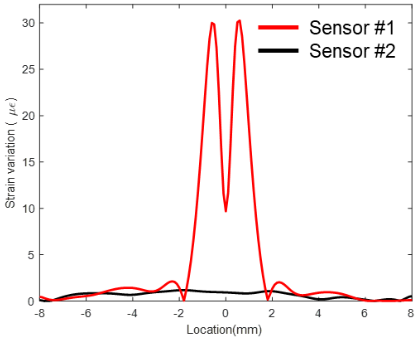

(i) Channel #9

Figure 4.5 Strain variations induced by crack along fiber sensors when crack presented in different channels from Channel #1 to Channel #9

Strain variations induced by crack for PCHE under different loading conditions were discussed. Figure 4.5 shows strain variation distribution when structure was under tension force. The crack was set at the middle of bottom layer which is the same as shown in Figure 4.2. The maximum strain variation is around 17 µ presenting at the location near to crack. Following the same analysis steps as discussed for the structure under pressure, strain variation distribution induced by crack can be estimated which is shown in Figure 4.6 (a). The outputs of Sensor #1 and Sensor #2 can be estimated by simulated results as shown in Figure 4.6 (b). Similar as discussion for sensor outputs under pressure, the effect of crack on strain outputs for Sensor #2 is clear since sensor is near to crack location. Comparing with calculated strain variations under pressure which presented in Figure 4.4 (c), the trends of strain variations along sensors are close to each other. Therefore, the effect of crack on sensor outputs for the structure under pressure and tension force are same. In this paper, the effect of crack on sensor outputs for the structure under tension force was experimentally studied. The experimental results can help to analyze the sensor outputs when the structure is under pressure conditions.

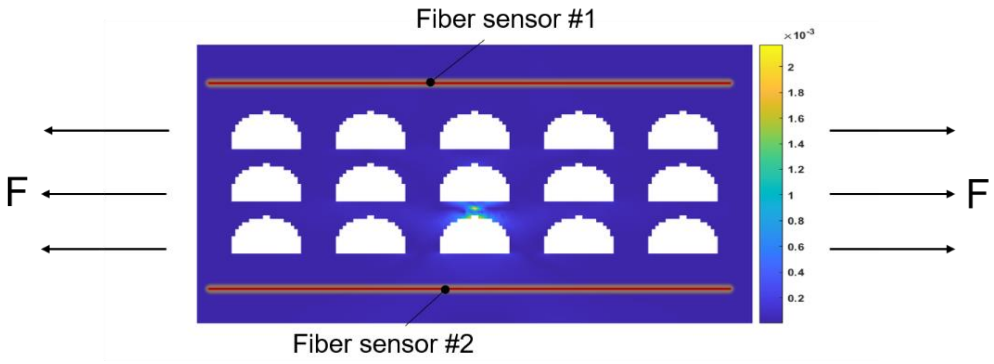

(a) strain variation distribution

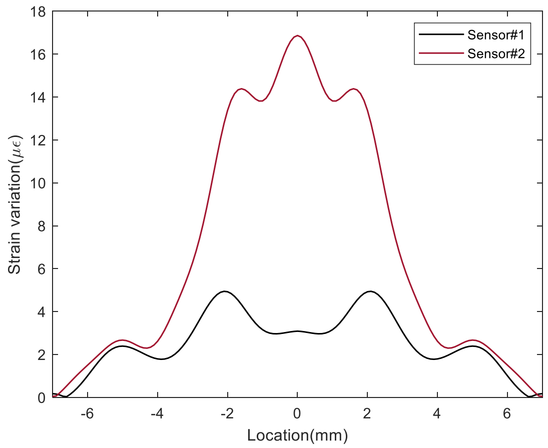

(b) Strain variation distribution along fiber installation line

Figure 4.6 Strain variation induced by crack under tension loading

4.3. Experimental methodology

4.3.1. Rayleigh based DOF sensing system

The Rayleigh-based DOF systems measure strains along fiber through getting signals after Rayleigh backscattering which is caused by inhomogeneity of the fiber medium [59]. For the Rayleigh backscattering sensing system, each backscattering interval can be regarded as a strain sensor. The Rayleigh backscattered light carries the information related to location and property of inhomogeneity. When fiber is stretched or compressed caused by mechanical load or thermal load, the location and property of inhomogeneity of backscattering points along fiber would be changed. This physical characteristic leads to the spectrum shift of scattered light. The shift in the spectrum can be presented as:

$$\frac{\Delta\lambda}{\lambda} = \frac{\Delta\upsilon}{\upsilon} = K_T T + K_\varepsilon \varepsilon \tag{4.1}$$

where T is temperature, ε is strain, λ is the mean optical wavelength, Δλ is the resonance wavelength, υ is the mean frequency, Δυ is the frequency shift, K_T and K_ε are the temperature and strain calibration constants.

Generally, the original or reference strain would be set as zero and temperature is regarded as a constant when applying Rayleigh backscattering light to measure strains. Therefore, the strain can be derived as:

$$\varepsilon = -\frac{\bar{\lambda}}{cK_\varepsilon}\Delta\upsilon = \bar{K}_\varepsilon \Delta\upsilon \tag{4.2}$$

In this paper, the Optical Distributed Sensor Interrogator (ODiSi B) from Luna technologies following the above principle was applied to investigate feasibility of crack detection in PCHE. The sensing performance is shown in Table 4.1. The high strain resolution and SR offer the availability to detect failures in the tiny and compact structure.

Table 4.1 Sensing performance of optical fiber sensor

SR	Sensing length	Strain resolution	Measurement range	System accuracy
1.28 mm	1-5 m	< 1 με	±10000 με	±25με

4.3.2. Test specimen

The experiences were conducted on universal machine (Instron 5960). The universal machine can apply tension force as large as 30 KN with 1 Hz acquisition rate. Dog-bone samples with PCHE geometry inside were manufactured to test strain distribution when applying loads to PCHE structure. The material of sample is SS316 which is regard as candidate material for PCHE in nuclear power plant. The design and dimension of samples are shown in Figure 4.7 (a). There are 3 x 5 channels in the sample. In order to learn crack influences on the sensor measurement, some of samples were manufactured with premade microcrack inside.

Optical fiber sensors were installed on the two sides of samples by epoxy with the distance of 1 mm to edge, being consistent with the installation scheme inside PCHE. The sensor installation process includes the following steps: (a) Sand the bonding surface of test samples with 400 grid and 200 grid sanding papers (2) Clean the sanding area with acetone (3) Bond fiber sensor on the cleaned surface of test sample by epoxy (4) Cure for 24 hours.

The test coupon with bonded sensor is shown in Figure 4.7 (b). In order to get stable and accuracy measurement, 50 mm – 55 mm fiber sensors are bonded on test coupons. The effective sensing length to study strain distribution in PCHE is the bonded fiber near to channel matrix. As shown in Figure 4.7 (a), there are 3 x 5 channels in the test coupon, and the area of channel matrix is calculated as 4 mm x 14 mm. Therefore, the effective sensing length for analysis is 14 mm. In the test, the measured strains at effective sensing length would be recorded and analyzed. The experimental setup is shown in Figure 4.8.

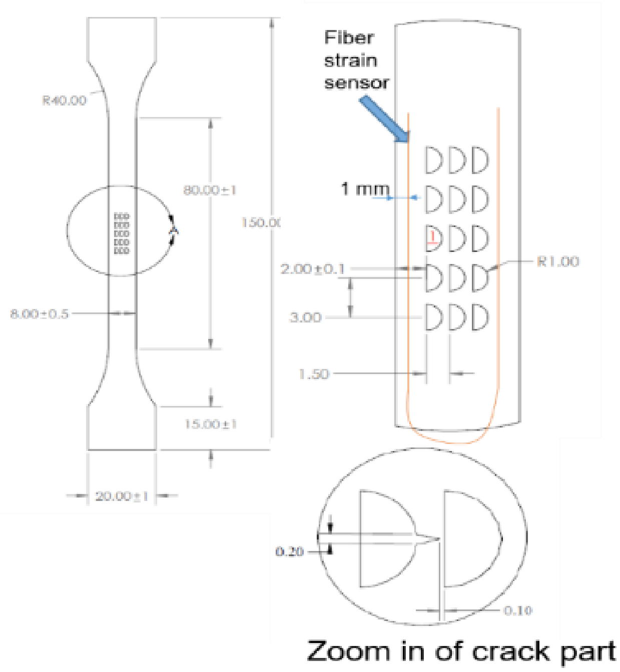

(a) Dimensions of multi-channel coupon and fiber bonding

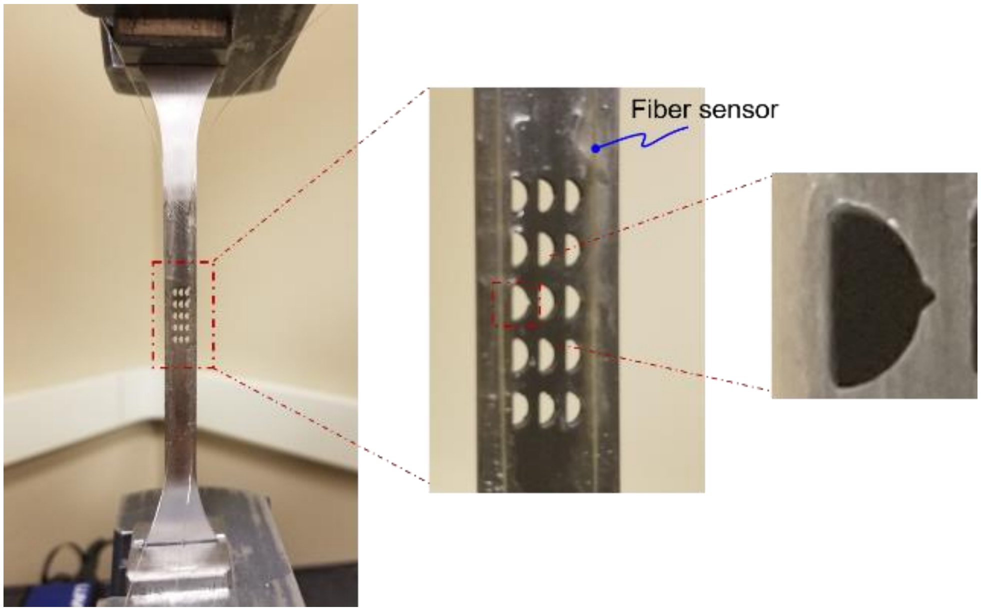

(b) Prototyped coupon for experimental test
Figure 4.7 Design and prototyping of test coupon

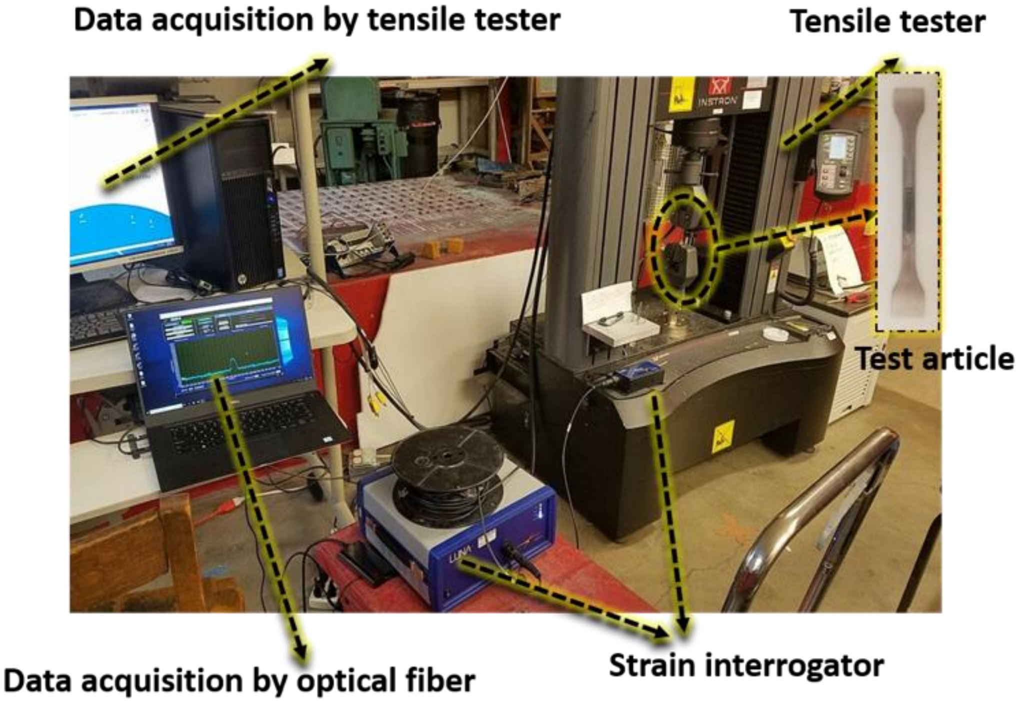

Figure 4.8 Experimental setup

4.3.3. Experimental program

For studying the strain variation induced by crack, static tests were conducted to test strain distributions of structures with and without crack inside under the same load. Moreover, since the material would pass through elastic and plastic deformation before getting fractured or failure, the plastic deformation of PCHE can be regarded as the early stage to generate microcrack. In this paper, the strain distribution of PCHE during plastic deformation was studied for early microcrack detection which can provide timely maintenance information to avoid serious damage. After plastic deformation, material would start to fracture and crack would start to grow. The sensor responses when crack starts to grow was also studied. Overall, loading tests for the PCHE structure on the three stages of material deformation (elastic, plastic and fracture) were conducted to study sensor responses when crack presents and grows in the PCHE.

Fiber coating bonded between structure and fiber core during sensing would influence strain measurements. Both strain transfer characteristic and slip between fiber coating and fiber core effect the accuracy of measurements[29][60]. Fiber coating can protect fiber sensors when sharp deformation generated. However, it will average and decrease the magnitude of measured strains. In this chapter, fiber sensors with and without coating were applied to measure strain distribution of PCHE under same load. The influence of fiber coating on strain measurement was discussed based on measured data. The designs for each experimental procedure are introduced as following:

(1) Static test

In static tests, two coupons with and without premade crack inside were tested under the same load. The coupon with premade crack was shown in Figure 4.7 (a). A 5-m fiber sensor was bonded on the two sides of both test coupons. The same and stable forces were applied on both coupons to get measured strains from fiber sensors. Take 750 N tension force applied on coupons as an example, Figure 4.9 shows the loading procedure during test. The extension was increased with 0.0018 mm/s until the applied force reach to 750 N. The system held 60 s to get stable strains. 3 groups of test for both coupons were conducted with 750 N, 1000N and 1250 N applied tension force. The strain distributions of these two coupons were compared to learn strain variation induced by crack.

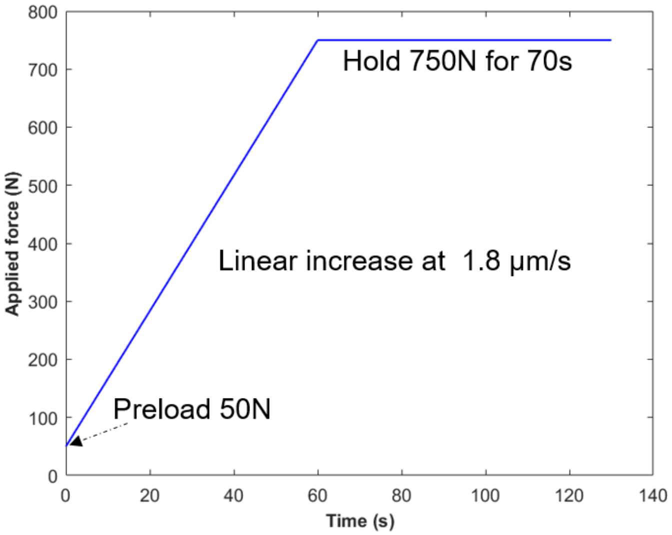

Figure 4.9 Universal machine setting for static test

(2) Plastic stage test

In the plastic test, the coupon with a premade crack (as shown in Figure 4.7 (a)) was tested under cyclic tension force. Figure 4.10 shows an example of test procedure. The cyclic force was set between 1000 N and 1500 N to generate plastic deformation for test coupon. 6 cycles were applied for each test. The applied force held at 1000 N after each cycle to record measured strains at the same load during plastic deformation. In the plastic stage test, 4 groups of tests were conducted with different applied tension force: 500N~1000N, 1000N~1500N, 1500N~2000N and 2000N~2500N.

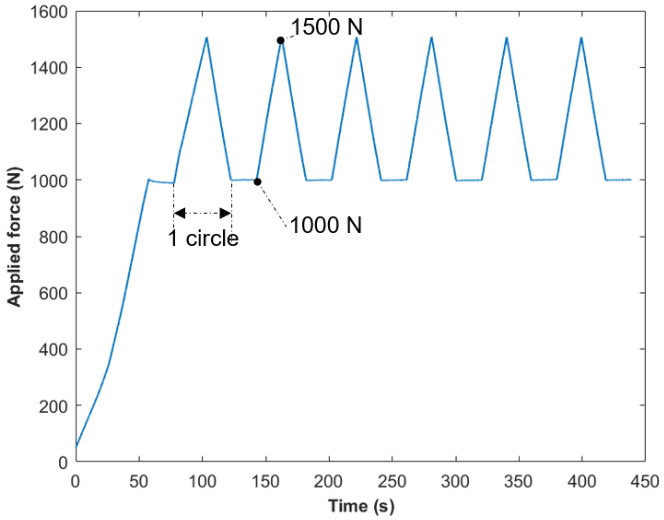

Figure 4.10 Universal machine setting for cyclic test

(3) Fracture stage test

In order to study sensor responses during crack growth for PCHE geometry, the coupon with a premade crack inside was tested under increasing tension force which enabled crack growth. The tension force kept increasing with extension rate 0.002 mm/s. The tension force would hold 30 s during each 500 N increment from 1000 N until the coupon fractured. The measured strains at each holding duration would be recorded and analyzed.

(4) Coating material analysis

For studying fiber coating influence on sensor measurement, fiber sensors with and without coating were bonded on the two sides of test coupon separately. The bonding scheme is shown in Figure 4.11. The acrylate coating fiber was bonded on the side A of test sample, and the fiber sensor without coating was bonded on the side B with the same location of side A. A stable tension force was applied to the test coupon which is the same as in static test. 2 groups of tests were conducted with different tension force:

1000N and 1500 N. The strain distribution measured by these two sensors were recorded at the same time.

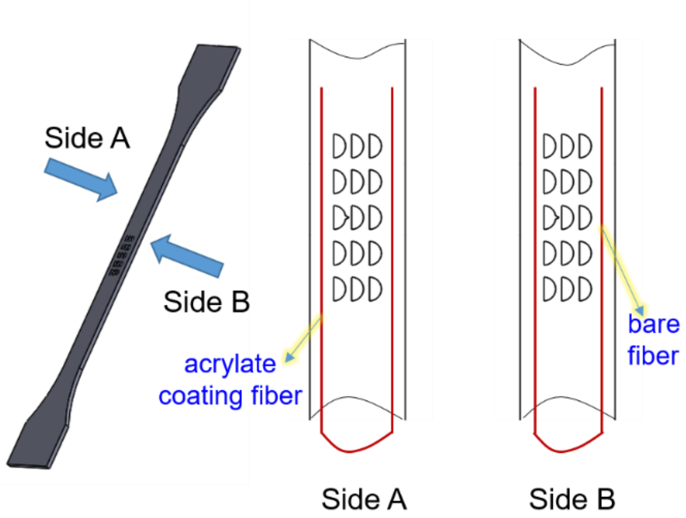

Figure 4.11 Bonding scheme for comparing measurements with differnet fiber coating

4.4. Results and Discussions

4.4.1. Static test

The measured strains for two test coupons under the same load were compared. As introduced in the Section 4.3.2, there are 50 mm fiber sensor bonded on each side of test coupons. The effective sensing length to study strain variations induced by crack for PCHE geometry is the part near to channel matrix. The strain variations at the effective sensing length were calculated based on measured strains. Following the test direction in Section 4.3.2, the fiber sensor bonded at the left side of test coupon is named as left sensor which is near to premade crack. The sensor bonded at the right side is named as right sensor. Figure 4.12 shows the calculated strain variations for left and right sensors when crack presented in the test coupon. The numerical results discussed in Section 4. 2 was added in the figure to compare with experimental results.

Error bar at each sensing point calculated from 100 times repeat tests was also added in the figure. Figure 4.12 shows that the trends of strain variations obtained from numerical results and experimental results are close to each other. When fiber sensor was bonded near crack position as left sensor in this test, the strain variations was clear and can be detection. When fiber sensor was bonded two columns away to crack position as right sensor in this test, the strain variations are not as clear as left one. This result can provide an overall evaluation of measured strains when crack presents in the structure. Moreover, the result can help layout fiber sensors in the structure to detect cracks. These tests results are consistent with the simulation data and demonstrated that the presence of crack can be detected by fiber strain sensors.

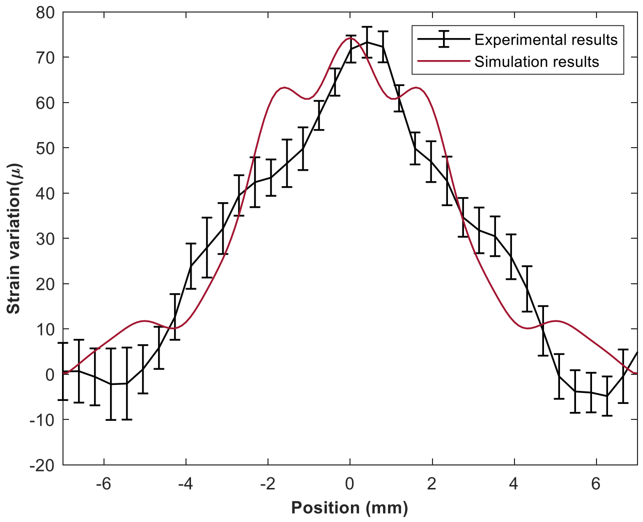

(a) left sensor

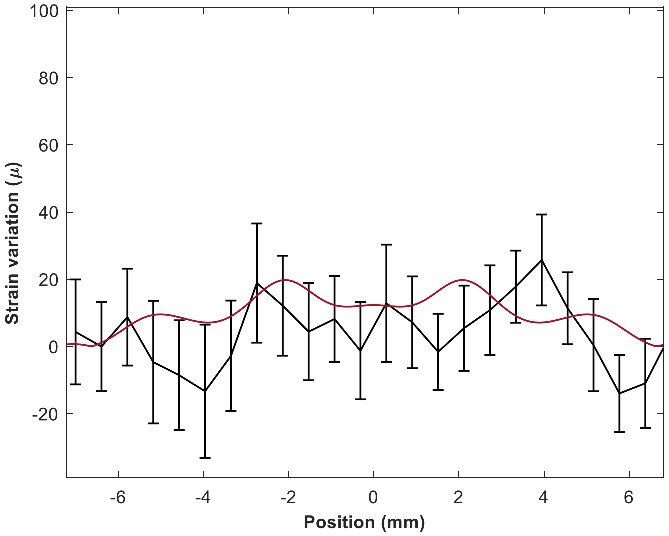

(b) right sensor

Figure 4.12 Measured strains for coupons with and without crack under 1000 N tension force

4.4.2. Plastic stage test

The measured strains in plastic deformation test with 1500N ~ 2000N tension cycle are shown in Figure 4.13. There are 6 tension cycles in the test. Figure 4.13 shows that strains increased with the increment of cycles for both sensors. The maximum strain is at the middle of bonding length for each sensor. For the left sensor, the maximum strain is higher than that at right sensor at each tension cycle. In order to analyze plastic deformation influence on strain distribution, the first cycle was regarded as strain distribution reference. The strain variations for cycles 2-6 with reference strain were calculated as shown in Figure 4.14. Figure 4.14 (a) shows that for the left sensor, the strain variations increase with cycles and the maximum increment presents at the middle part of channel position. The reason of measured strains kept increasing during cyclic tension is that test coupon can't recover after plastic deformation. The similar results also present at right sensor which is shown in Figure 4.14 (b). However, the magnitude of increment at right sensor is not as high as that at left sensor. The maximum strain variations after plastic deformation at each cycle were extracted from cyclic tension tests with different loading level which is shown in Figure 4.15. When the cyclic tension forces are under 1500 N, test coupons are under elastic deformation where deformations can restore after each cycle. The maximum strain variations at each cycle is less than 20 με. Cracks are hard to grow in the structure under these conditions. When the cyclic tension forces are above 1500 N, maximum strain variations start to increase with cycles which demonstrated the generation of plastic deformation. Cracks would start to grow with continuous plastic deformation. These results demonstrate fiber sensors can be applied to detect early failure and crack at plastic deformation phase in the compact heat exchanger.

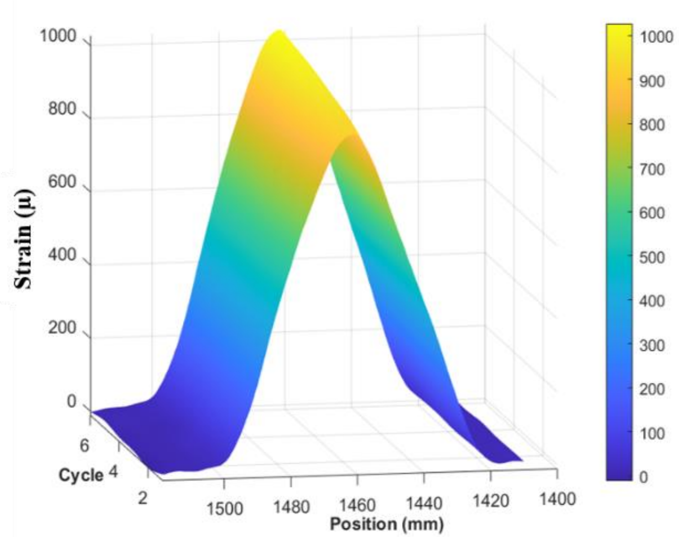

(a) left sensor

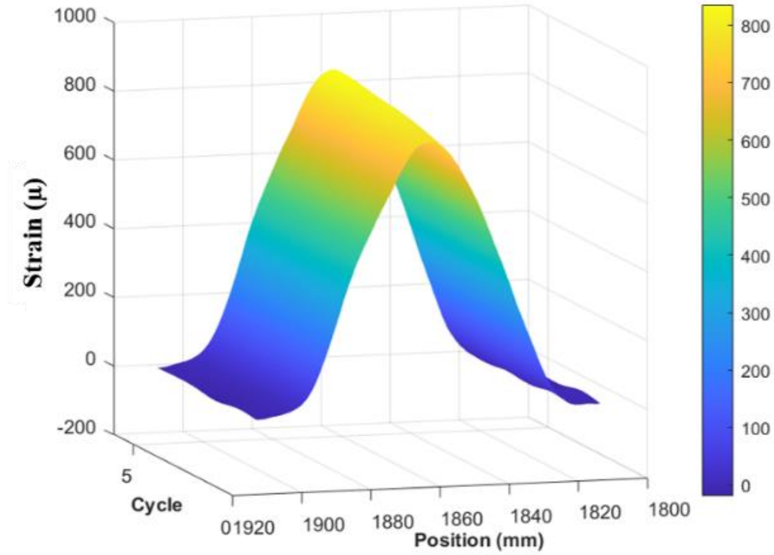

(b) right sensor

Figure 4.13 Measured strains during plastic deformation

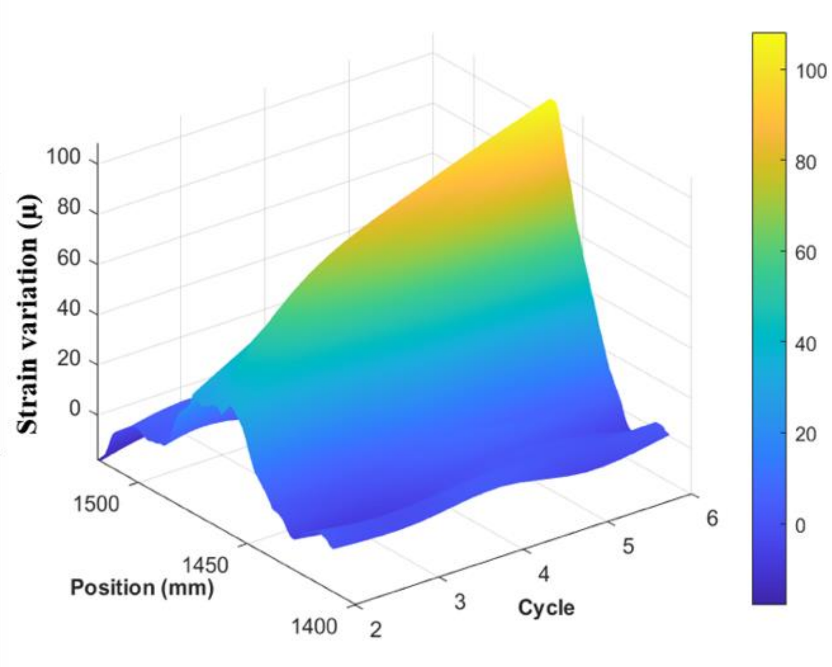

(a) left sensor

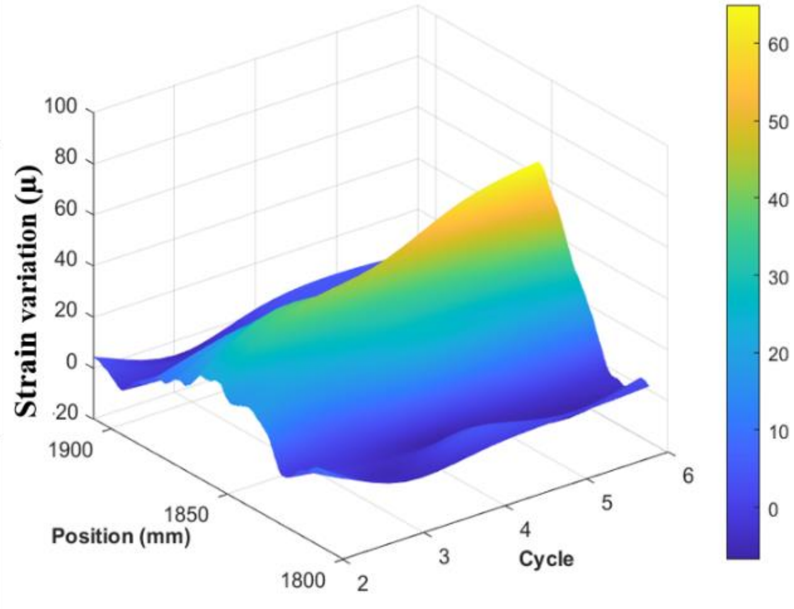

(b) right sensor

Figure 4.14 Strain variations during plastic deformation test

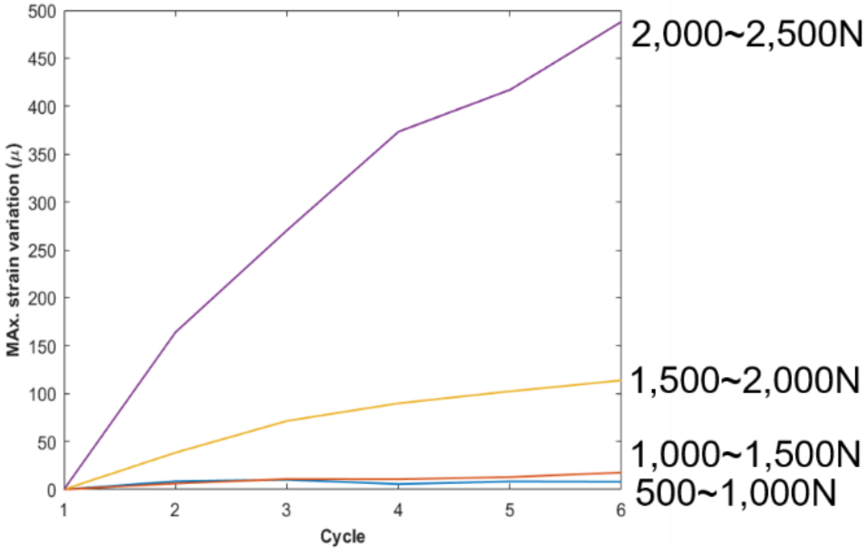

(a) left sensor

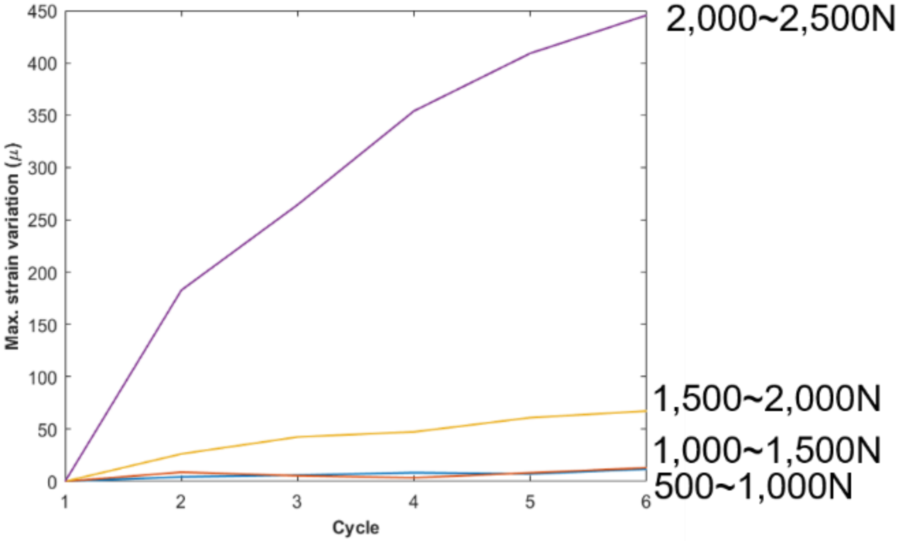

(b) right sensor

Figure 4.15 Maximum strain variations with different tension cycles

4.4.3. Fracture stage test

The measured strains were recorded under different applied force during fracture test as shown in Figure 4.16. As tension force increased, the test coupon experienced elastic deformation, plastic deformation and finally break. Strains along fiber sensors keeps increasing with tension force. The maximum stain variation is around 300 με from 1000 N to 1500 N, and 1200 με from 1500 N to 2000 N at left sensor. The disproportionate increment of strains with tension force shows plastic deformation during test. When the tension force reaches to 2500 N, measurement data start to loss around the middle of channel matrix for both two sensors. The strains anomalies are also shown in other experiments [61][62] when test material generates plastic deformation. The reason to cause strains anomalies may come from two points: 1) strains around the middle of channel matrix are too high which are beyond the measurement range of system (10000 με); 2) the strain gradient is too high which caused Fresnel's reflection. The Fresnel's reflection means when the energy of backscattering light is very higher than the reference signal at the beginning of the test, a 'blind' zone would be generated on the area near the high-energy point. In practice, operators can apply this phenomenon during structural monitoring to check cracks in the PCHE.

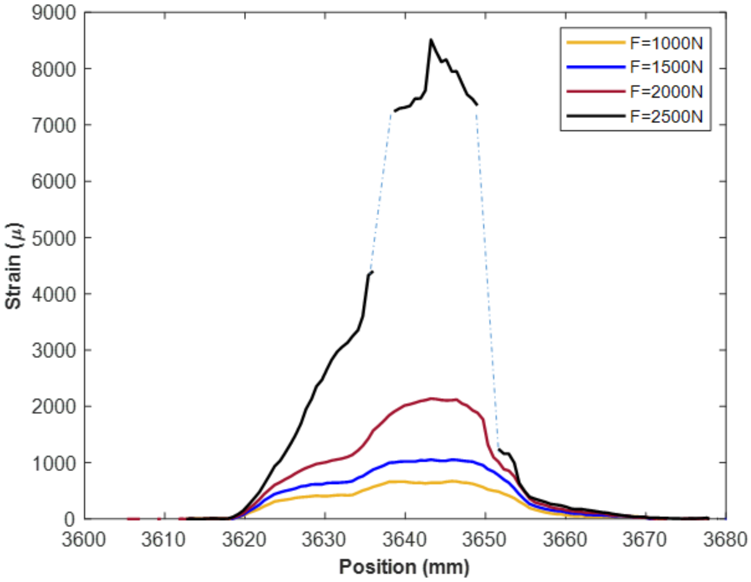

(a) left sensor

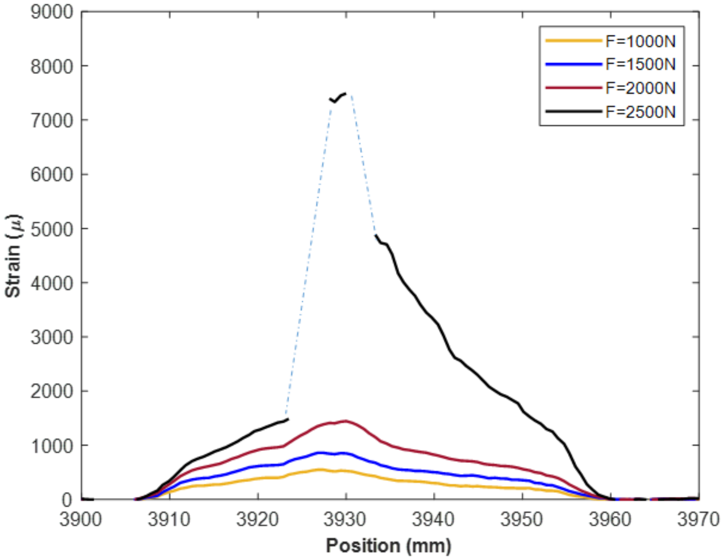

(b) right sensor
Figure 4.16 Sensor measurements for crack growth test

4.4.4. Coating material comparisons

Figure 4.17 shows measured strains under 1000 N tension force by optical fiber sensors with and without coating. Strain distribution from FEA is regarded as a reference to compare measured strains by these two sensors. It is shown in Figure 4.17 that the overall measured strains by bare fiber are higher than simulation results. The strain differences between them at each sensing position is around 50 με. The trend of strain distribution measured by bare fiber is much close to FEA results. For the fiber sensor with acrylate coating, there is a big difference of measured strains with FEA results. The average strain measured by acrylate coating fiber is around 400 με, but the average strain from FEA results is above 600 με. Moreover, it is hard to see similar trend of strain distributions between acrylate coating fiber and FEA results. Table 4.2 presents quantification evaluation of sensing performance under 1000 N and 1500 N tension force. For the bare fiber, the correlations between measured strains and FEA results are above 0.65 under different tension loads. The correlations between measured strains by coated fiber and FEA results are less than 0.1 which are much lower than that from bare fiber. Moreover, the average differences between measured strains by coated fiber and FEA results are higher than that by bare fibers. Both correlations and differences show that sensing performances of these two sensors are quite different. The reason to cause these differences is strain transfer mechanism, how strains transfer from test coupon surface to fiber core. For acrylate coated fiber, there are four layers to transfer strains from test coupon: matrix, adhesive, coating and fiber core. For bare coating, only three layers to transfer strains: matrix, adhesive and fiber core. The strain loss would be decreased by decreasing transfer layer. That is one reason to make the overall strains measured by bare fiber higher than that by coated fiber. Another reason comes from slippery between coating layer and fiber core. The slippery makes strains hard to totally transfer from coating to fiber core. The similar experimental results and conclusions are obtained by other scholars[29][60]. High precision fibers, like bare fiber, are good to get local strains but would be easy to be damaged by cracks in the test since it is sensitivity to structural change. Other fibers with a not very high precision is durable, especially when crack width is large and strains are high in the structure. For PCHE structure, channels are at millimeter level and cracks are at micro scale which cause strain variations induced by crack are not very high. The high precision and sensitivity fiber sensor is more suitable for PCHE detection.

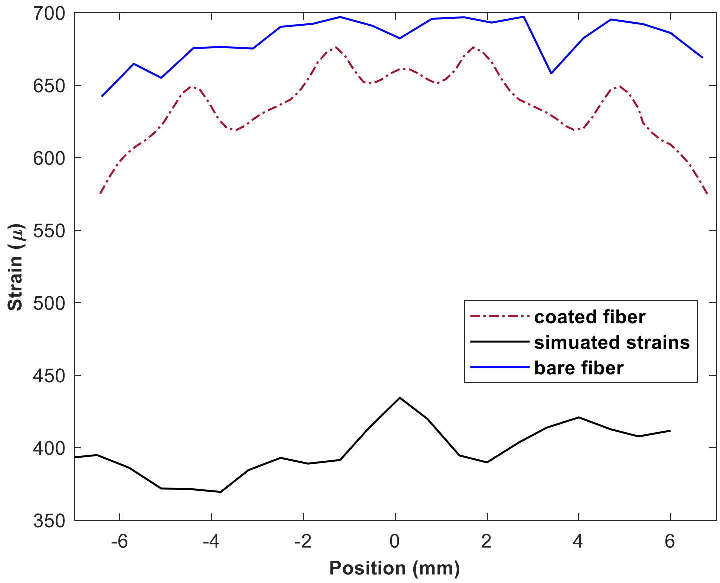

Figure 4.17 Comparison measurements by different coating fiber sensors with FEA results

Table 4.2 Comparison of measurement performance with simulations

	Load	Bare fiber	Coated fiber
Correlation	1000N	0.65	0.09
	1500 N	0.66	0.08
Difference	1000 N	41µ	241 µ
	1500 N	40µ	394 µ

4.5. Conclusion

In this paper, the feasibility of applying Rayleigh-based OFDR strain sensors to detect cracks in PCHE was investigated. Lab tests were conducted to analyze strain distribution of test coupons, including: static test, plastic deformation test and fracture test on universal machine. Static test shows that strain distribution would be changed when crack presents in the structure. The strain variations induced by cracks can be detected by fiber sensors. The plastic deformation test shows that strain variations increased during plastic deformation which can provide reference for early crack detection. The fracture test shows that when crack starts to propagate in the structure, the measurement data start to loss around crack position. The measurements at other positions along fiber still work well. The strain anomalies can be regarded as a signal of crack growth in PCHE. Moreover, the influence of fiber coating on strain measurement was learned. The measured strains by bare fiber are closer to FEA results than that by coated fiber sensors.

A New Approach to Monitor Material Composition for Additive Manufacturing Based on Temperature Contour Measurement

Xiaochen Hu, Dongqing Yan and Zhaoyan Fan

Submitted to Journal of Manufacturing Science and Engineering

Chapter 5. In-situ Monitoring of Material Composition for Additive Manufacturing

Abstract

Binary material and functional graded material (FGM) additive manufacturing (AM) is an approach received increasing attention in the recent years, due to its capability of tailoring product properties to achieve position-determined functions of products. Material composition is a significant factor that effects properties of AM products, especially for binary material and FGM printing. In-situ monitoring the material composition and providing feedback for the quality control has thus become one of the key research issue for AM. This paper proposed an in-situ sensing method to identify material composition by monitoring the temperature contour surrounding the melting pool in AM. The relationship between material composition and dimensions of the temperature contour on the powder bed was analytically modeled based on Fourier's law of thermal conduction. To validate the model, raw thermal images of the melting pools of Copper-Inconel 625 alloy were captured by an IR camera during Laser Powder Bed Fusion. The thermal images were processed through image segmentation to extract features such as the length and width of the contours, which showed consistent trend with the theoretical results. The extracted features and actual weight percentage of copper in the alloy were further used to train an Artificial Neuron Network (ANN) model. The results showed that the accuracy of 94% was achieved when using the trained ANN model to estimate the composition of alloy from the thermal image data.

5.1. Introduction

Additive manufacturing (AM) has been widely studied for various applications in the recent decades due to its advantages in fast prototyping and complex structure manufacturing. Depending on material feeding methods, the AM technologies can be categorized as powder bed fusion (PBF) and direct energy deposition (DED) [63]. Conventional AM prints material with fixed composition, such as steel, titanium, nickel, aluminum, cooper magnesium, cobalt-chrome, tungsten and gold [64], to achieve consistent material properties across the printed parts. In the recent years, new techniques have been developed to process different component metals and melt them to form alloy during the printing process. By adjusting the feed rate of the component metals, it enabled customizing the binary and ternary alloy and accordingly tailoring the mechanical properties, corrosion resistance, and antibacterial properties [64]–[70]. The new capability also included producing functional graded material (FGM), where the material composition was adjusted during printing a single part, to develop the required properties at designated locations for multifunctional application.

Prior studies have tested process-structure-property relationship of FGM with Ti-Cr [65], Ti-Al [66], Ti-W [67], Fe-Ni [69] and Cu-Ni [68] alloy system, and shown the microstructure and mechanical properties of the alloys are sensitive to the material composition. Small variations in the composition control may lead to property inconsistency or even defects in the printed structure. However, due to the evaporation rate of different metals at the heating temperature, inhomogeneous material distribution, and inconsistent mixture of wires and powders, the composition is yet accurately controlled in the present AM systems [70]. Karnati et al. [71] premixed Cu and Ni powder for PBF process and observed a 4% error between the designed and realistic composition. Cui et al. [72] designed new alloy, AlCoCrFeNi, with 20% of Al, while the actual weight percentage of Al is less than 15%. Li et al. [69] studied Fe-Cr-Ni FGMs and found a maximum error of 15% in the weight percentage Cr between the experimental and theoretical results. Given the inconsistency of material composition in binary material and FGM printing, the in-situ monitoring of compositions has become a critical issue for the precise control of alloy printing in additive manufacturing. Although some of the material composition detection methods, such as X-Ray Fluorescence (XRF) [73] and Electro-Backscatter Diffraction (EBSD) [74], is capable of providing accurate readings post-process, they are sensitive to the ambient air flow and thus require either vacuum environment or contact the detector with the specimen to minimize the disturbances. Such requirements made it hard to apply these methods to measure composition in-situ during AM.

Most of the research in in-situ composition monitoring focused on the spectrometers in the recent literatures [75]–[78]. Spectrometers measure the emission spectrum of plasma above the melt pool and estimate the material type and percentage according to the wavelength of emission spectrum. Ma [75] applied opto-ultrasonic dual detection method to detect the percentage of Ti in the ER2319 aluminum alloy printed in wire arc additive manufacturing. Huang [76] compared between the spectrums of Al alloy 6060 and 5087 and found that the amount of Mg in the alloy can be represented by the spectrum variation. Song et al. [77] applied the optical emission spectrometer to detect laser-induced plasma and spectral line-intensity-ratio during laser additive manufacturing of Ti-Al alloy. The measured results together with the actual material composition were used to train a support vector regression (SVR) model for material composition estimation. Although the spectrometers could measure composition in plasma with high accuracy, to obtain optical spectrum during AM process, it generally requires the optical collector placed very close to the substrate (e.g. 1.5 mm [78]). Additionally, spectrometers detect the composition of plasma in the vapor but not in the solid. Under a given heating temperature, the different evaporation rate of different elements in the alloy lead to the fact that the composition in plasma is inconsistent with that of the alloy [76]. Such constraint limited the accuracy of spectrometers for composition measurement in additive manufacturing.

Besides the spectrum of the ionized alloy atoms, given the high temperature nature of the additive manufacturing process, the temperature profiles captured by visible light or infrared (IR) cameras are also widely studied to monitor the quality of the printed parts with a focus on the geometry accuracy, failure, and porosity. Krauss et al. [79] measured the temperature distribution surrounding the melt pool by an IR camera to detect void when Inconel 718 is melt during powder bed fusion process. It is found that the variation of heat conductivity, heat capacity and density of material induced by the voids can be represented in the change of temperature gradient from the captured thermal images. Mojtaba et al. [80] presented a similar approach to predict porosity from the temperature distribution. Craeghs et al. [81] built a failure detection system during layer-wise laser melting process by measuring the temperature distribution of melt pool. The deformation due to thermal stress and overheating during process were detected. Literature [82] predicted porosity at the corresponding position for DED by pyrometer and IR camera. Zhang et al. [83] applied high speed visible light camera to take photos during single line printing process in PBF. The features of melt pool, plume and spatters were extracted based on taken images. The track width as the quality evaluation index and extracted features were correlated by machine learning. Scime and Beuth [84] developed a methodology for monitoring the melt pool to detect flaws (under-melting, keyholing porosity, severe keyholing and balling) from the morphology of the captured image of melt pool. Kwon et al. [85] found the melt pool size measured through camera images are correlated with the microstructure and accordingly applied it to train a machine learning model to estimate the density of manufactured parts.

The prior research on temperature sensing for AM monitoring to detect defects or measure structural properties were based on the assumption that the material composition is fixed. The variation of temperature distribution induced by composition change has not been reported in the literatures. In this paper, a thermal imagining based in-situ monitoring method was developed for measuring alloy composition during additive manufacturing. The correlation between temperature distribution and material composition was theoretically built based on the Fourier’s law of thermal conduction. Experiments were conducted with mixed powder of Inconel 625 and Cu through laser PBF process. Temperature distribution images were experimentally recorded by an IR camera and then used to quantify the influence of material composition on temperature distribution. An Artificial Neuron Network (ANN) model was established to estimate material compositions based on temperature distribution. The experimental results were also analyzed and compared with the theoretical analysis.

The rest of this paper was organized as follows: Section 5.2 presented theoretical model of temperature distribution for metal alloy AM process and proved that the length of the temperature contour is a function of the element compositions in the alloy. Section 5.3 presented the setup of in-situ material composition monitoring system and experimental procedures. The feature extraction from thermal images and ANN model training were presented in Section 5.4. The results were analyzed in Section 5.5. Finally, a conclusion was given in Section 5.6.

5.2. Modeling

In the AM process, laser/electron beams provide energy to melt powders and make powders in liquid state on the build platform. Then the melted powder starts to solidify and form parts. During the melting and solidification process, temperature field around melting pool can be obtained. Literatures such as [86], [87] studied temperature field during AM process by experimental and numerical methods. According to their studies, the characteristics of temperature field around melting pools depend on variety factors, such as process parameters, powder properties, and powder distribution on the bed. The theoretical equations of temperature distribution were established and developed based on theory of thermal conduction as described in [88], [89]. In this section, the influence of material composition on temperature distribution was theoretically analyzed. For in-situ monitoring material compositions, the relationship between material composition and temperature field was correlated by ANN method. The principle and work flow of ANN method was introduced in Section 2.2.

5.2.1. Temperature distribution of AM Process

During the AM process, feedstock in powder or wire forms are melt by the energy from laser beam on the build plate. As the build plate is cooled by the surrounding air or coolant system supplied by the AM system, there is certain temperature gradient built around the melt pool. When the laser beam is stationary and the material properties are assumed as isotropic, the temperature contours surrounding the laser beam distribute on a series of co-centered circles. During printing, the laser beam scans across the build plate at a certain speed and accordingly stretches the temperature contours into oval shape. Based on Fourier's law of thermal conduction, a model [88], [89] can be built by assuming:

- The thermal properties of printed material are isotropic;
- The laser spot (e.g. 40 μm for Laser PBF) is far smaller than the size of the build plate;
- Initial temperature of the printed structure is T_0;
- Phase transition of printed alloy is not considered.

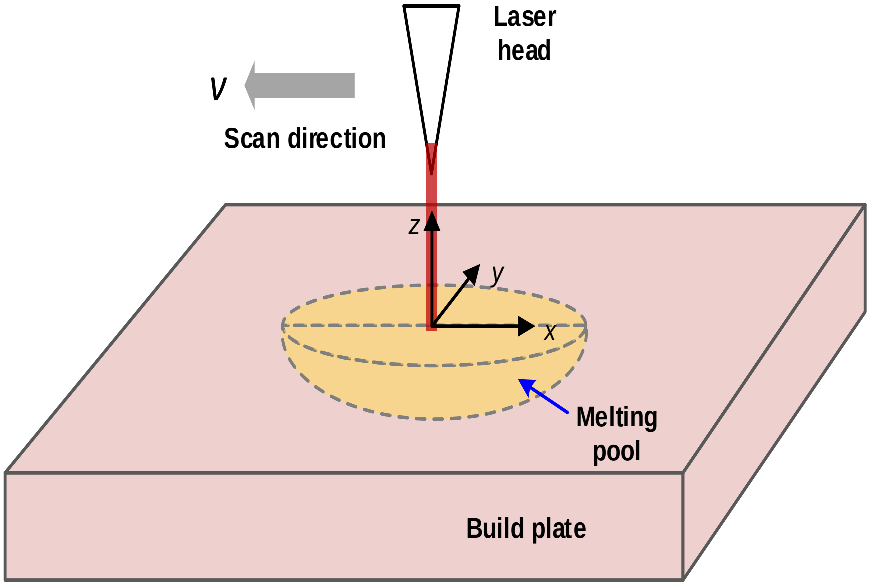

Figure 5.1 Schematic of L-PBF process

Figure 5.1 shows a simplified scheme according to the assumptions, where the laser head moves along *x* direction at velocity *v* and melts powders on the build plate. The thermal conduction on the build plate based on Fourier's law can be described as [88]:

$$\rho C \frac{\partial T}{\partial t} = k\left(\frac{\partial^2 T}{\partial x^2} + \frac{\partial^2 T}{\partial y^2} + \frac{\partial^2 T}{\partial z^2}\right) + Q(x, y, z, t),$$

$$x, y \in (-\infty, +\infty), \mathrm{z} < 0, \mathrm{t} > 0 \tag{5.1}$$

$$T(x,y,z,t) = T_0\ ,\ x, y \in (-\infty, +\infty),\ \ \mathrm{z} < 0,\ \ \mathrm{t} = 0$$

where ρ is density, C is the specific heat capacity, *k* is thermal conductivity, Q is the heat source function, T is temperature, *t* is time, *x*, *y*, *z* are the positions in the Cartesian coordinate system.

The Wilson-Rosenthal solution to Eq. (5.1) can be obtained when a single point heat source is applied to the location (0, 0, 0) [88]. When considering the distribution on the surface of the feedstock, by setting z to zero, the temperature can be expressed as:

$$T - T_0 = \frac{P\eta}{4\pi kR} \exp \frac{-\rho C v(\mathrm{R} - x)}{2k} \tag{5.2}$$

where $R = \sqrt{x^2 + y^2}$ is the distance from the point of interest to the center of the laser spot (0, 0), T_0 is the temperature of the environment, *P* is laser power, η is the absorption coefficient of the feedstock, and *v* is the laser scanning speed. For any given temperature T_m, the temperature contour (*x*, *y*, *z*) surrounding the laser spot can be expressed by forcing $T = T_m$:

$$T_m - T_0 = \frac{P\eta}{4\pi k\sqrt{x^2+y^2}} \exp\frac{-\rho C v(\sqrt{x^2+y^2}-x)}{2k} \tag{5.3}$$

At any temperature level T$_m$, Eq. (5.2) represents an oval contour surrounding the laser beam at (0, 0). The length of the oval contour is determined by the two ends where the contour intersects with the x-axis. Mathematically, the location of the two intersection points before and after the laser beam are expressed as (x_{Left}, 0) and (x_{Right}, 0), respectively. By substituting the locations in to Eq. (5.3) and solve the roots of the equations, the location of the right intersection point on the x-axis can be calculated as:

$$x_{Right} = \frac{P\eta}{4\pi k(T_m - T_0)} \tag{5.4}$$

For the intersection point on the left side where $x_{Left} < 0$, the exponential term in Eq. (5.3) is not zero. The solution of x_{Left} was calculated by approximating the exponential term with Taylor's expansion, and finally derived as:

$$x_{Left} \approx \frac{-1}{\frac{\rho C v}{k} + \frac{4\pi k(T_m - T_0)}{P\eta}} \tag{5.5}$$

Therefore, the length of the temperature contour can be calculated as:

$$L = x_{Right} - x_{Left} = \frac{P\eta}{4\pi k(T_m - T_0)} + \frac{1}{\frac{\rho C v}{k} + \frac{4\pi k(T_m - T_0)}{P\eta}} \tag{5.6}$$

Equation (5.6) shows that the length of temperature contour, when a fixed temperature level T_m and laser power P is selected, is a function of the thermal properties of printed material, i.e. density ρ, conductivity k, and heat capacity C.

Variation of these thermal properties induced by the change of material composition can be represented by the variation of the contour length.

To further demonstrate the relationships in application, the copper-nickel alloy that commonly studied [90] for AM was considered as an example. As Cu and Ni has similar density and heat capacity [91]. In this case, length of the contour can be assumed as a function of the thermal conductivity *k*. To combine the parameters other than *k*, let $\alpha = 4\pi(\mathrm{T_m} - T_0)/P\eta$, and $\beta = \rho C v$. Eq. (5.6) can then be rewritten as:

$$L = \frac{1}{\alpha k} + \frac{k}{\beta + \alpha k^2} \tag{5.7}$$

To study the variation of L when k changes, the derivative of L with respect to k was calculated based on Eq. (5.7), expressed as:

$$\frac{dL}{dk} = -\left(\frac{2\alpha^2 k^4 + \alpha\beta k^2 + \beta^2}{\alpha k^2 (\beta + \alpha k^2)^2}\right) \tag{5.8}$$

Physically, in Eq. (5.8), as all the parameters α, *β*, and *k* are positive real numbers, *dL*/*dk* is always negative. It suggests that when the conductivity *k* increases, the value of *L* monotonically decreases. In case the conductivity monotonically changes with the composition variation, i.e. increasing weight percentage of Cu in the Cu-Ni alloy, the Cu% can be retrieved from the measured contour length.

In Eq. (5.6), it is shown that the length of the oval contour is inversely proportional to the term (T_m – T). Namely, the contour size becomes small when a large T_m is selected. In practice, the measurement accuracy of contour length is constrained by the limited image resolution of the IR camera. When increasing T_m, the contour size reduces and the number of pixels covering the contour reduces accordingly. As a result, the measurement accuracy will reduce. Another consideration of selecting T_m is to avoid the region where the phase of alloy transits between liquid and solid, which was not considered in the analytical model. Additionally, when T_m is selected too low, the temperature contour is also subject to noises and disturbances such as spattering in experimental test. Summarizing all of factors, this study chooses T_m on a level right below the melting temperature of the alloy in the realistic tests.

Similar to the length, the width and coverage area of temperature contour can also be approximated a function of the thermal properties and process parameters. Such relationships can be used as the basis for retrieving the material composition from temperature contour measurement.

To demonstrate the process, an example is calculated using alloy containing Cu and Ni. As the properties of Cu-Inconel625 at different composition levels is not available in the literatures, the example considered a similar alloy made of Cu-Ni [90]. Thermal properties of the Cu-Ni alloy, expressed by Ni or Cu weight percentage, has been experimentally measured in [92], as listed in Table 5.1. Similar to the Cu-Inconel 625, it is seen that the density of the alloy doesn't show apparent variation at different composition levels, but the thermal conductivity increases more than 15 times when the weight percentage of Cu increases from 28% to 99%.

Table 5.1 Thermal properties of Ni and Cu based materials [92]

	Inconel 400	CuNi44	CuNi25	CuNi10	CuNi6	CuNi2	Cu
Ni composition, (%)	63	44	25	10	6	2	0
Cu composition, (%)	28-34	56	75	90	94	98	99.9
Thermal conductivity, k, (W/m K)	21.8	23	29	59	92	130	388
Density, ρ, (10^3 kg/m^3)	8.9	8.9	8.9	8.9	8.9	8.9	8.9

Specific heat, C, (10^3 J/kg C)	0.49	0.41	0.38	0.38	0.38	0.38	0.38
Melting point (°C)	1440	1260	1181	1100	1095	1090	1074

Based on the data given in Table 5.1, the temperature contours of different material compositions were numerically calculated accordingly to Eq. (5.3), under consistent laser power (200W) and scanning speed (100 mm/s). Figure 5.2 (a-d) shows the calculated temperature contours when T_m is 1000°C, 1500°C, and 2000°C for different alloy compositions. It is seen that, for each T_m level, the size of the oval-shape temperature contour decreases with the increase of Cu% in the alloy, due to the increase of conductivity (Table 5.1).

To quantify the relationship between contour size and composition, the length, width, and coverage area of the oval contours are extracted and plotted in Figure 5.3. It is seen from Figure 5.3 (a) that both the length and width of the oval temperature contour are sensitive to the composition level especially when the Cu % is greater than 50%, as the apparent increase of conductivity as given in Table 5.1. The coverage area of the temperature contour also shows a similar trend, as seen in Figure 5.3 (b). The monotonic relationships suggest that all of the three features, length, width, and coverage area of the temperature contours could be used to retrieve the composition level in practice.

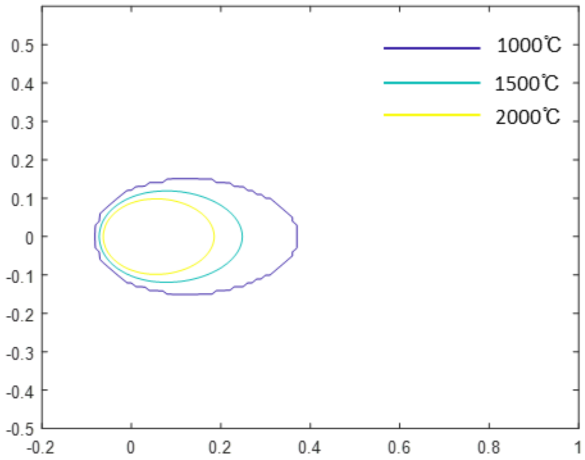

(a) Inconel400 (Cu 28-34%)

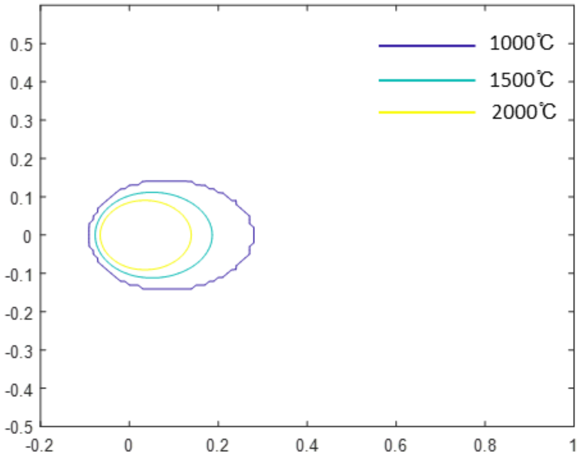

(b) CuNi 25(Cu 75%)

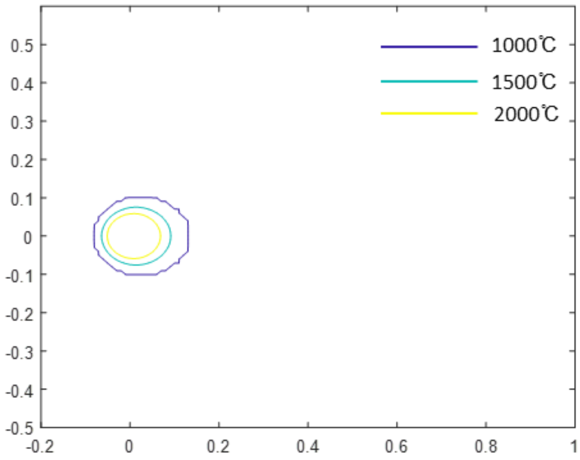

(c) CuNi10 (Cu 90%)

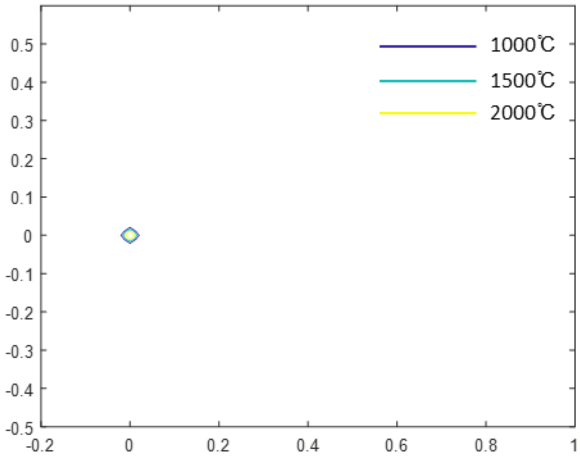

(d) Cu

Figure 5.2 Contour of temperature field with same threshold for different materials

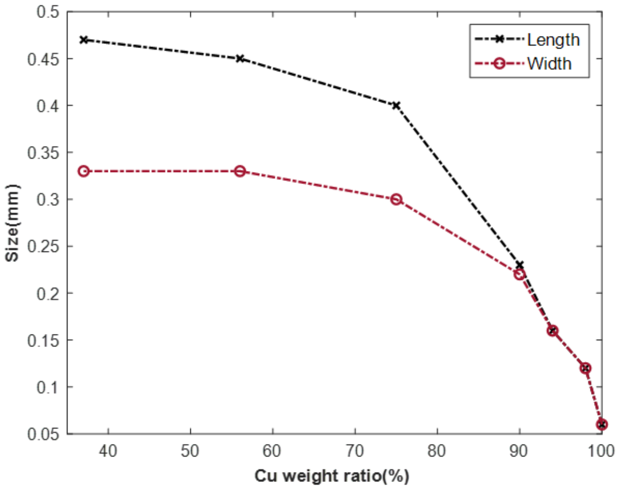

(a) Length and Width

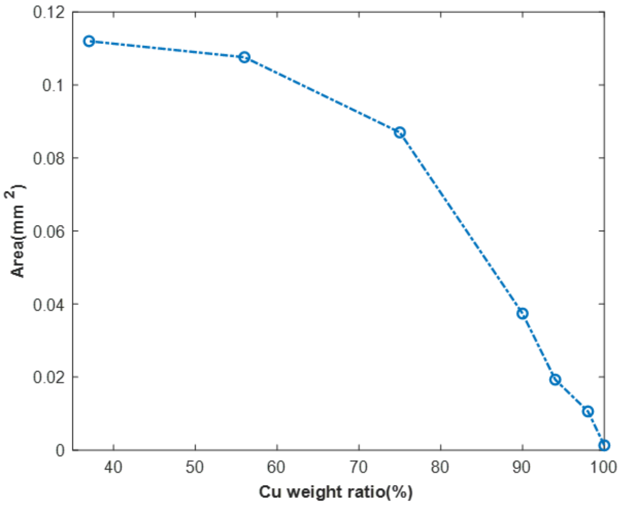

(b) Area

Figure 5.3 Characteristic of temperature field with Ni weight ratio under same temperature threshold

Although the analytical model proved the overall relationship between the contour features and composition levels, in realistic application, considering the presence of measurement error, actual material properties at each temperature range, and physical noises during the additive manufacturing process, it is challenging to provide precise estimation. In practice, the extracted contour features were correlated with the composition levels through a machine learning model to estimate the detailed relationship from experimental data. Within the various algorithms developed in the literatures [93], [94], this work adopts Artificial Neural Network due to its advantages in learning complex relationship.

5.2.2. Artificial Neuron Network

ANN is a modelling method inspired by human brain that allows learning complex relationship by examples from collected data that describe a physical phenomenon or a decision process [95]. ANN can be applied to build classification and regression models to achieve pattern or character recognition[96], [97], optimization and prediction[98]. It has wide applications in data processing[99], sensor applications[100], system control and so on[101].

Figure 5.4 shows the schematic of ANN model. Two processes are included in ANN model: feed forward process to transfer input information to output by functions; back propagation process to evaluation errors between transferred results and expected results. The errors can be regarded as feedback to the built functions in the feed forward process. The parameters in the function would be adjusted based on errors. Figure 5.4 (a) also shows the architecture of ANN. It includes one input layer, one output layers and some hidden layers. Each layer has nodes to transfer information between layers. In Figure 5.4 (a), there are 2 hidden layers with 3 and 4 nodes in each layer respectively. There is weight associated with input when information is transferred between nodes as $w_{i,j}$ in Figure 5.4 (a). Weight effects the input contribution to the training algorithms. The higher value of weight makes stronger connection between input and output. Weights are adjusted during training process according to the feedback from back propagation process. The sum of multiplying weights by inputs formed the input to the nodes at next layer. An activation function is applied to generate output. Take the information transfer between input layer and first hidden layer as an example, the input to the node *h* at the hidden layer can be calculated as:

$$h_{1j} = f(\sum_{i}^{n} w_{\mathrm{ij}} p_{\mathrm{i}} + \mathrm{bias}) \tag{5.9}$$

where *i* is the index of input *p* and *j* is the index of nodes at first hidden layers. The bias is the error between input layer and first hidden layer calculated by back propagation process. *f* is activation function. In this chapter, the sigmoid activation function is applied to train the model. The formation of sigmoid function is shown as below:

$$h = f(p) = \frac{1}{1+e^{-p}} \tag{5.10}$$

where *p* is the input to nodes and *h* is the output at nodes.

Figure 5.4 (b) presented the flow chart of the developed ANN model where the input variables are processed with the sigmoid functions through intermediate layers, and then compared with the ground truth read to calculate the RMSE error, expressed as:

$$RMSE = \sqrt{\frac{\sum_{n=1}^{N}(q_n - \hat{q}_n)^2}{N}} \tag{5.11}$$

where N is the total number of output, q_n is the *n*th actual output, $\hat{q}_n$ is the *n*th output calculated by trained model. The RMSE error were back propagated (Levenberg-Marquardt algorithm) from output layer to the input layer. The weights associated with each node connection were updated according to the value of the error, and repeated through iterations until the error is less than a threshold.

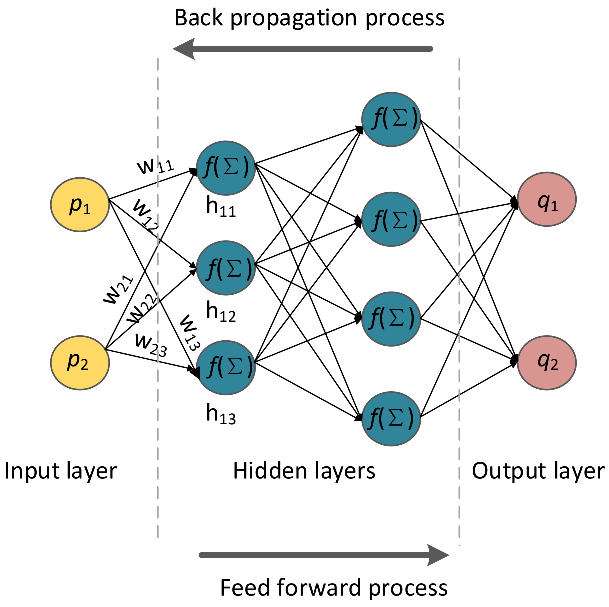

(a) schematic

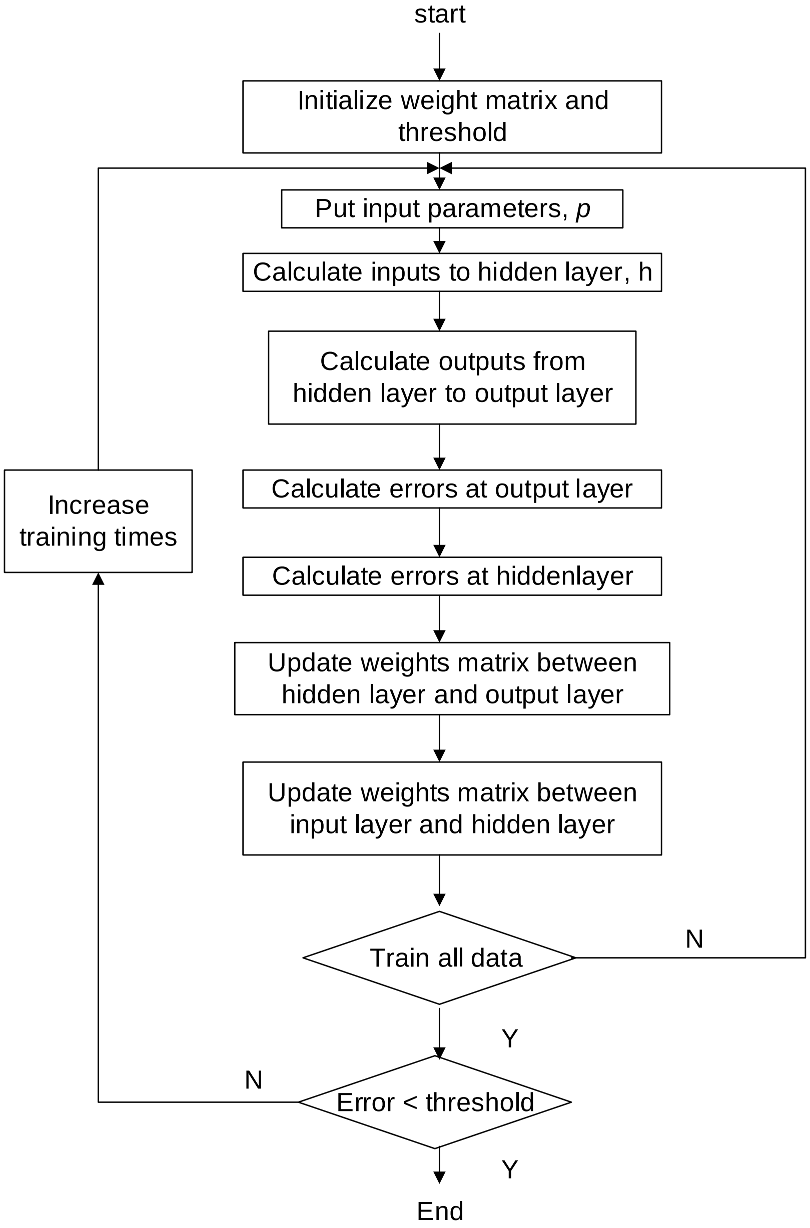

(b) Training flow
Figure 5.4 ANN model

5.3. Experimental procedure

According to the theoretical analysis and ANN model establish in Section 5.2, the in-situ monitoring of material composition during AM process was presented. In this section, experimental study was carried out to validate proposed method. The experiments tested the copper-inconel625 alloy, in which the major active components are Cu and Ni, being consistent with the theoretical analysis. IR camera was applied to acquire temperature filed during process. The sensing system and experimental setup are introduced as below.

5.3.1. In-situ sensing system setup

Figure 5.5 (a) shows the scheme of built experimental platform. It includes two parts: Laser PBF (L-PBF) machine and IR camera. Mix powders were additive manufactured on the powder bed of L-PBF machine. The IR camera was installed above the powder bed to acquire temperature field during process. The field of view of IR camera was fix by this installation scheme. Figure 5.5 (b) shows the in-situ sensing system setup. The L-PBF machine, OR Laser Creator, was applied to conduct experiments. The machine was composed by a fiber laser, powder spreading system and a controller panel. The Yb fiber laser can provide maximum 250 W power with 1070 nm wavelength. Material powders deposited on the powder bed through a scraper. The Argon gas is filled in the chamber to avoid material oxidation during printing process.

An IR camera, Optris PI 1M, was installed above the powder bed with an angle to acquire temperature field. The maximum frame rate of the IR camera is 1KHz for temperature measurement from 600°C to 1800°C. There is a compromise between frame rate and total number of sampling pixels. High frame rate can catch the characteristic of fast laser-material interaction dynamic process, but this makes the computation cost with large number of sampling pixels high. For characterizing temperature field during fast dynamic process, a high frame rate of 1KHz was applied with 72 x 56 sampling pixels. In order to obtain absolute temperatures of temperature field by IR camera, the emissivity of measured objects need to be known before test. However, the emissivity is hard to be determined since it depends on varieties of factors, such as material type, material state and surface flatness. For single type of material AM process, emissivity of the measured material would be determined by rough calibration with solid state. The emissivity was adjusted based on reference measurements from thermocouples [102]. As the emissivity of the copper-Inconel625 alloy at high temperature is not available from the literatures, this study assumes a consistent emissivity of 1.0 for all composition levels in calculating the temperature of each pixel from the captured IR intensity in the thermal images [79].

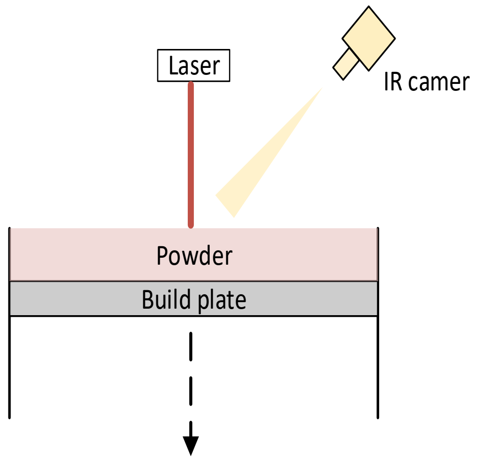

(a) Scheme

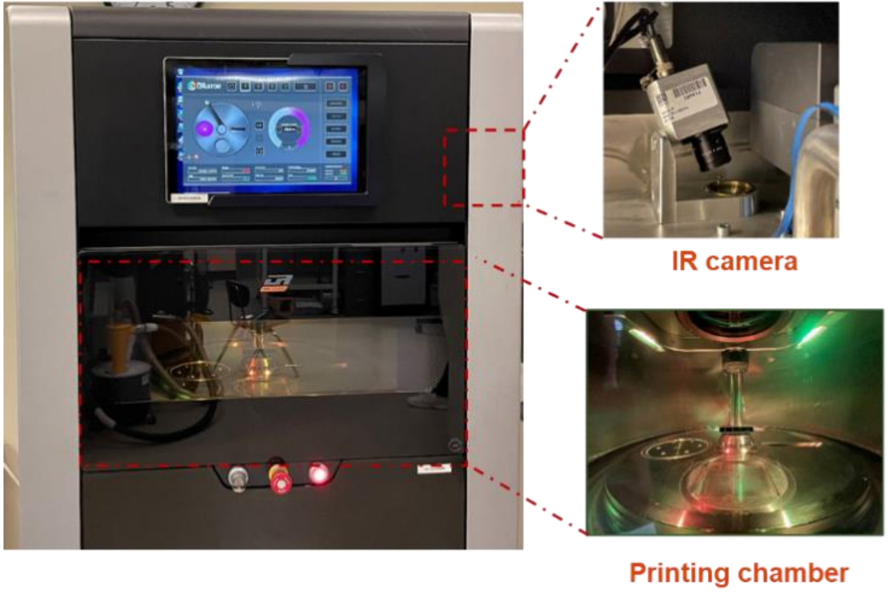

(b) Experimental setup
Figure 5.5 In-situ monitoring system

5.3.2. Experimental setup

Experiments with different material compositions were conducted by the L-PBF machine. The materials applied in the experiments are Inconel 625 and Cu. Table 5.2 presents the designed weight ratios of these two materials in each group test. This study approximated the composition of the printed structure with that of the mixed powder, by ignoring the variations induced from different vaporization temperature of each element. Through preliminary tests, the printing setups selected laser power as 200W and scanning speed as 200 mm/s, which guarantees the materials at all composition levels can be properly melted and deposited on the build plate. For each composition level, the temperature contours were extracted from the images when the laser spot scanning across 18 positions on the rectangular paths.

The experiments tested single tracks printed in rectangular shape, 2.54 x 54 mm, as shown in Figure 5.6. The view zone of the IR camera covers the middle section of the rectangular paths. With preliminary tests, the spatial resolution of IR camera is 0.25 mm. The view zoon of IR camera with 72 x 56 pixels is 18mm x 14mm. The temperature contours were extracted from the images when the laser spot scanning across 18 positions on the rectangular paths. The track length is much longer than the view zoon that can avoid signal fluctuations resulted from laser turns on/off [103].

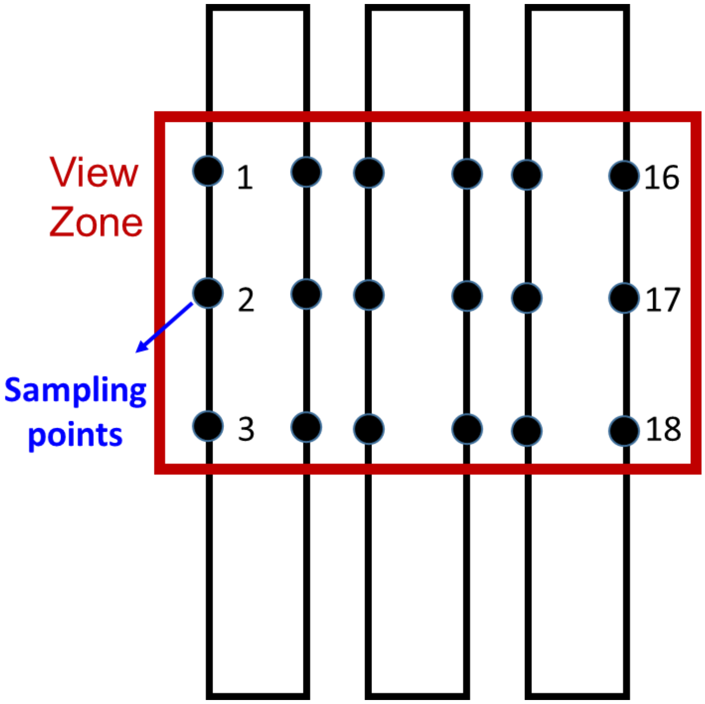

Figure 5.6 Additive manufactured sample

Table 5.2 Weight ratios of materials in experiments

Group	1	2	3	4	5
Cu, %	100	80	50	20	0
Inconel 625, %	0	20	50	80	100

5.4. Signal Processing

Figure 5.7 shows some of the sampled images captured on position 1-3 by the IR camera in printing the mixed powder at different composition levels. The grayscale of each pixel from dark (black) to bright (white), represents the temperature range from 600˚C to 1200 ℃. When the Inconel 625 with 0% of Cu is being printed, strong spattering is observed during printing due to the low conductivity of Inconel 625 and the consequent high temperature when being heated by the laser beam.

In each image, it consists of a dark background and different bright spots in foreground. These bright spots represented the radiations emitted at the laser heated zone. Comparing these images, it is shown that the shape and size of bright spots varies with weight ratios of powders. For printing powder without Cu, bright spots are large and elongated along printing direction. With the increment of Cu, the bright spots become smaller and closer to circles. The trend of bright spots varies with weight ratio of powders obtained from IR camera is similar with results from theoretical analysis as shown in Figure 5.3. For quantitatively correlate the relationship between temperature field and material composition, features in the captured images need to be extracted.

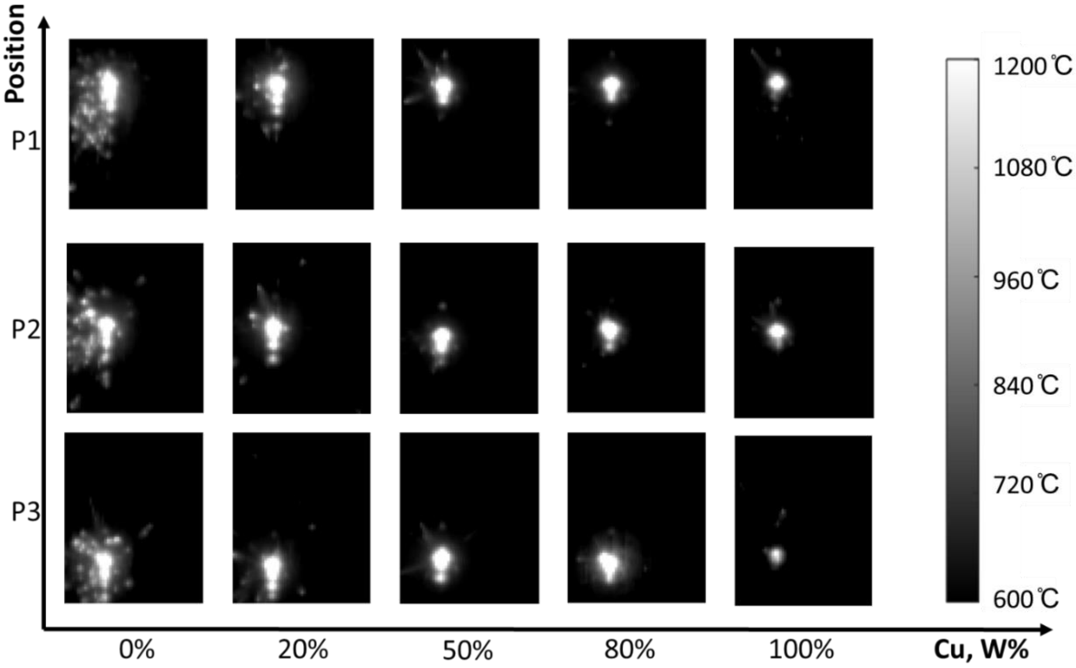

Figure 5.7 Images from IR camera with different Inconel weight ratio

5.4.1. Feature extraction

This study considers using all the three extracted features, length, width, and area of the temperature contour as the input of the ANN model. Although the three features are not fully independent from each other, in experiments, the disturbances during printing process, such as spatters, induced certain amount of errors and noises in each of them. Single feature with noise may induce bias in the model. Therefore, considering all three features in the model can reduce the errors induced by disturbances. Figure 5.8 shows the technical steps to process the raw images through *resampling* and *thresholding*. The image resampling interpolated 10 points in both x and y directions for each pixel, and increased the resolution of image 10 times from 72 x 56 pixels to 720 x 560 pixels. The thresholding is then applied to generate a binary image to extract the temperature contour at T_m. Based on threshold determination algorithm, image thresholding methods can be categorized as: histogram-based, clustering-based, entropy-based, attribute-based, spatial and local methods [104]. These methods can determine the threshold to separate foreground and background for individual images according to characteristic of images. The most suitable thresholding method is problem-dependent [105]. In this chapter, same greyscale threshold was applied on all images obtained with different material compositions. By thresholding with same greyscale value, the contours of foreground parts were formed with same value which can match with theoretical analysis in Section 5.2.1. Figure 5.8 shows the binary image formed after thresholding. The length, width and area of foreground can be numerically extracted from binary images.

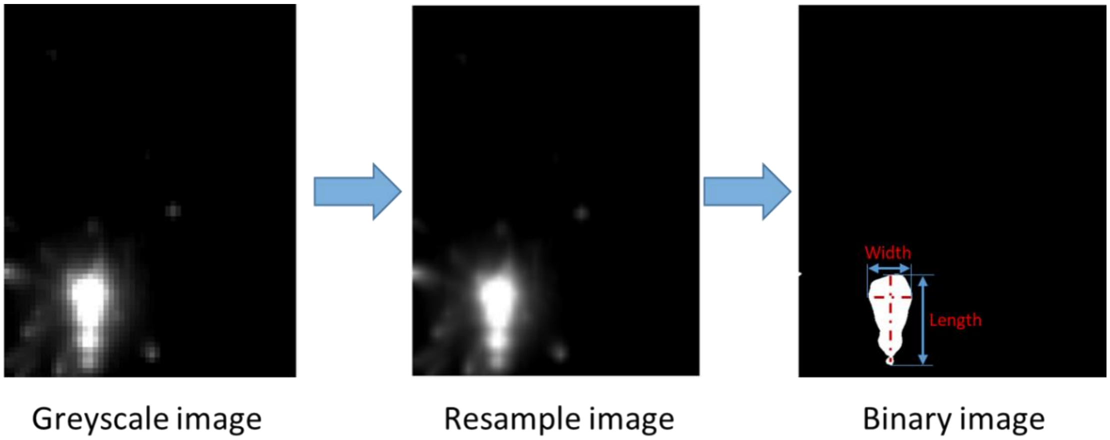

Figure 5.8 Image processing process for feature extraction

5.4.2. ANN model built-up

To correlate the extracted features with the material composition acquired from premixed powder, the ANN model was applied. In the model, the input parameters are the features extracted from images acquired by IR camera. As introduced in Section 5.4.1, there are three input parameters for ANN model including length, width and area of the contour. The output is the weight ratio of Cu in the mix powder. Considering the five composition levels being tested, from 0% to 100% of Cu in the alloy, and the contours are sampled at 18 potions on the laser scanning path, there are in total 90 sample images collected through the experiment. For training ANN model and validating model performance, 70% of samples are randomly selected as training set, 15% of samples are randomly selected as validation set and 15% of samples are randomly selected as test set.

For ANN model, the regression performance was determined by both data set and model architecture. The number of layers and neurons have significant influence on evaluation accuracy. In this chapter, the architecture of ANN model was determined based on evaluation accuracy of built model. The ANN model was designed with 2 hidden layers. The number of neurons in each layers was designed from 1 to 30. The trained models with different number of neurons were compared to obtain accurate and robust model.

5.5. Results

Following proposed image processing and machine learning method introduced in Section 5.4, features in images and correlation between features and material compositions can be obtained. Figure 5.9 shows the extracted length, width, and coverage area of the contours at different material composition levels, where the data point and error bar representing the average and standard deviation of the extracted values, respectively. It is seen that all three extracted feature values decrease with the increase of Cu percentage in the alloy, being consistent with the trend predicted by the analytical model (see Figure 5.3). Compared with the other Cu levels in the curves, the large standard deviation when Cu is 0% (when single Inconel 625 was printed) was observed, due to the noises caused by serious spatters (see Figure 5.7).

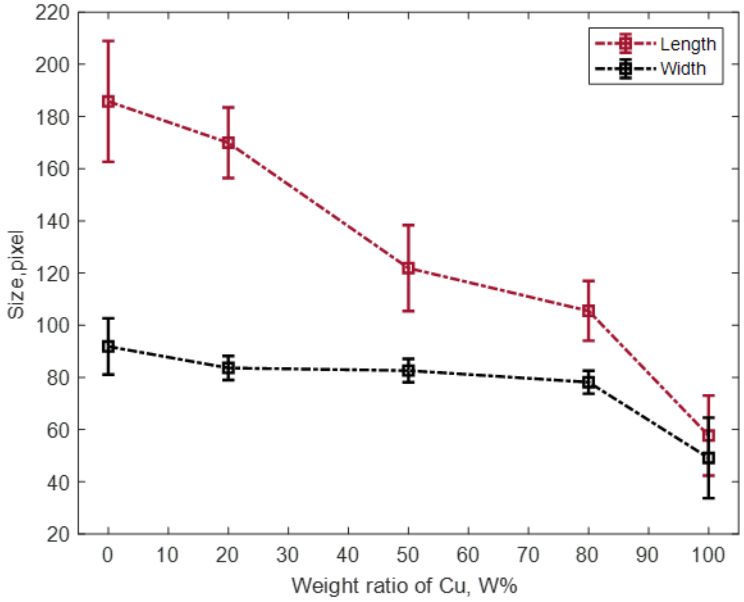

(a) Length and width

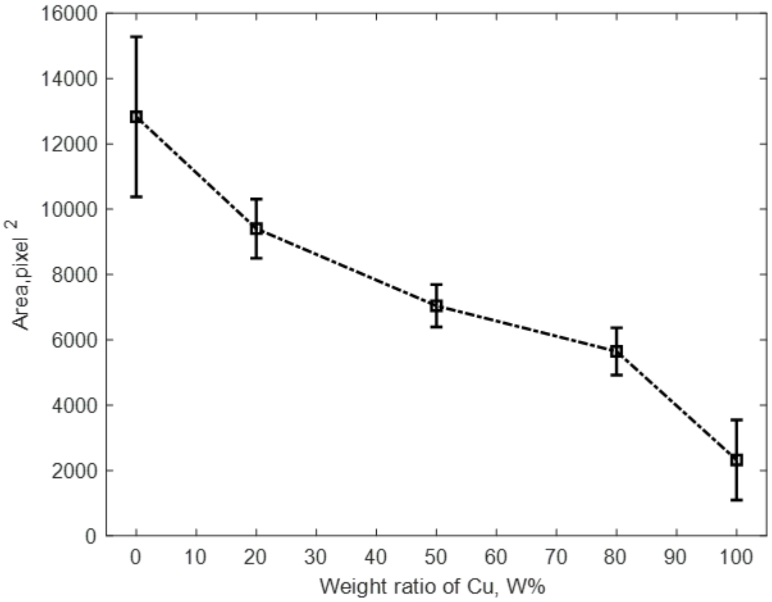

(b) Area

Figure 5.9 Features extracted from images vs. material compositions

For building ANN model with high accuracy and robustness, the model performance with different number of neurons in hidden layers were evaluated. Figure 5.10 shows architecture of ANN model with two hidden layers. The number of neurons is i in first hidden layer and j in second hidden layer. Both i and j are from 1 to 30. The evaluation performances with different architecture of ANN models were analyzed and compared. Figure 5.11 shows the RMSE calculated from training data and validation data with different number of neurons in hidden layers. It is shown that the accuracy of ANN predictions varied with the ANN architectures. For training data, most of ANN architectures obtained similar RMSE which means most of ANN architectures work well. When there is only one neuron in hidden layers, the RMSE is higher than other cases. For validation data, when i is larger than 10, the calculated RMSE started to increase. Comparing evaluation performance for training data and validation data, it is known that over fit happened when i is larger than 10. Through analyzing results in Figure 5.11 (a) and (b), i=10 and j=10 were determined to build a two hidden layer ANN model.

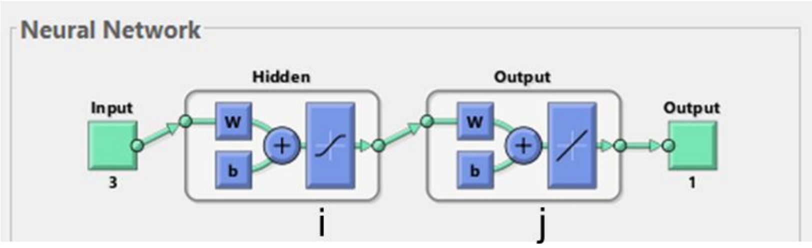

Figure 5.10 Architecture design of ANN model

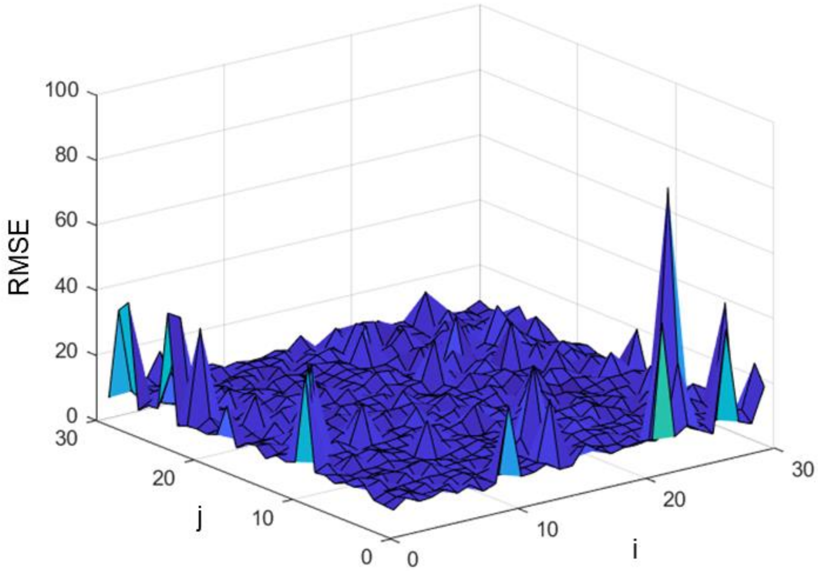

(a) Training set

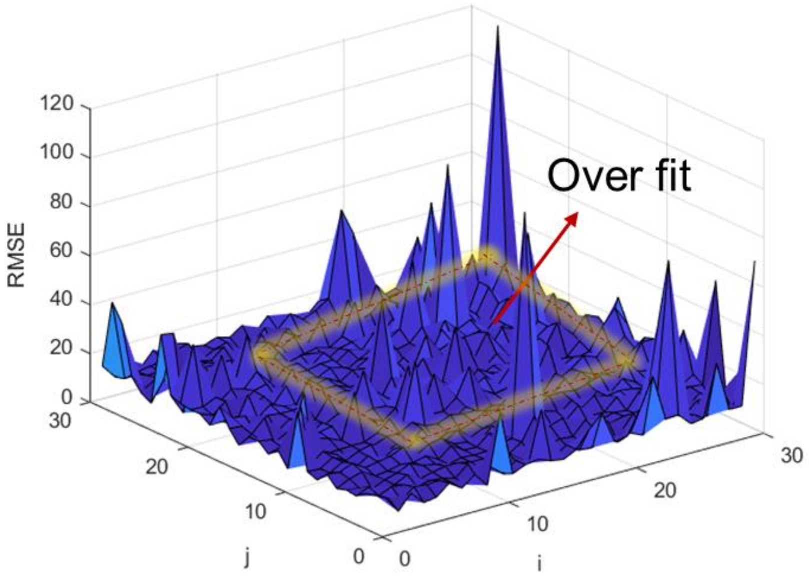

(b) Validation set

Figure 5.11 Performance evaluation of designed ANN model with different number of neurons

Figure 5.12 shows the estimated and actual composition in one of the randomized test group by determined ANN model. The averages and standard deviations of estimated results for each composition level were calculated and presented in the figure. It is shown that the predicted weight ratios are close to true weight ratios. The statistical performance evaluations for each set of data was shown in Table 5.3. The RMSE of predicted results ranged from 6.12% to 6.66% in three sets of data, which showed the high accuracy of predicted results. The variations among RMSE in different data sets were less than 0.54% which demonstrated the robustness of trained ANN model. The coefficients of linear fit between predicted results and true values were in the range of 0.97-0.98 which indicated the high consistency of the predicted results and true results.

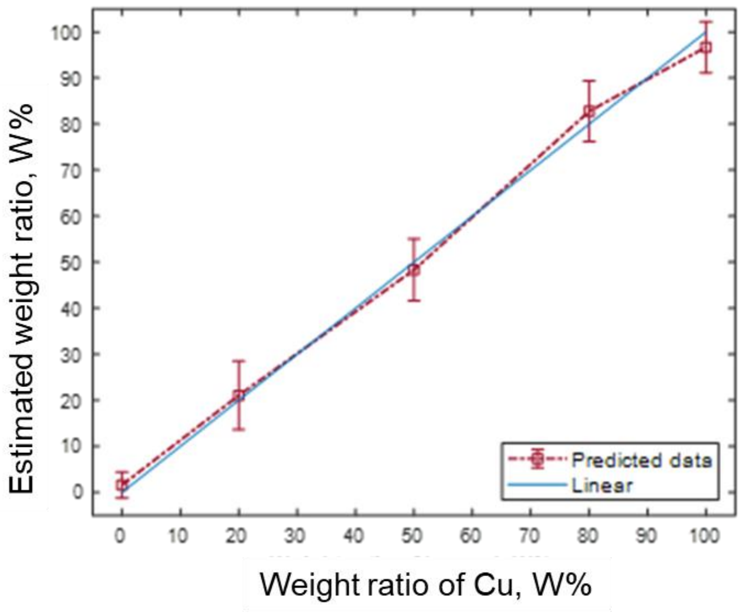

(a) Training set

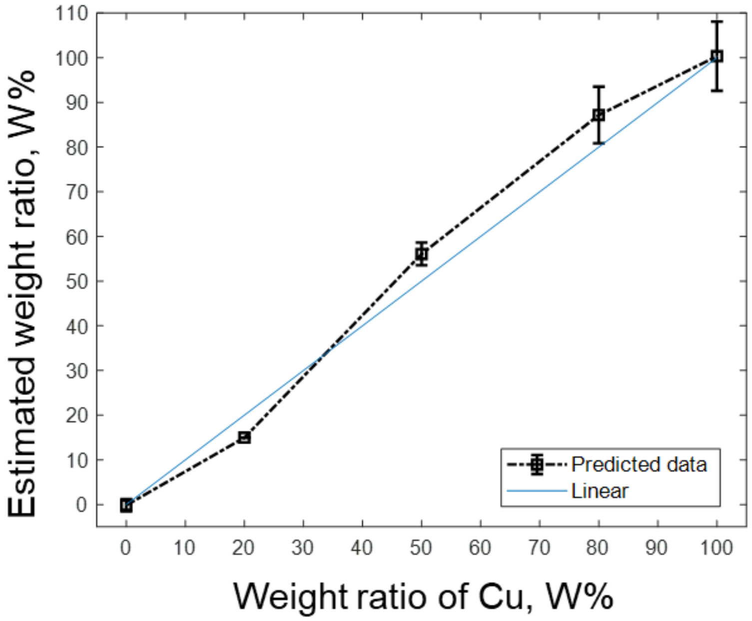

(b)Validation set

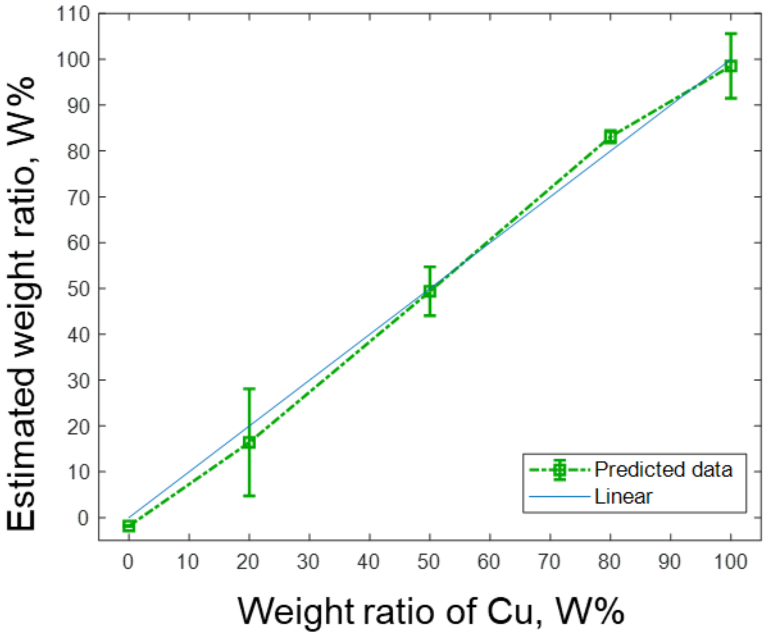

(c) Test set

Figure 5.12 Performance evaluation of designed ANN model

Table 5.3 Statistical performance evaluation of ANN model

	% of samples	RMSE,%	Linear coefficient, R
Training set	70	6.19	0.98
Validation set	15	6.12	0.97
Test set	15	6.66	0.98

To study the stability of the estimation, the randomized data selection for training, validation, and testing were repeated for 50 times. Figure 5.13 shows the errors and standard deviations of the estimated composition of all the 50 repeats. It is seen in Figure 5.13 that the average estimation error for each composition level is less than 6%. Figure 5.13 (b) shows that the standard deviations of estimation results in each composition level is less than 9%. Compared with other composition levels, the large standard deviation when Cu is 0% was observed due to the high noise level in thermal images and extracted features (see Figure 5.7 and Figure 5.9).

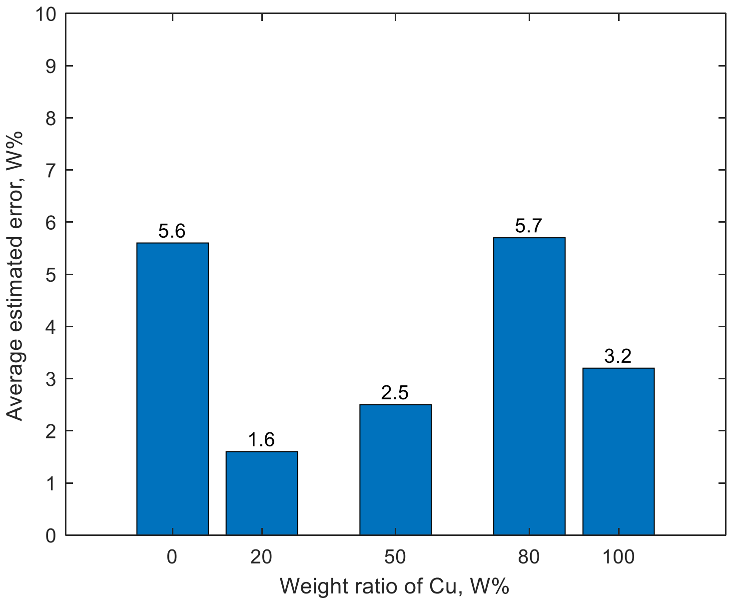

(a) Average estimation error

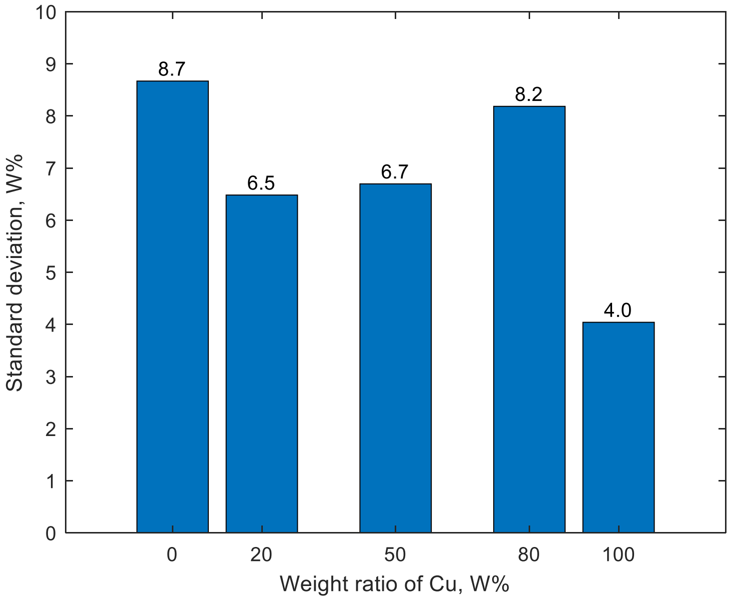

(b) Standard deviation

Figure 5.13. Stability tested by repeating the test for 50 times

5.6. Conclusion

This paper introduced a new in-situ material composition monitoring method for additive manufacturing process. The developed method estimates the material composition from the size of temperature contour that can be measured through Infrared cameras. An analytical model of the developed method was built based Fourier's Law of thermal conduction. It is proved that the length of the oval temperature contours is a function of the thermal properties of the alloy. In case the alloy thermal properties are monotonic function of the composition, the method has been proved being effective to measure the composition. Based on the known material properties, the method has been demonstrated using Cu-Ni alloy as an example. To validate the theoretical model, experiments tested five composition levels of Cu and Inconel 625 on a commercial Laser PBF machine. Dimensions of temperature contour from thermal images were extracted. The experimental results showed that the length, width, and coverage area of the temperature contour monotonically decreases with the increase of weight percentage of Cu in the alloy, being consistent with the theories. To make use of the relationship for composition measurement, an Artificial Neural Network model was built and trained by the experimental data. Test results showed that the trained ANN model estimated the composition with an error less than 5.7%. It indicates that the developed method can be used for monitoring the material composition in-situ. Such a capability would be significant, especially, for printing binary material or functional graded materials where accurate control of the material composition is demanded.

Chapter 6. Conclusions

This thesis focused on developing advanced, intelligent and flexible optical sensing and metrology system to achieve real-time and non-destructive monitoring for two applications: 1) structural health test for compact heat exchanger 2) bimetallic AM process monitoring. Mathematical and intelligent algorithm were introduced in the sensing strategies to characterize complex and dynamic system with high accuracy and low cost. The testing systems were designed and setup based on optical sensing theories and knowledge of testing targets in Structural, Mechanics and Physics. The sensing data from experiments were analyzed and compared with theoretical or numerical results. Contributions of this thesis are summarized as follows.

Chapter 2 presented the model, simulation, and validation of a new crack detection technique for monitoring the crack development within complex structures. A novel diagnosis model was built to predict crack positions based on limited sampling data in structure. A geometric-true numerical model of a sensor-embedded compact heat exchanger was built on ANSYS platform to evaluate the strain variation under different temperature and pressure conditions. The crack position detection algorithm was developed based on Tikhonov regularization. The detection accuracy of the proposed method was verified by simulations considering variety of sensor installation scheme, crack positions and crack dimensions.

In chapter 3, strain transfer characteristic of optical fiber strain sensors was studied to compensate measurements and improve measurement accuracy. An analytical model was built based on mechanical equilibrium. Compared to the previous work, proposed analytical model considered both mechanical and thermal effects on strain transfer. The built model can be applied to improve measurement accuracy for system in high temperature and high pressure environment. The analytical model was verified by experiments under different mechanical and thermal loads. It is shown that developed theoretical model well matches with experimental results with high accuracy up to 97.6%.

In chapter 4, an experimental platform was designed and setup to test optical fiber strain sensor responses when elastic, plastic deformation and crack growth presents in the PCHE. The feasibility of embedding distributed optical fiber strain sensors to detect micro cracks for PCHE was investigated. The experimental results were compared with finite element analysis (FEA) results. Experimental results demonstrated that optical fiber sensor had responses when crack presented in the PCHE during elastic, plastic deformation and crack growth. As a component affecting the crack detection accuracy, the fiber coating was discussed to quantify its correlation with the strain measurement results.

In Chapter 5, a novel in-situ sensing method for material composition identification during bimetallic AM process by IR camera was proposed. The proposed sensing method was based on temperature field analysis and intelligent algorithms. Comparing with previous research that focused on single material AM, the proposed method correlated the relationship between temperature field and material composition theoretically and experimentally. An IR camera was installed to capture temperature field with different material compositions during AM process. The features of temperature field were extracted through image processing and correlated with material compositions through Artificial Neural Network (ANN) method. The trained ANN model can predict material compositions with the error less than 6.6%. This prediction results demonstrated that the proposed method can be applied on in-situ material composition evaluation for AM process.

The scientific contributions of this thesis work are summarized as:

1) The work first introduced the concept of embedded distributed strain sensing for structural health monitoring and developed a physical and mathematical solution for retrieving the location of cracks through strain data measured by optical fiber sensors.

2) The work first introduced both mechanical and thermal load in the model of strain transfer rate and provided a theoretical basis for accurate measurement of strain with the presence of temperature variation.

3) The work first presented the correlation between the temperature contour and material composition in additive manufacturing, from theoretical perspective. Such a relationship was mathematically proved being effective for measuring the alloy composition and finally validated through experiments on a commercial laser powder bed fusion system.

Bibliography

[1] B. Culshaw and A. Kersey, “Fiber-Optic Sensing: A Historical Perspective,” *Journal of Lightwave Technology*, vol. 26, no. 9, pp. 1064–1078, May 2008, doi: 10.1109/JLT.0082.921915.

[2] K. O. Hill and G. Meltz, “Fiber Bragg grating technology fundamentals and overview,” *Journal of lightwave technology*, vol. 15, no. 8, pp. 1263–1276, 1997.

[3] A. Barrias, J. Casas, and S. Villalba, “A Review of Distributed Optical Fiber Sensors for Civil Engineering Applications,” *Sensors*, vol. 16, no. 5, p. 748, May 2016, doi: 10.3390/s16050748.

[4] P. Ferdinand, “The evolution of optical fiber sensors technologies during the 35 last years and their applications in structure health monitoring,” presented at the EWSHM-7th European Workshop on Structural Health Monitoring, 2014.

[5] G. Rodriguez, J. R. Casas, and S. Villalba, “SHM by DOFS in civil engineering: A review,” *Structural monitoring and maintenance*, vol. 2, no. 4, pp. 357–382, 2015.

[6] M. Froggatt and J. Moore, “High-spatial-resolution distributed strain measurement in optical fiber with Rayleigh scatter,” *Appl. Opt.*, vol. 37, no. 10, p. 1735, Apr. 1998, doi: 10.1364/AO.37.001735.

[7] M. G. Tanner, S. D. Dyer, B. Baek, R. H. Hadfield, and S. Woo Nam, “High-resolution single-mode fiber-optic distributed Raman sensor for absolute temperature measurement using superconducting nanowire single-photon detectors,” *Applied Physics Letters*, vol. 99, no. 20, p. 201110, 2011.

[8] J. Park *et al.*, “Raman-based distributed temperature sensor with simplex coding and link optimization,” *IEEE Photonics Technology Letters*, vol. 18, no. 17, pp. 1879–1881, 2006.

[9] S. Bagavathiappan, B. B. Lahiri, T. Saravanan, J. Philip, and T. Jayakumar, “Infrared thermography for condition monitoring – A review,” *Infrared Physics & Technology*, vol. 60, pp. 35–55, Sep. 2013, doi: 10.1016/j.infrared.2013.03.006.

[10] A. Kylili, P. A. Fokaides, P. Christou, and S. A. Kalogirou, “Infrared thermography (IRT) applications for building diagnostics: A review,” *Applied Energy*, vol. 134, pp. 531–549, 2014.

[11] J.-H. Eoh, H. C. No, Y.-H. Yoo, and S.-O. Kim, “Sodium-CO2 interaction in a supercritical CO2 power conversion system coupled with a sodium fast reactor,” *Nuclear Technology*, vol. 173, no. 2, pp. 99–114, 2011.

[12] J.-R. Lee, H. Jeong, C. C. Ciang, D.-J. Yoon, and S.-S. Lee, “Application of ultrasonic wave propagation imaging method to automatic damage visualization of nuclear power plant pipeline,” *Nuclear Engineering and Design*, vol. 240, no. 10, pp. 3513–3520, Oct. 2010, doi: 10.1016/j.nucengdes.2010.06.011.

[13] M. S. Safizadeh and M. Hasanian, “GAS PIPELINE CORROSION MAPPING USING PULSED EDDY CURRENT TECHNIQUE,” vol. 5, no. 1, p. 8, 2011.

[14] M. Z. Abdullah, N. A. Ashaari, and M. A. Aziz, “Development of a neutron tomography system for industrial applications,” *Measurement*, vol. 42, no. 7, pp. 1017–1026, Aug. 2009, doi: 10.1016/j.measurement.2009.03.003.

[15] A. A. Carvalho, J. M. A. Rebello, L. V. S. Sagrilo, C. S. Camerini, and I. V. J. Miranda, “MFL signals and artificial neural networks applied to detection and classification of pipe weld defects,” *NDT & E International*, vol. 39, no. 8, pp. 661–667, Dec. 2006, doi: 10.1016/j.ndteint.2006.04.003.

[16] A. Turnbull, L. Wright, and L. Crocker, “New insight into the pit-to-crack transition from finite element analysis of the stress and strain distribution around a corrosion pit,”

Corrosion Science, vol. 52, no. 4, pp. 1492–1498, Apr. 2010, doi: 10.1016/j.corsci.2009.12.004.

[17] Y. Lee and J. I. Lee, “Structural assessment of intermediate printed circuit heat exchanger for sodium-cooled fast reactor with supercritical CO2 cycle,” *Annals of Nuclear Energy*, vol. 73, pp. 84–95, Nov. 2014, doi: 10.1016/j.anucene.2014.06.022.

[18] “Luna ODiSI system data sheet.”

[19] H. W. Engl and H. Gfrerer, “A posteriori parameter choice for general regularization methods for solving linear ill-posed problems,” *Applied Numerical Mathematics*, vol. 4, no. 5, pp. 395–417, 1988, doi: https://doi.org/10.1016/0168-9274(88)90017-7.

[20] G. H. Golub, M. Heath, and G. Wahba, “Generalized Cross-Validation as a Method for Choosing a Good Ridge Parameter,” *Technometrics*, vol. 21, no. 2, pp. 215–223, 1979, doi: 10.2307/1268518.

[21] P. C. Hansen, “Analysis of Discrete Ill-Posed Problems by Means of the L-Curve,” *SIAM Rev.*, vol. 34, no. 4, pp. 561–580, Dec. 1992, doi: 10.1137/1034115.

[22] W. Fang, “Reconstruction of permittivity profile from boundary capacitance data,” *Applied Mathematics and Computation*, vol. 177, no. 1, pp. 178–188, 2006, doi: https://doi.org/10.1016/j.amc.2005.10.046.

[23] R. Burkart, A. Dugenske, and T. Kurfess, “Enhanced Part Accuracy Through Strain Measurement in Milling Machines,” *Journal of Manufacturing Science and Engineering*, vol. 142, no. 1, p. 011002, 2020.

[24] G. Alvarez-Botero, F. E. Baron, C. C. Cano, O. Sosa, and M. Varon, “Optical sensing using fiber Bragg gratings: fundamentals and applications,” *IEEE Instrumentation & Measurement Magazine*, vol. 20, no. 2, pp. 33–38, 2017.

[25] J. Li *et al.*, “High spatial resolution distributed fiber strain sensor based on phase-OFDR,” *Optics express*, vol. 25, no. 22, pp. 27913–27922, 2017.

[26] B. Sollerv, D. Gifford, M. Wolfe, M. Froggatt, M. Yu, and P. Wysocki, “Measurement of localized heating in fiber optic components with millimeter spatial resolution,” 2006, p. OFN3.

[27] A. K. Sang, M. E. Froggatt, D. K. Gifford, S. T. Kreger, and B. D. Dickerson, “One Centimeter Spatial Resolution Temperature Measurements in a Nuclear Reactor Using Rayleigh Scatter in Optical Fiber,” *IEEE Sensors J.*, vol. 8, no. 7, pp. 1375–1380, Jul. 2008, doi: 10.1109/JSEN.2008.927247.

[28] S. Sandlin and A. Hokkanen, “Embedding optical fibers in metal alloys,” *IEEE instrumentation & measurement magazine*, vol. 6, no. 2, pp. 31–36, 2003.

[29] N. A. Hoult, O. Ekim, and R. Regier, “Damage/Deterioration Detection for Steel Structures Using Distributed Fiber Optic Strain Sensors,” *J. Eng. Mech.*, vol. 140, no. 12, p. 04014097, Dec. 2014, doi: 10.1061/(ASCE)EM.1943-7889.0000812.

[30] “Strain Sensing for Compact Heat Exchanger Defect Detection | Pressure Vessels and Piping Conference | ASME Digital Collection.” https://asmedigitalcollection-asme-org.ezproxy.proxy.library.oregonstate.edu/PVP/proceedings/PVP2019/58967/V005T10A006/1068604 (accessed May 28, 2020).

[31] T. Chen *et al.*, “Distributed hydrogen sensing using in-fiber Rayleigh scattering,” *Applied Physics Letters*, vol. 100, no. 19, p. 191105, 2012.

[32] F. Scurti, S. Ishmael, G. Flanagan, and J. Schwartz, “Quench detection for high temperature superconductor magnets: a novel technique based on Rayleigh-backscattering interrogated optical fibers,” *Supercond. Sci. Technol.*, vol. 29, no. 3, p. 03LT01, Mar. 2016, doi: 10.1088/0953-2048/29/3/03LT01.

[33] D. C. Betz, G. Thursby, B. Culshaw, and W. J. Staszewski, “Advanced layout of a fiber Bragg grating strain gauge rosette,” *Journal of Lightwave Technology*, vol. 24, no. 2, pp. 1019–1026, Feb. 2006, doi: 10.1109/JLT.2005.862442.

[34] Yung Bin Lin, Kuo Chun Chang, Jenn Chuan Chern, and L. A. Wang, “Packaging methods of fiber-Bragg grating sensors in civil structure applications,” *IEEE Sensors J.*, vol. 5, no. 3, pp. 419–424, Jun. 2005, doi: 10.1109/JSEN.2005.844539.

[35] Q. Zhang *et al.*, “Strain transfer in distributed fiber optic sensor with optical frequency domain reflectometry technology,” *Optical Engineering*, vol. 58, p. 15, 2019.

[36] S.-C. Her and C.-Y. Huang, “Effect of Coating on the Strain Transfer of Optical Fiber Sensors,” *Sensors*, vol. 11, no. 7, pp. 6926–6941, Jul. 2011, doi: 10.3390/s110706926.

[37] Z. Wang, H. Li, L. Zhang, and J. Xue, “Strain Transfer Characteristic of a Fiber Bragg Grating Sensor Bonded to the Surface of Carbon Fiber Reinforced Polymer Laminates,” *Applied Sciences*, vol. 8, no. 7, p. 1171, Jul. 2018, doi: 10.3390/app8071171.

[38] H.-N. Li, G.-D. Zhou, L. Ren, and D.-S. Li, “Strain Transfer Coefficient Analyses for Embedded Fiber Bragg Grating Sensors in Different Host Materials,” *J. Eng. Mech.*, vol. 135, no. 12, pp. 1343–1353, Dec. 2009, doi: 10.1061/(ASCE)0733-9399(2009)135:12(1343).

[39] H. Wang and P. Xiang, “Strain transfer analysis of optical fiber based sensors embedded in an asphalt pavement structure,” *Meas. Sci. Technol.*, vol. 27, no. 7, p. 075106, Jul. 2016, doi: 10.1088/0957-0233/27/7/075106.

[40] H. P. Wang, P. Xiang, and X. Li, “Theoretical Analysis on Strain Transfer Error of FBG Sensors Attached on Steel Structures Subjected to Fatigue Load,” *Strain*, vol. 52, no. 6, pp. 522–530, 2016, doi: https://doi.org/10.1111/str.12195.

[41] X. Feng, J. Zhou, C. Sun, X. Zhang, and F. Ansari, “Theoretical and Experimental Investigations into Crack Detection with BOTDR-Distributed Fiber Optic Sensors,” *J. Eng. Mech.*, vol. 139, no. 12, pp. 1797–1807, Dec. 2013, doi: 10.1061/(ASCE)EM.1943-7889.0000622.

[42] Yi Renhui, Zhou Zude, Liu Mingyao, Ji Dongliang, “Dymamic strain transfer laes of surface bonded FBGs,” *China Mechanical Engineering*, vol. 24, pp. 3362–3367, 2016.

[43] H. Wang and J.-G. Dai, “Strain transfer analysis of fiber Bragg grating sensor assembled composite structures subjected to thermal loading,” *Composites Part B: Engineering*, vol. 162, pp. 303–313, Apr. 2019, doi: 10.1016/j.compositesb.2018.11.013.

[44] C.-L. Tien, L.-C. Chen, H.-Y. Chiang, W.-F. Liu, and H.-F. Shih, “Temperature sensors based on D-shaped Fiber Bragg Grating coated with different thin films,” 2012, pp. 1–3.

[45] X. C. Li, F. Prinz, and J. Seim, “Thermal behavior of a metal embedded fiber Bragg grating sensor,” *Smart materials and structures*, vol. 10, no. 4, p. 575, 2001.

[46] X. Li and F. Prinz, “Metal Embedded Fiber Bragg Grating Sensors in Layered Manufacturing,” *Journal of Manufacturing Science and Engineering*, vol. 125, no. 3, pp. 577–585, Aug. 2003, doi: 10.1115/1.1581889.

[47] Q. Li, G. Flamant, X. Yuan, P. Neveu, and L. Luo, “Compact heat exchangers: A review and future applications for a new generation of high temperature solar receivers,” *Renewable and Sustainable Energy Reviews*, vol. 15, no. 9, pp. 4855–4875, Dec. 2011, doi: 10.1016/j.rser.2011.07.066.

[48] B. S. Haynes and A. Johnston, “High-effectiveness micro-exchanger performance,” 2002.

[49] A. Klepka, W. Staszewski, R. Jenal, M. Szwedo, J. Iwaniec, and T. Uhl, “Nonlinear acoustics for fatigue crack detection – experimental investigations of vibro-acoustic wave modulations,” *Structural Health Monitoring*, vol. 11, no. 2, pp. 197–211, Mar. 2012, doi: 10.1177/1475921711414236.

[50] W. Abd el Bar, I. I. Mahmoud, and H. A. Konber, “Development and characterization of a neutron tomography system for a Research Reactor,” *Journal of Taibah University for Science*, vol. 10, no. 2, pp. 195–204, Apr. 2016, doi: 10.1016/j.jtusci.2015.03.002.

[51] E. Verstrynge, K. De Wilder, A. Drougkas, E. Voet, K. Van Balen, and M. Wevers, “Crack monitoring in historical masonry with distributed strain and acoustic emission sensing techniques,” *Construction and Building Materials*, vol. 162, pp. 898–907, Feb. 2018, doi: 10.1016/j.conbuildmat.2018.01.103.

[52] X. Feng, X. Zhang, C. Sun, M. Motamedi, and F. Ansari, “Stationary Wavelet Transform Method for Distributed Detection of Damage by Fiber-Optic Sensors,” *J. Eng. Mech.*, vol. 140, no. 4, p. 04013004, Apr. 2014, doi: 10.1061/(ASCE)EM.1943-7889.0000679.

[53] Z. Xu, X. Feng, S. Zhong, and W. Wu, “Surface Crack Detection in Prestressed Concrete Cylinder Pipes Using BOTDA Strain Sensors,” *Mathematical Problems in Engineering*, vol. 2017, pp. 1–12, 2017, doi: 10.1155/2017/9259062.

[54] R. M. Liu, S. K. Babanajad, T. Taylor, and F. Ansari, “Experimental study on structural defect detection by monitoring distributed dynamic strain,” *Smart Mater. Struct.*, vol. 24, no. 11, p. 115038, Nov. 2015, doi: 10.1088/0964-1726/24/11/115038.

[55] S. K. Babanajad and F. Ansari, “Mechanistic Quantification of Microcracks from Dynamic Distributed Sensing of Strains,” *J. Eng. Mech.*, vol. 143, no. 8, p. 04017041, Aug. 2017, doi: 10.1061/(ASCE)EM.1943-7889.0001230.

[56] Y. Dong, X. Bao, and L. Chen, “2-km-range and 2-cm-spatial-resolution Brillouin optical fiber sensor using a transient differential pulse pair,” in *Proceedings of 2011 International Conference on Electronics and Optoelectronics*, 2011, vol. 4, pp. V4-11.

[57] C. G. Berrocal, I. Fernandez, and R. Rempling, “Crack monitoring in reinforced concrete beams by distributed optical fiber sensors,” *Structure and Infrastructure Engineering*, pp. 1–16, Feb. 2020, doi: 10.1080/15732479.2020.1731558.

[58] Y. Shan, H. Xu, Z. Zhou, Z. Yuan, X. Xu, and Z. Wu, “State sensing of composite structures with complex curved surface based on distributed optical fiber sensor,” *Journal of Intelligent Material Systems and Structures*, vol. 30, no. 13, pp. 1951–1968, Aug. 2019, doi: 10.1177/1045389X19849287.

[59] X. Bao, D.-P. Zhou, C. Baker, and L. Chen, “Recent Development in the Distributed Fiber Optic Acoustic and Ultrasonic Detection,” *J. Lightwave Technol.*, vol. 35, no. 16, pp. 3256–3267, Aug. 2017, doi: 10.1109/JLT.2016.2612060.

[60] K. S. C. Kuang, “Distributed damage detection of offshore steel structures using plastic optical fibre sensors,” *Sensors and Actuators A: Physical*, vol. 229, pp. 59–67, Jun. 2015, doi: 10.1016/j.sna.2015.03.028.

[61] M. Saidi and A. Gabor, “Adaptation of the strain measurement in textile reinforced cementitious matrix composites by distributed optical fibre and 2D digital image correlation,” *Strain*, vol. 56, no. 1, Feb. 2020, doi: 10.1111/str.12335.

[62] M. Bado, J. Casas, and A. Barrias, “Performance of Rayleigh-Based Distributed Optical Fiber Sensors Bonded to Reinforcing Bars in Bending,” *Sensors*, vol. 18, no. 9, p. 3125, Sep. 2018, doi: 10.3390/s18093125.

[63] S. K. Everton, M. Hirsch, P. Stravroulakis, R. K. Leach, and A. T. Clare, “Review of in-situ process monitoring and in-situ metrology for metal additive manufacturing,” *Materials & Design*, vol. 95, pp. 431–445, Apr. 2016, doi: 10.1016/j.matdes.2016.01.099.

[64] C. Y. Yap *et al.*, “Review of selective laser melting: Materials and applications,” *Applied Physics Reviews*, vol. 2, no. 4, p. 041101, Dec. 2015, doi: 10.1063/1.4935926.

[65] Y. Z. Zhang, C. Meacock, and R. Vilar, “Laser powder micro-deposition of compositional gradient Ti–Cr alloy,” *Materials & Design*, vol. 31, no. 8, pp. 3891–3895, Sep. 2010, doi: 10.1016/j.matdes.2010.02.052.

[66] I. Shishkovsky, F. Missemer, and I. Smurov, “Direct Metal Deposition of Functional Graded Structures in Ti- Al System,” *Physics Procedia*, vol. 39, pp. 382–391, 2012, doi: 10.1016/j.phpro.2012.10.052.

[67] M. Y. Mendoza *et al.*, “Microstructures and Grain Refinement of Additive-Manufactured Ti-xW Alloys,” *Metall and Mat Trans A*, vol. 48, no. 7, pp. 3594–3605, Jul. 2017, doi: 10.1007/s11661-017-4117-7.

[68] S. Karnati, Y. Zhang, F. F. Liou, and J. W. Newkirk, “On the Feasibility of Tailoring Copper–Nickel Functionally Graded Materials Fabricated through Laser Metal Deposition,” *Metals*, vol. 9, no. 3, p. 287, Mar. 2019, doi: 10.3390/met9030287.

[69] W. Li, L. Yan, X. Chen, J. Zhang, X. Zhang, and F. Liou, “Directed energy depositing a new Fe-Cr-Ni alloy with gradually changing composition with elemental powder mixes and particle size’ effect in fabrication process,” *Journal of Materials Processing Technology*, vol. 255, pp. 96–104, May 2018, doi: 10.1016/j.jmatprotec.2017.12.010.

[70] Y. Chen, X. Zhang, M. M. Parvez, and F. Liou, “A Review on Metallic Alloys Fabrication Using Elemental Powder Blends by Laser Powder Directed Energy Deposition Process,” *Materials*, vol. 13, no. 16, p. 3562, Aug. 2020, doi: 10.3390/ma13163562.

[71] S. Karnati, F. F. Liou, and J. W. Newkirk, “Characterization of copper–nickel alloys fabricated using laser metal deposition and blended powder feedstocks,” *Int J Adv Manuf Technol*, vol. 103, no. 1–4, pp. 239–250, Jul. 2019, doi: 10.1007/s00170-019-03553-0.

[72] W. Cui, S. Karnati, X. Zhang, E. Burns, and F. Liou, “Fabrication of AlCoCrFeNi High-Entropy Alloy Coating on an AISI 304 Substrate via a CoFe2Ni Intermediate Layer,” *Entropy*, vol. 21, no. 1, p. 2, Dec. 2018, doi: 10.3390/e21010002.

[73] C. Wei, Z. Sun, Y. Huang, and L. Li, “Embedding anti-counterfeiting features in metallic components via multiple material additive manufacturing,” *Additive Manufacturing*, vol. 24, pp. 1–12, 2018.

[74] A. Reichardt *et al.*, “Development and characterization of Ti-6Al-4V to 304L stainless steel gradient components fabricated with laser deposition additive manufacturing,” *Materials & Design*, vol. 104, pp. 404–413, 2016.

[75] Y. Ma *et al.*, “Simultaneous Compositional and Grain Size Measurements Using Laser Opto-Ultrasonic Dual Detection for Additive Manufacturing,” *Materials*, vol. 13, no. 10, p. 2404, May 2020, doi: 10.3390/ma13102404.

[76] Y. Huang, F. Li, Y. Zhang, Y. Cai, and X. Hua, “Spectral analysis of the dynamic behavior of a welding arc during pulsed gas metal arc welding of AA5083 aluminum alloy with ER5183 wire,” *IEEE Transactions on Plasma Science*, vol. 47, no. 11, pp. 5078–5088, 2019.

[77] L. Song, W. Huang, X. Han, and J. Mazumder, “Real-Time Composition Monitoring Using Support Vector Regression of Laser-Induced Plasma for Laser Additive Manufacturing,” *IEEE Trans. Ind. Electron.*, vol. 64, no. 1, pp. 633–642, Jan. 2017, doi: 10.1109/TIE.2016.2608318.

[78] S. Wang and C. Liu, “Real-Time Monitoring of Chemical Composition in Nickel-Based Laser Cladding Layer by Emission Spectroscopy Analysis,” *Materials*, vol. 12, no. 16, p. 2637, Aug. 2019, doi: 10.3390/ma12162637.

[79] H. Krauss, C. Eschey, and M. F. Zaeh, “Thermography for Monitoring the Selective Laser Melting Process,” p. 16.

[80] M. Khanzadeh, S. Chowdhury, L. Bian, and M. A. Tschopp, “A Methodology for Predicting Porosity From Thermal Imaging of Melt Pools in Additive Manufacturing Thin Wall Sections,” in *Volume 2: Additive Manufacturing; Materials*, Los Angeles, California, USA, Jun. 2017, p. V002T01A044. doi: 10.1115/MSEC2017-2909.

[81] T. Craeghs, S. Clijsters, Jean.-P. Kruth, F. Bechmann, and Marie.-C. Ebert, "Detection of Process Failures in Layerwise Laser Melting with Optical Process Monitoring," *Physics Procedia*, vol. 39, pp. 753–759, 2012, doi: 10.1016/j.phpro.2012.10.097.

[82] M. Khanzadeh, S. Chowdhury, M. Marufuzzaman, M. A. Tschopp, and L. Bian, "Porosity prediction: Supervised-learning of thermal history for direct laser deposition," *Journal of Manufacturing Systems*, vol. 47, pp. 69–82, Apr. 2018, doi: 10.1016/j.jmsy.2018.04.001.

[83] Y. Zhang, G. S. Hong, D. Ye, K. Zhu, and J. Y. H. Fuh, "Extraction and evaluation of melt pool, plume and spatter information for powder-bed fusion AM process monitoring," *Materials & Design*, vol. 156, pp. 458–469, Oct. 2018, doi: 10.1016/j.matdes.2018.07.002.

[84] L. Scime and J. Beuth, "Using machine learning to identify in-situ melt pool signatures indicative of flaw formation in a laser powder bed fusion additive manufacturing process," *Additive Manufacturing*, vol. 25, pp. 151–165, Jan. 2019, doi: 10.1016/j.addma.2018.11.010.

[85] O. Kwon *et al.*, "A deep neural network for classification of melt-pool images in metal additive manufacturing," *J Intell Manuf*, vol. 31, no. 2, pp. 375–386, Feb. 2020, doi: 10.1007/s10845-018-1451-6.

[86] B. Cheng and K. Chou, "Melt pool evolution study in selective laser melting." 26th Annual International Solid Freeform Fabrication Symposium-An Additive Manufacturing Conference, 2015.

[87] B. Cheng and K. Chou, "A numerical investigation of thermal property effects on melt pool characteristics in powder-bed electron beam additive manufacturing," *Proceedings of the Institution of Mechanical Engineers, Part B: Journal of Engineering Manufacture*, vol. 232, no. 9, pp. 1615–1627, Jul. 2018, doi: 10.1177/0954405416673105.

[88] E. Mirkoohi, D. E. Seivers, H. Garmestani, and S. Y. Liang, "Heat Source Modeling in Selective Laser Melting," *Materials*, vol. 12, no. 13, p. 2052, Jun. 2019, doi: 10.3390/ma12132052.

[89] J. A. Ramos-Grez and M. Sen, "Analytical, quasi-stationary Wilson-Rosenthal solution for moving heat sources," *International Journal of Thermal Sciences*, vol. 140, pp. 455–465, Jun. 2019, doi: 10.1016/j.ijthermalsci.2019.03.017.

[90] A. E. Hassanin, F. Scherillo, U. Prisco, R. Sansone, and A. Astarita, "Selective laser melting of Cu-inconel 718 powder mixtures," *Journal of Manufacturing Processes*, vol. 59, pp. 679–689, Nov. 2020, doi: 10.1016/j.jmapro.2020.10.039.

[91] "Thermal properties of metals, conductivity, thermal expansion, specific heat." [Online]. Available: https://www.engineersedge.com/properties_of_metals.htm

[92] "Copper-Nickel Alloys: Properties, Processing, Applications." [Online]. Available: https://www.copper.org/applications/marine/cuni/properties/DKI_booklet.html#pro

[93] A. Chowdhury, E. Kautz, B. Yener, and D. Lewis, "Image driven machine learning methods for microstructure recognition," *Computational Materials Science*, vol. 123, pp. 176–187, Oct. 2016, doi: 10.1016/j.commatsci.2016.05.034.

[94] C. Gobert, E. W. Reutzel, J. Petrich, A. R. Nassar, and S. Phoha, "Application of supervised machine learning for defect detection during metallic powder bed fusion additive manufacturing using high resolution imaging.," *Additive Manufacturing*, vol. 21, pp. 517–528, May 2018, doi: 10.1016/j.addma.2018.04.005.

[95] *Encyclopedia of Environmental Health*. Elsevier, 2019.

[96] D. S. Bulgarevich, S. Tsukamoto, T. Kasuya, M. Demura, and M. Watanabe, "Pattern recognition with machine learning on optical microscopy images of typical metallurgical

microstructures," *Sci Rep*, vol. 8, no. 1, p. 2078, Dec. 2018, doi: 10.1038/s41598-018-20438-6.

[97] G. Rogova, "Combining the Results of Several Neural Network Classifiers," in *Classic Works of the Dempster-Shafer Theory of Belief Functions*, R. R. Yager and L. Liu, Eds. Berlin, Heidelberg: Springer, 2008, pp. 683–692. doi: 10.1007/978-3-540-44792-4_27.

[98] G. Zhang, B. Eddy Patuwo, and M. Y. Hu, "Forecasting with artificial neural networks:: The state of the art," *International Journal of Forecasting*, vol. 14, no. 1, pp. 35–62, Mar. 1998, doi: 10.1016/S0169-2070(97)00044-7.

[99] M. W. Craven and J. W. Shavlik, "Using neural networks for data mining," *Future Generation Computer Systems*, vol. 13, no. 2, pp. 211–229, Nov. 1997, doi: 10.1016/S0167-739X(97)00022-8.

[100] "MULTI-SENSOR DATA FUSION FOR SPECIFIC ENERGY ESTIMATION IN A SURFACE GRINDING PROCESS." https://www-jstage-jst-go-jp.ezproxy.proxy.library.oregonstate.edu/article/isfa/2018/0/2018_325/_article/-char/ja/ (accessed Oct. 07, 2021).

[101] I. A. Basheer and M. Hajmeer, "Artificial neural networks: fundamentals, computing, design, and application," *Journal of microbiological methods*, vol. 43, no. 1, pp. 3–31, 2000.

[102] G. Mohr, S. Nowakowski, S. J. Altenburg, C. Maierhofer, and K. Hilgenberg, "Experimental Determination of the Emissivity of Powder Layers and Bulk Material in Laser Powder Bed Fusion Using Infrared Thermography and Thermocouples," *Metals*, vol. 10, no. 11, p. 1546, 2020.

[103] J. C. Heigel and B. M. Lane, "MEASUREMENT OF THE MELT POOL LENGTH DURING SINGLE SCAN TRACKS IN A COMMERCIAL LASER POWDER BED FUSION PROCESS," p. 8.

[104] M. Sezgin and B. Sankur, "Survey over image thresholding techniques and quantitative performance evaluation," *Journal of Electronic imaging*, vol. 13, no. 1, pp. 146–165, 2004.

[105] N. Chaki, S. H. Shaikh, and K. Saeed, "Applications of binarization," in *Exploring Image Binarization Techniques*, Springer, 2014, pp. 65–70.